EXPERIMENTAL VERIFICATION OF A THEORETICAL LOADING FUNCTION DESCRIBING MOMENTUM TRANSFER FROM AN EXPLOSION TO A TREE STEM

Malcolm P. Keown, et al

Army Engineer Waterways Experiment Station
Vicksburg, Mississippi

January 1976

EXPERIMENTAL VERIFICATION OF A THEORETICAL LOADING FUNCTION DESCRIBING MOMENTUM TRANSFER FROM AN EXPLOSION TO A TREE STEM

by

Malcolm P. Kinnis, Jack E. Stutz, Hongbing Nitschke

Protective and Environmental Systems Laboratory
U. S. Army Engineer Waterways Experiment Station
P. O. Box 631, Vicksburg, Miss. 39180

January 1979
Final Report

Unclassified

SECURITY CLASSIFICATION OF THIS PAGE (When Data Entered)

REPORT DOCUMENTATION PAGE

READ INSTRUCTIONS BEFORE COMPLETING FORM

1. REPORT NUMBER: Technical Report M-76-2
2. GOVT ACCESSION NO.:
3. RECIPIENT'S CATALOG NUMBER:

4. TITLE (and Subtitle): EXPERIMENTAL VERIFICATION OF A THEORETICAL LOADING FUNCTION DESCRIBING MOMENTUM TRANSFER FROM AN EXPLOSION TO A TREE STEM

5. TYPE OF REPORT & PERIOD COVERED: Final report

6. PERFORMING ORG. REPORT NUMBER:

7. AUTHOR(s): Malcolm P. Keown, Jack K. Stoll, Hansjoerg Nikodem

8. CONTRACT OR GRANT NUMBER(s):

9. PERFORMING ORGANIZATION NAME AND ADDRESS: U. S. Army Engineer Waterways Experiment Station, Mobility and Environmental Systems Laboratory, P. O. Box 631, Vicksburg, Mississippi 39180

10. PROGRAM ELEMENT, PROJECT, TASK AREA & WORK UNIT NUMBERS: Project 4A062112A859, Task 05

11. CONTROLLING OFFICE NAME AND ADDRESS: Office, Chief of Engineers, U. S. Army, Washington, D. C. 20314

12. REPORT DATE: January 1976

13. NUMBER OF PAGES: 106

14. MONITORING AGENCY NAME & ADDRESS (if different from Controlling Office):

15. SECURITY CLASS. (of this report): Unclassified

15a. DECLASSIFICATION/DOWNGRADING SCHEDULE:

16. DISTRIBUTION STATEMENT (of this Report)

Approved for public release; distribution unlimited.

17. DISTRIBUTION STATEMENT (of the abstract entered in Block 20, if different from Report)

18. SUPPLEMENTARY NOTES

19. KEY WORDS (Continue on reverse side if necessary and identify by block number)

Dynamic loads
Explosion effects
Forests
Helicopter landing zones
Momentum transfer
Shock waves
Tree stems

20. ABSTRACT (Continue on reverse side if necessary and identify by block number)

This study was conducted to validate methods previously developed by the Waterways Experiment Station to theoretically predict the clearing capability of a given explosive at a selected site in a forested area to be used as a helicopter landing zone. The prediction depends largely on a theoretical loading function used in the solution of a partial differential equation that describes the motion of a tree stem being acted upon by a shock front.

(Continued)

DD FORM 1 JAN 73 1473 EDITION OF 1 NOV 65 IS OBSOLETE

Unclassified

SECURITY CLASSIFICATION OF THIS PAGE (When Data Entered)

20. ABSTRACT (Continued)

Special equipment was designed to evaluate the loading function in terms of the impulse experienced by free-flying logs, which represented the tree stems. Seven explosions of 0.09-metric-ton TNT equivalent yield were detonated to provide adequate data for evaluation. Each explosion was monitored for the correct yield and shock-front symmetry. The results show good agreement between the stem loading predicted by the theoretical loading function and the actual loading experienced by the logs during the tests.

Appendix A describes the development of a failure criterion for a tree stem under dynamic loading by a shock front. Specification of the failure criterion requires the solution of the partial differential equation discussed above. The solution of the equation using the finite difference method is presented in detail.

Appendix B demonstrates a method to rapidly determine the remnant height of a tree stem for wide variations in explosive yield and tree properties. The solution is in the form of a nomograph.

THE CONTENTS OF THIS REPORT ARE NOT TO BE USED FOR ADVERTISING, PUBLICATION, OR PROMOTIONAL PURPOSES. CITATION OF TRADE NAMES DOES NOT CONSTITUTE AN OFFICIAL ENDORSEMENT OR APPROVAL OF THE USE OF SUCH COMMERCIAL PRODUCTS.

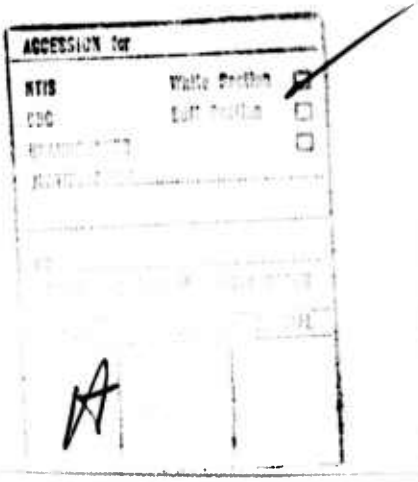

PREFACE

The study reported herein was performed in 1971 by the U. S. Army Engineer Waterways Experiment Station (WES) for the Office, Chief of Engineers, U. S. Army, under Military Engineering Design and Expedient Construction Criteria Project 4A062112A859, "Rapid Engineering Criteria," Task 05, "Development of High Explosive Techniques for Clearing Forested Areas." All phases of the study were under the general supervision of Messrs. W. G. Shockley, Chief, Mobility and Environmental Systems Laboratory (MESL), and W. E. Grabau, former Chief, Environmental Systems Division (ESD) and now Special Assistant, MESL, and under the direct supervision of Mr. J. K. Stoll, Chief, Environmental Simulation Branch (ESB), ESD.

Personnel who contributed to various phases of the project were: experimental design--Dr. H. Nikodem, formerly of MESL, Mr. M. P. Keown, ESB, Mr. P. A. Smith, Environmental Research Branch (ERB), ESD, and Mr. G. C. Downing, Chief, Dynamics Branch, Instrumentation Services Division (ISD); field experiments--Messrs. Smith and Downing, Mr. C. E. Stevens, Environmental Characterization Branch, ESD, Messrs. F. P. Leake, Jr., and B. C. Palmertree, ISD, Mr. S. E. Bartlett, Weapons Effects Laboratory, and Messrs. F. B. Gautier and J. W. Turner, Jr., Photography Branch, Publications and Graphic Arts Division, WES; and experimental data processing and analysis--Messrs. Keown and Downing, Mr. J. R. Lundien, ERB, CPT E. S. Neumann, CPT A. L. Hornbrook, and S5 R. G. Barden, all formerly assigned to MESL, and Messrs. J. L. Ferguson and C. B. Cox, ISD.

Mr. Bartlett was responsible for on-site safety precautions and detonation of the explosives. Messrs. Gautier and Turner were responsible for still and high-speed-motion photography. Mr. Downing was responsible for all electronic measurement and magnetic tape recording equipment used in the field experiments and supervised magnetic tape data processing.

The theoretical work related to momentum transfer from an explosion to a tree stem was done by Dr. Nikodem.

The report was prepared by Messrs. Keown and Stoll. Appendix A was prepared by Dr. Nikodem with the assistance of Mr. Keown and Mr. D. W. Walters, Automatic Data Processing Center, WES. Appendix B was prepared by Mr. Keown.

COL L. A. Brown, CE, BG E. D. Peixotto, CE, and COL G. H. Hilt, CE, were Directors of WES during the study and the preparation of the report. Mr. F. R. Brown was Technical Director.

CONTENTS

CONVERSION FACTORS, METRIC (SI) TO U. S. CUSTOMARY AND U. S. CUSTOMARY TO METRIC (SI) UNITS OF MEASUREMENT

Units of measurement used in this report can be converted as follows:

Multiply	By	To Obtain
Metric (SI) to U. S. Customary		
millimetres	0.0394	inches
centimetres	0.3937	inches
metres	3.2808	feet
kilometres	0.6213	miles (U. S. statute)
square centimetres	6.4516	square inches
cubic metres	35.3147	cubic feet
grams	0.002205	pounds (mass)
kilograms	2.2051	pounds (mass)
metric tons	2205.0	pounds
grams per cubic metre	62.43	pounds per cubic foot
dynes	2.248×10^{-6}	pounds (force)
centimetres per second	0.3937	inches per second
metres per second	3.2808	feet per second
U. S. Customary to Metric (SI)		
feet	0.3048	metres
grains	0.0648	grams
pounds (mass)	0.4535924	kilograms
pounds per square inch	6.894757	kilopascals
degrees (angle)	0.01745329	radians
Fahrenheit degrees	5/9	Celsius degrees or Kelvins*

* To obtain Celsius (C) temperature readings from Fahrenheit (F) readings, use the following formula: $C = (5/9)(F - 32)$. To obtain Kelvin (K) readings use: $K = (5/9)(F - 32) + 273.15$.

EXPERIMENTAL VERIFICATION OF A THEORETICAL LOADING FUNCTION DESCRIBING MOMENTUM TRANSFER FROM AN EXPLOSION TO A TREE STEM

PART I: INTRODUCTION

Background

1. An important characteristic of the U. S. Army's tactical mobility is the widespread and effective use of troop-carrying helicopters. Experience gained in Southeast Asia indicated that the Army must develop the capability to conduct effective military operations in forested areas that are intensively used by the enemy for sanctuaries and approach and retreat routes. Helicopter landing zones (HLZ's) are essential in such operations for tactical deployment of troops, resupply, evacuation of wounded, etc. An enemy's ingenious use of various antihelicopter mines and booby traps makes the use of existing clearings for HLZ's dangerous; furthermore, establishing an HLZ in hostile territory by conventional engineering techniques is both hazardous and time-consuming. Clearly, a new technique is needed for constructing HLZ's in forested areas that would meet the Army's mission requirements with a minimum exposure of men and equipment to a hostile environment.

2. In 1968 the U. S. Army Engineer Waterways Experiment Station (WES) began a study for the U. S. Air Force on the feasibility of using large bombs to rapidly construct clearings in forested areas. Full-scale experiments conducted at Fort Benning, Georgia, and in South Vietnam demonstrated the utility of the Air Force concept. The results of these experiments were used to structure a mathematical model to predict tree-remnant height as a function of distance from the center of the explosion, weapon yield, tree stem diameter, and tree strength. The results obtained from the model depend largely on a theoretical loading function used in the solution of a partial differential equation that describes the motion of an individual tree stem being acted upon by a shock front. Although the loading function was structured

using all available reliable data, the initial project plan did not include provisions to verify that the loading function reliably characterized the action of the shock front on the tree stem; however, results obtained from the model showed good agreement with test results. The output of the model can be used to compare predicted tree-remnant heights with vertical ground clearances required for helicopter landing and takeoff. This comparison will indicate whether a clearing is satisfactory for landing zone operations prior to detonation of the munition. The development of the model and applications are described in Reference 1 and Appendices A and B of this report.

Purpose

3. The purposes of the study reported herein were to:

   a. Develop reliable methods for evaluating impulse loading of tree stems being acted upon by a shock front.

   b. Acquire adequate data to validate the theoretical loading function used in the partial differential equation describing tree stem motion under the influence of a shock front;[1] or if the loading function could not be validated, use the data to generate a new loading function.

Scope

4. Test equipment was assembled to measure the impulse loading of a tree stem by a shock front. Slash-pine logs were used to represent tree stems. Seven explosives of 0.09-metric-ton* (200-lb) TNT equivalent yield were detonated. Blast data from each shot were compared with established overpressure and time-of-arrival (TOA) data[2-5] to verify that the desired yield had been obtained and that the shock front propagated away from ground zero (GZ) in a symmetrical manner. A method was developed for evaluating the theoretical loading function in terms of the impulse experienced by the logs. Experimental and theoretical velocities were compared.

---

* A table of factors converting metric (SI) units of measurement to U. S. customary units, and U. S. customary to metric (SI) is given on page 5.

PART II: EXPERIMENTAL DESIGN AND PROCEDURES

Test Site

5. The series of test shots* was conducted on a flat plain at the WES Big Black Test Facility, 16 km east-southeast of Vicksburg, Mississippi, on the west bank of the Big Black River. The first soil layer at the test site generally consists of a thin mantle of topsoil underlain by silty clay (CL according to the Unified Soil Classification System) with a dry density of 2.3×10^7 g/m^3. A seismic refraction survey conducted at the site indicated that the compression wave velocity in the first layer was 300 m/sec; the minimum depth of the first layer was 6 m.

6. The site layout for a representative test shot is shown in Figure 1. The center of the explosive charge, hereafter referred to as GZ, was 75 m from the nearest vertical discontinuity that would cause any reflections of the shock front. At this distance the overpressure had decayed to less than 1 psi.**

Explosive

7. Ammonium nitrate (mixed with 6 percent by weight No. 2 diesel fuel) was chosen for the explosive material instead of TNT. An ammonium nitrate-fuel oil compound (hereafter referred to as AN/FO) is oxygen-balanced and, hence, the chemical reaction goes on to completion at the time of detonation. A TNT explosion is not an oxygen-balanced reaction and, therefore, may require several milliseconds (msec) to attain complete detonation of the explosive material. Therefore, use of AN/FO improved the probability of attaining a very rapid rate of energy release.

---

* The seven test shots of 0.09-metric-ton TNT equivalent yield will be referred to as BB001-BB007 throughout the remainder of this report when it is necessary to specify information about a particular shot.

** psi is retained as the unit of pressure as opposed to its metric equivalent because this unit remains in common use.

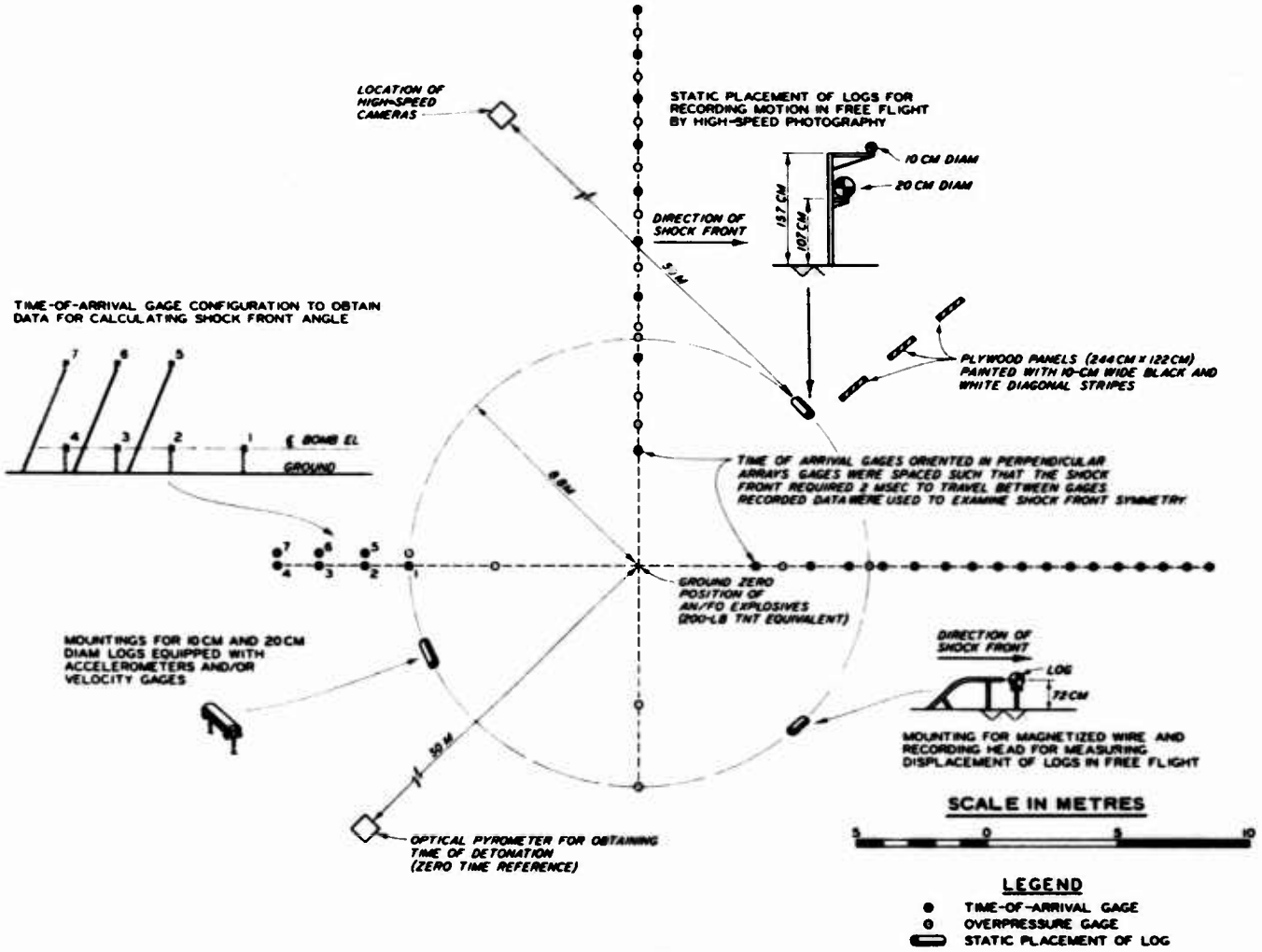

Figure 1. Representative layout for experimental equipment

Also, the safety precautions applicable to AN/FO explosives are considerably less restrictive than those applicable to TNT. The AN/FO explosive was prepared by mixing No. 2 diesel fuel oil with the ammonium nitrate (Gulf N-IV fertilizer) at a ratio of 6 parts fuel oil by weight to 94 parts ammonium nitrate. The ammonium nitrate was sensitized (oiled) at the site by vigorously pouring the mix back and forth between large metal cans. After the mixing procedure, the explosive was stored for at least 24 hr to allow maximum oil absorption by the ammonium nitrate.* The average equivalent weight of TNT to AN/FO in the 40-psi region is 0.85.[2] To produce a 0.09-metric-ton equivalent TNT yield, 104.5 kg of AN/FO were required.

8. For test shots BB001-BB003 (see Table 1) the AN/FO was placed in a cubical Styrofoam container (Figure 2a) having a spherical cavity 0.64 m in diameter. The height of burst (measured from the ground to the center of the cavity) was 0.72 m. This value was scaled down from the height of burst of the Fort Benning shot,[1] by the cube-root scaling laws applicable to explosives,[6] so that the results from the Fort Benning test and those from tests conducted at the Big Black Test Facility could be compared. The explosive was detonated by a 4-lb C-4 booster with a No. 10 Engineer's Special Blasting Cap and 200-grain Primacord. The cubical exterior shape of the Styrofoam container was modified to a spherical shape (Figure 2b) after shot BB003 (Table 1) to preclude the possibility that the additional volume of the cubical container might contribute to the heat of the explosion or could in some way distort the symmetry of the shock front. No evidence was noted on subsequent tests of any differences in the explosions as a result of changing containers.

---

* Gulf N-IV ammonium nitrate fertilizer is in the form of spheres (average diameter 1.5 mm) that are generally called "prills." The spherical surface configuration allows maximum chemical absorption for a given volume.

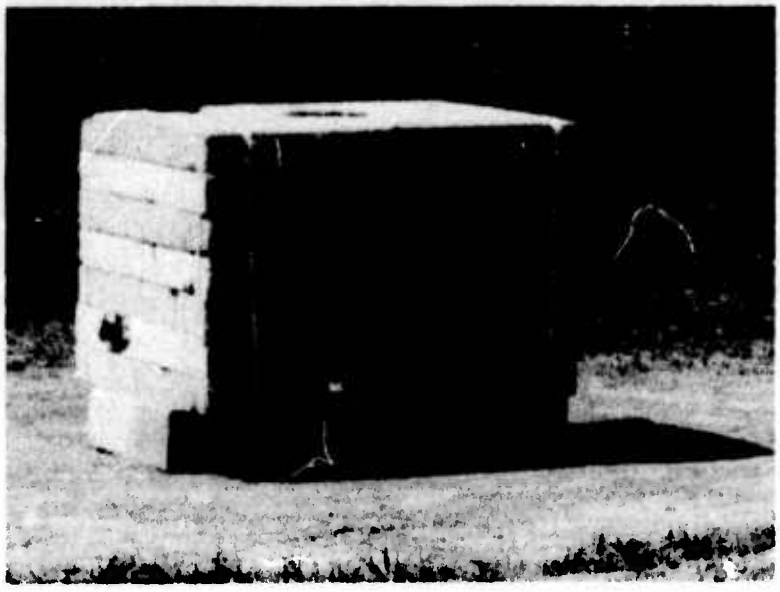

a. Shots BB001-BB003

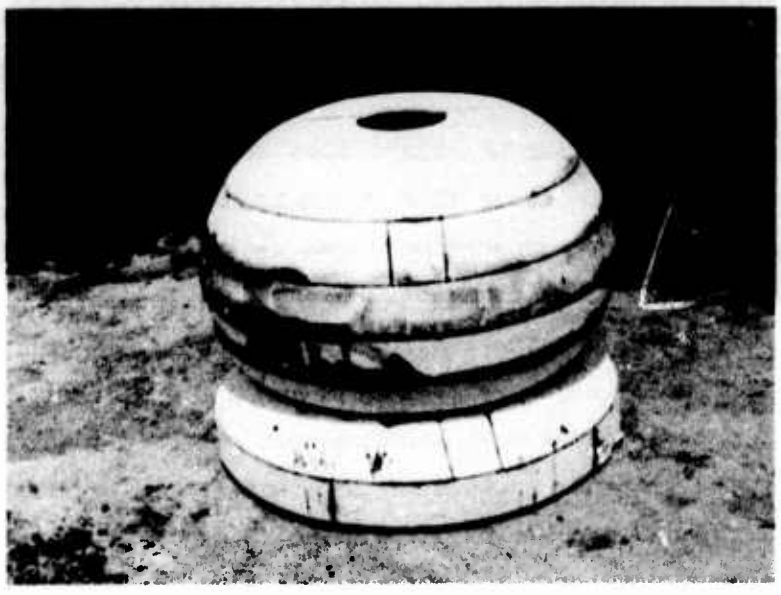

b. Shots BB004-BB007

Figure 2. Containers used to hold AN/FO

Logs

9. As stated in paragraph 4, logs were used to represent tree stems. It was believed that logs would simulate stem behavior under shock loading, since the previous study[1] had shown that the failure of a tree stem is not influenced by the crown or root mass of the tree, i.e., the portion of the stem that is subjected to deformation is a free body from the initial interaction of the stem and the shock front until stem failure. Logs used for the test program were termed "free flying" to indicate that their motion was in no way constrained, i.e. a free body. The shock front that accelerated the logs into free flight was assumed to have spherical symmetry; therefore, the impulse loading on a free body (log) was the same in any plane tangent to the shock front. All the logs were statically placed (prior to detonation) in a horizontal position such that the longitudinal axis of the log was tangent to the shock front (assuming that the shock front would expand as a sphere centered at GZ). The logs were placed horizontally in lieu of other orientations because they could be positioned easily on simple stands with only minor difficulties in maintaining calibration on logs that were instrumented.

10. Logs used during the first five shots (see Table 2) were initially positioned no closer than 8.8 m to GZ and were greater than 6 cm in diameter. These constraints were necessary so that the logs would not sustain physical damage (such that the log would not be reusable, see Figure 3) and the instrumentation would not malfunction because of abnormally high overpressures and jetting (see paragraphs 64-66). The data from the Fort Benning test shot[1] (3.6-metric-ton yield) indicated that all trees 6 cm in diameter or larger that were 30 m or more from GZ did not fail. According to the cube-root scaling laws applicable to explosives,[6] a 6-cm-diam stem would not fail at 8.8 m from GZ for a 0.09-metric-ton yield. Therefore, by placing the logs at a distance of 8.8 m or more from GZ (an overpressure of approximately 40 psi) and by using logs greater than 6 cm in diameter, it was felt that no serious damage to the logs nor the instrumentation mounted

on some of them would result. The logs were moved closer to GZ for tests BB006 and BB007 to determine the limit of reliability of the instrumentation.

Figure 3. Maximum expansion of fireball (test shot BB002) did not reach logs placed 8.8 m from GZ

Noninstrumented logs

11. Two noninstrumented logs were used in shots BB001 and BB002 to obtain a displacement-time history of a flying log by high-speed photography (see paragraph 55). The logs were placed prior to detonation of the explosive on a stand constructed of 7.6-cm channel iron anchored in concrete as shown in the extreme right of Figure 3 (also see Figure 1). The logs were 111.8 cm long and had 20- and 10-cm diameters and weighed 33,966 and 6,351 g, respectively. The ends were painted in alternating black and white quadrants.

Instrumented logs and stands

12. Fifteen logs were instrumented; most were used for more than one test shot. These logs were assigned numbers for test purposes as indicated in Table 2; however, log number 1 in one test was not necessarily the same log number 1 in another test. These logs were 111.8 cm long, either 10 or 20 cm in diameter, and varied in mass (including

instrumentation) from 9,054 to 38,206 g. Fourteen of the logs were rough (natural surface); the other log had been turned down in a lathe so that its surface was smooth and was used to study the relative effect of surface condition on the drag coefficient of the log. The logs were instrumented on both ends and the center to obtain a displacement-time history of a flying log by using accelerometers (paragraph 24), velocity gages (paragraph 25), and specially constructed displacement-time equipment (paragraph 26). Because the displacement-time equipment used with the logs is unique, a brief description of the several types used during the test program is provided in paragraph 26.

13. Two types of stands were used during the test program to support the instrumented logs prior to detonation of the explosive. The first type was constructed of 7.6-cm channel iron anchored in buried concrete bases of relatively large mass (Figure 4a). The backfill around each base was compacted to a high density. This construction technique was used to minimize the effect of any vibrations caused by ground motion occurring at the test stands before the arrival of the shock front and to prevent any damage to the stands by airblast. Examination of the log stands and test data after the first test shot indicated that the rigid construction techniques described above were not necessary. Therefore, a less costly mounting stand was prefabricated from 1.25-m lengths of 5.1-cm angle iron (vertical members) and 15-cm sections of 7.6-cm channel iron (horizontal members) as shown in Figure 4b. One vertical and one horizontal member were required to support each end. This stand could be installed by one man whereas the concrete-based stands required several men and a dragline to lift the concrete base into place. All logs were positioned on the stands such that their initial trajectories would not be affected by electrical cables or by the supports on which they rested. The logs were put in place by resting the ends on foam pads. Each log instrumented with accelerometers and/or velocity gages was staked to prevent any movement. The stability was necessary so that the accelerometers and velocity gages would remain calibrated during the time interval between

a. Stand constructed of 7.6-cm angle iron anchored in concrete

b. Stand constructed of a 1.25-m length of 5.1-cm angle iron (vertical member) and a 15-cm section of 7.6-cm channel iron (horizontal member)

Figure 4. Log stands used in test program

positioning and detonation. The stakes were removed just prior to countdown and detonation.

14. An attempt was made in shot BB003 (paragraph 36) to evaluate the effect of the supporting stand on the test results of an instrumented log; this was accomplished by hanging log number 3 (see Table 2) by its ends with piano wire. The piano wire was hung across two electrodes (mounted in the horizontal beam as shown in Figure 5a) that were part of a circuit connected directly to the firing mechanism. When the charge was detonated, a high current passed through the piano wire, instantaneously melting the wire and releasing the log into free fall. The entire support array was constructed of 10- by 10-cm timber (Figure 5b).

Recorders

15. The field data (other than the high-speed photographic records) from all the shots (Table 1) were recorded on magnetic tape. Overpressure, acceleration, velocity, displacement-time, TOA, a zero-time indication, and a time reference code, i.e. an Inter-Range Instrumentation Group (IRIG) trace, were recorded during each detonation. The data were recorded with Model 3560 Sangamo Portable Magnetic Tape Recorder/Reproducers manufactured by Sangamo Electric Company. Two such recorders were used for each detonation; each carried 14 data channels. The IRIG trace was obtained with a Model SP-100-BS IRIG-B Test Time Code Generator manufactured by Flow Corporation and fed into the recorder. The generator produced 100 pps, 30 bit binary coded decimal time of year/17 bit time of day. The recorders and associated equipment were housed in a van located 200 m from GZ.

Instrumentation

16. Instrumentation was selected for each detonation that would provide information on the blast characteristics and the response to the blast of free-flying logs (see paragraph 9 for definition of free-flying logs). The characteristics of the blast were determined from

a. Piano wire hanging across electrodes that were connected to detonation circuit

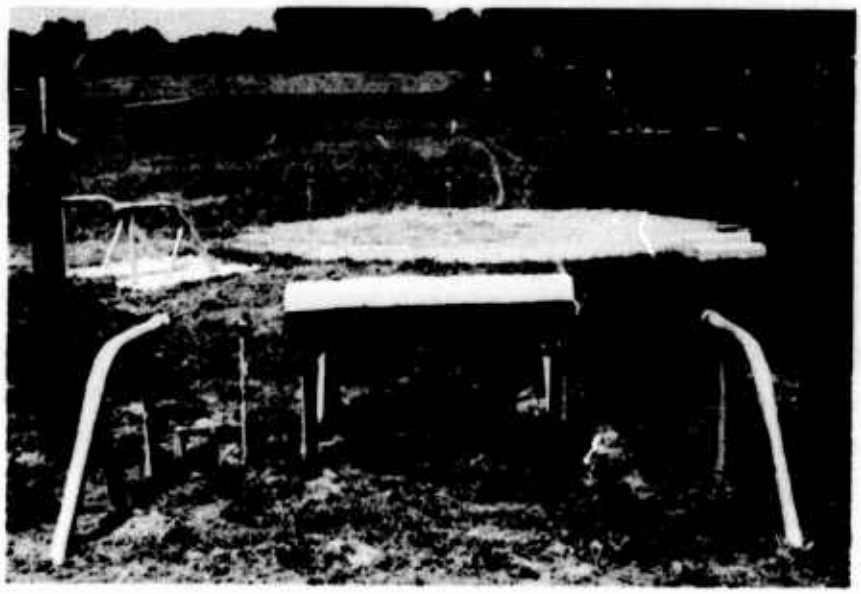

b. Log suspended by piano wire hung across two electrodes mounted in overhead beam

Figure 5. Apparatus used as alternative to log stands

measurements of incident overpressure versus time, time of arrival of the shock front at various distances from GZ, and from high-speed-photography records. The flying log's response to the shock front was evaluated from measurements of acceleration, velocity, and displacement-time, and from high-speed-photography records.

Overpressure (OP) gages

17. Norwood Models 211-34-C and 11A-34 bonded strain-gage pressure transducers manufactured by American Standard, Inc., were used to detect the TOA of the shock front and to measure the OP at selected locations (see Figure 1 and Table 3). These transducers were mounted flush with the ground (Figure 6a). Pressure imposed upon the flush-mounted diaphragm and strain-tube assembly causes minute compression of the strain tube, resulting in a signal output from the gage that is directly proportional to the pressure. Also used were Model LC-35 pressure transducers manufactured by Atlantic Research Corporation. These gages were used in conjunction with a Kistler preamplifier to achieve the necessary signal conditioning and were mounted on stands such that the points were oriented radially toward GZ (Figure 6b).

TOA gages

18. The TOA gages, constructed at WES, were used in shots BB001, BB002, and BB005 to determine the arrival time of the shock front at a given distance from GZ (Figure 1 and Table 4). Each gage consisted of a small paper vane attached to an arm that pivoted back against a brittle pencil lead (Figure 7a). As the shock front passed, the lead was broken by the arm and a voltage change was recorded on magnetic tape. The TOA gages were assembled in arrays to allow study of the symmetry of the shock front and to obtain continuous records of OP versus distance from GZ. Figure 7b shows the array used in shot BB002 (see paragraph 35) to obtain data from which OP could be calculated from TOA data (see paragraph 80) and from which the shape of the shock front could be examined (paragraph 72).

19. The TOA gages were mounted such that the pressure-sensitive element (the paper vane) was between GZ and the aluminum pole on which the gage was mounted. Hence, the pencil lead would be broken by the

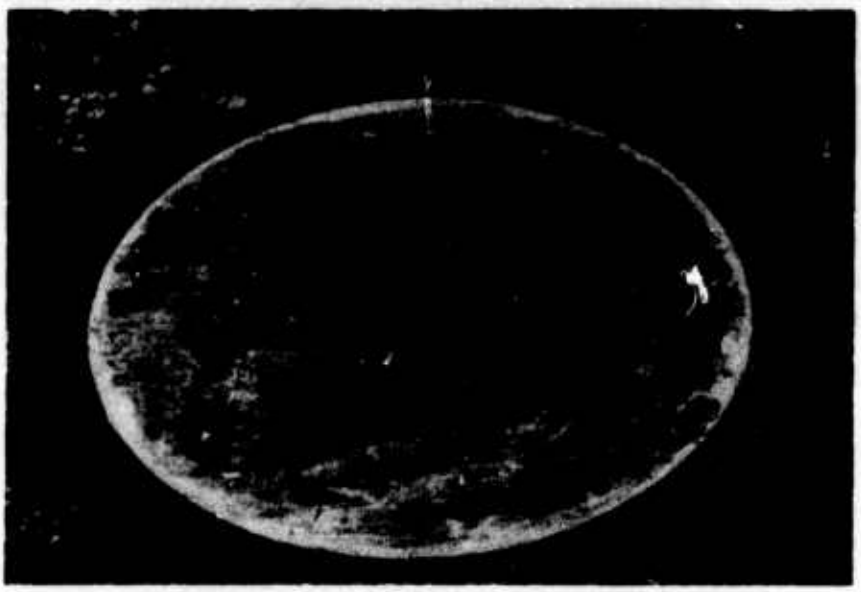

a. Norwood Model 211-34-C gage mounted flush with ground surface

b. Atlantic Research Corporation Model LC-35 gage oriented radially toward GZ

Figure 6. OP gages

a. Single TOA gage

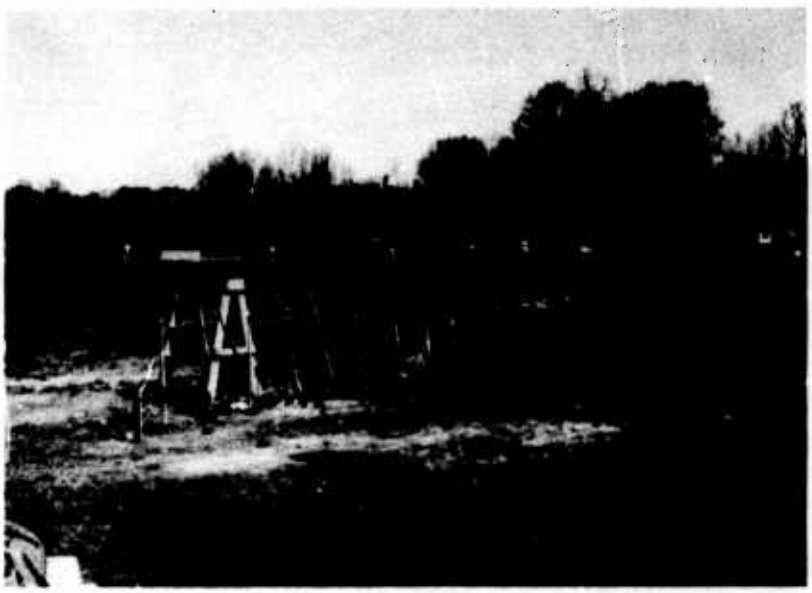

b. Array of TOA gages used for shot BB002

Figure 7. TOA gages

paper vane before the shock front set the aluminum pole into oscillatory motion (and, as a result, possibly break the pencil lead). The TOA gages were attached to the aluminum poles with hose clamps; a Styrofoam strip was placed between the hose clamp and the pole to mechanically decouple the gage and the aluminum pole. This was necessary because wind or personnel occasionally set an aluminum pole into oscillation and the pencil lead was broken. The Styrofoam strip prevented breakage of the pencil lead in the majority of cases where unwanted oscillations occurred.

20. Two electrical circuits were developed to accommodate the TOA gages. One circuit (Figure 8a) was used for a single gage on a single data channel and the other (Figure 8b) for multiple gages on a single channel. The circuit shown in Figure 8a functions as follows: Prior to the breaking of the pencil lead by the paper vane, the amplifier draws no current from the 24-v source. When the pencil lead breaks, the input voltage to the amplifier rises to 5.1 v (the operating voltage of the Zener diode) and the amplifier draws current. The increase in current produces a discontinuity on a magnetic tape data record. This discontinuity can be visually examined on an oscillogram reproduced from the magnetic tape. The arrival time can be estimated from the discontinuity. In addition to its capacity as a voltage regulator, the Zener diode serves as a clipper for transients induced in the cable by the explosion. This circuit was used when several TOA values were required at the same distance from GZ, i.e., separate channels were required because the discontinuities occurred simultaneously.

21. The circuit shown in Figure 8b functions as follows: Prior to the breaking of the pencil lead closest to GZ, the input load impedance on the amplifier is the equivalent resistance of the number of 10-k resistors in parallel (one 10-k resistor for each TOA gage). The input voltage is zero. When the shock front breaks the first pencil lead, the Zener diode becomes active and supplies 5.1 v to the 10-k resistor in series with the amplifier input, and the amplifier draws current, which in turn produces a discontinuity on a magnetic tape data record that corresponds to the arrival time of the shock front. When the second pencil lead breaks, the amplifier draws twice as much current,

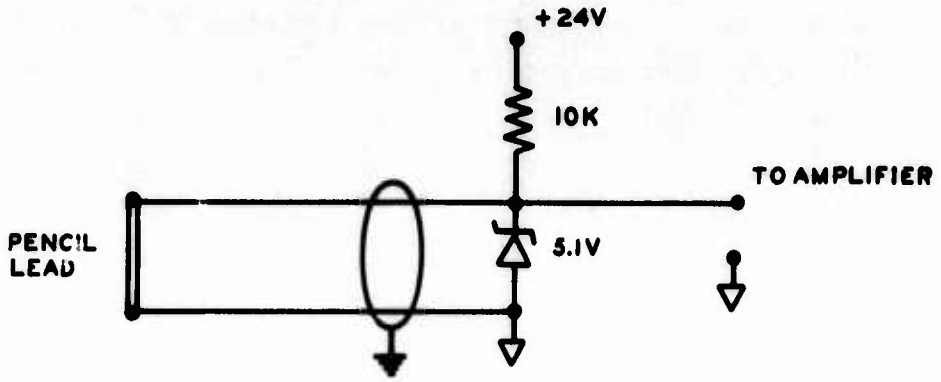

a. Circuit for one TOA gage on single data channel

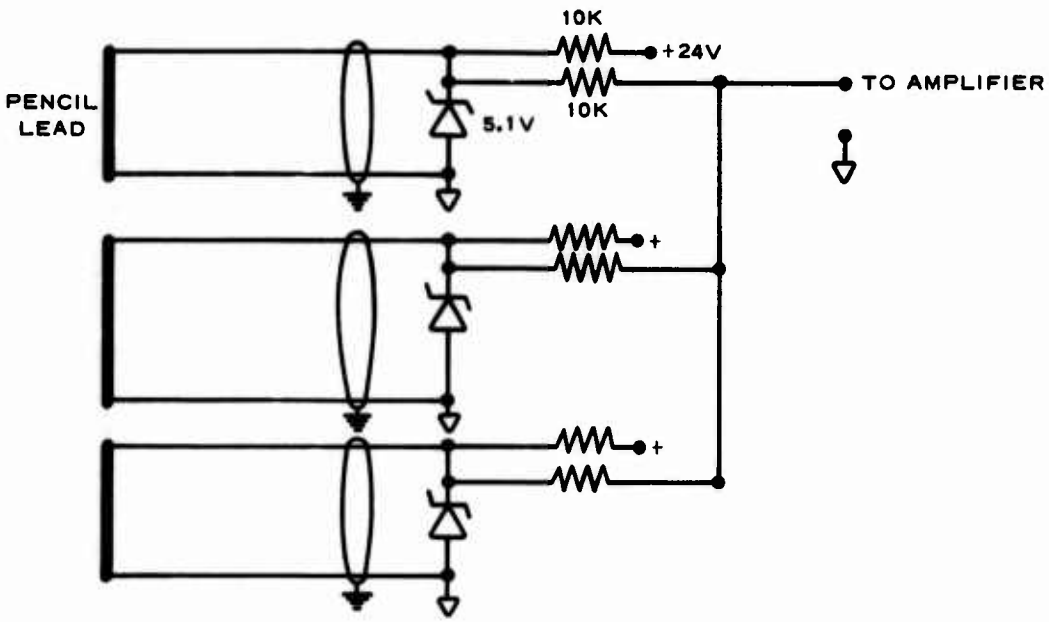

b. Circuit for multiple TOA gages on single data channel. Only three TOA gages are shown, but the circuit can be expanded to accommodate more gages (see text)

Figure 8. Circuits for TOA gages

and another discontinuity occurs, i.e., the currents from the individual TOA circuits are additive. The increase of current due to the breaking of the pencil leads continues until the shock front reaches the end of the array of TOA gages. The number of gages on a circuit is limited only by the readability of the record, i.e., as the number of gages on the line increases, the step height of the discontinuities decreases for the same maximum amplifier input current. The maximum number of gages successfully used on a single data channel during the test program was 15. This type of circuit was used when TOA data were required on the same azimuth as, but at different distances from, GZ.

Instrumentation for
determination of zero time

22. The estimation of shock front arrival time from oscillogram trace discontinuities requires an accurate reference value (zero time). Zero time was generated by two techniques. The primary zero time indication was obtained from a break-wire circuit. The wire was wrapped around the booster in the center of the explosive sphere of AN/FO (paragraph 8). When the explosive was detonated, the wire broke and produced a change of voltage in the circuit. The change of voltage appeared as a sharp discontinuity on the resulting oscillogram trace. The secondary zero time was obtained from a Questar telescope (see Table 1) with a photodiode attached to the eyepiece (Figure 9). The illumination from the explosion generated sufficient output from the photodiode to place a discontinuity on the oscillogram trace.

Earth-movement canister

23. Horizontal and vertical soil displacements were measured by a Model 354137-0102 velocity gage manufactured by Bell and Howell. The gage was used only for test shots BB001 and BB002 (see Table 1). Data from these tests indicated that the air shock was arriving before the ground shock and, therefore, ground shock could not affect the instrumentation (see paragraph 61); hence, use of these gages was discontinued after test shot BB002.

Accelerometers

24. Models 2261 (4000-g max) and 2265M1 (2500-g max)

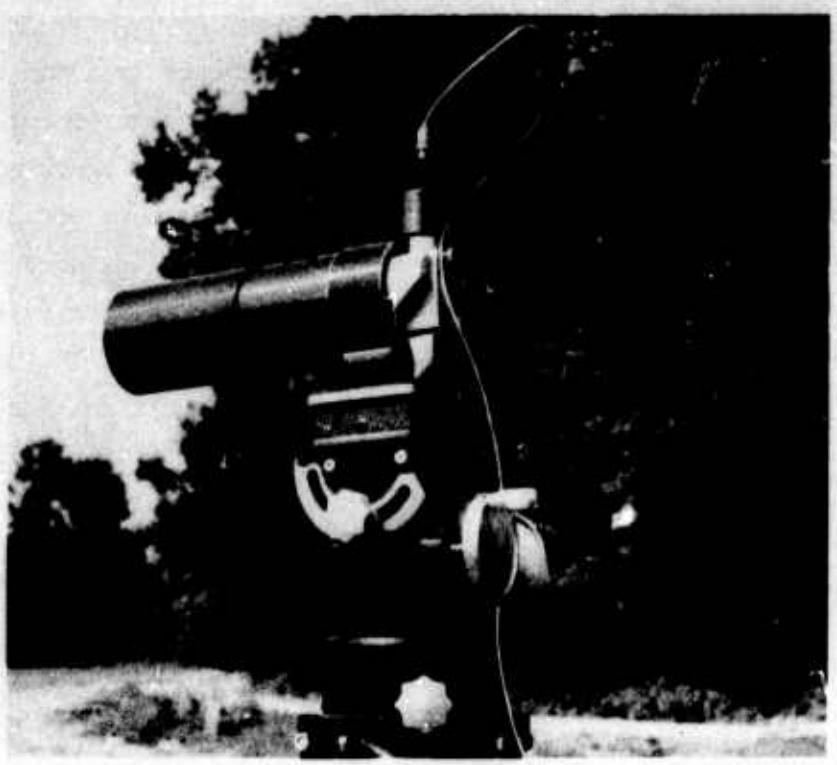

Figure 9. Questar telescope with photodiode attached to eyepiece used to obtain secondary zero time

accelerometers manufactured by Endevco Corporation were used (see Table 2) to measure the horizontal and vertical components of the acceleration experienced by the flying logs. The choice of accelerometer range is usually made on the basis of the maximum acceleration expected. However, the range choice also dictates the resonant frequency of the accelerometer (a high-range accelerometer has higher resonant frequency than a low-range accelerometer of the same type). The Model 2261 accelerometer had a resonant frequency of 30 kHz and the Model 2264M1, 20 kHz. To avoid getting erroneous acceleration data, the gages must be operated well below their resonant frequencies, as was the case for this test program. The accelerometers were mounted within hollowed-out portions of the flying logs, and expanded foam was used to secure each gage in place (Figure 10). The accelerometers produced signals with amplitudes proportional to acceleration along the designated axis (horizontal or vertical) of the log. They were used in conjunction with a WES Type 100-OP amplifier to achieve the necessary signal conditioning

Figure 10. Acceleration and velocity gages mounted in expanded foam in hollowed-out portion of log. Cables associated with the gages are shown coming from the log

and were calibrated prior to each test shot.

Velocity gages

25. Two types of velocity gages were used: a Model 7LV6-N velocity gage manufactured by Sanborn Company, and a Model DX5 velocity gage manufactured by Sparton Southwest, Inc. The Sanborn gage (a linear inductive type) produced a signal with an amplitude proportional to linear velocity and had an effective measuring length (displacement) of 15 cm. This gage was used on log numbers 2 and 3 in test shots BB003 and BB004 (see Table 2). The Sparton gage (variable reluctance type) produced a signal with an amplitude proportional to horizontal or vertical velocity. This gage was used on log numbers 1 and 3 in test shots BB003 and BB004. Each gage was precalibrated (or checked for calibration) prior to each test shot. The necessary temperature correction factors (paragraph 29b(6)) were incorporated in the calibration procedure. The velocity gages were mounted in the logs in the same manner as the acceleration gages (Figure 10).

Displacement-time gages

26. Four types of gages were constructed and tested at WES to

examine the displacement-time characteristics of flying logs. Because these gages are unique, their development is discussed below. The initial configuration consisted of a rigid steel wire connected to the end of the log. The other end of the wire was hook-shaped; perpendicular to the hook were fine wires spaced a known distance apart (Figure 11a). When the log was acted upon by the shock front, it was displaced. As the log was displaced, the hook broke the fine wires in succession. Figure 11b is a schematic of the circuit. Each broken wire increased the input resistance (and voltage) of the data channel amplifier. This produced a step on the resulting oscillogram trace corresponding to a known distance. Hence, in conjunction with the IRIG trace (see paragraph 15), a displacement-time record was obtained. Unfortunately, the apparatus generated data of poor quality. Even though the fine-wire configuration was mounted under protective cover in a rigidly mounted stand (see paragraph 13), some of the fine wires were broken by the initial impact of the shock front before the steel hook came into contact with them. Figure 4a shows the log in position on the stand; the fine-wire configuration is inside the hollow upper horizontal member of the stand. This device was used for test shots BB001 and BB002 (see Table 2). The fine-wire concept was rejected in favor of using photoelectric cells in place of the fine wires. The circuitry required for the photoelectric scheme became extremely complicated and was subsequently rejected. The third configuration consisted of a wire magnetized at known increments, attached to the end of the log. As the log moved away from the stand, the wire moved past a recording head mounted in the stand. Thus, a displacement-time record was produced for the flying log. This configuration was successful, as discussed in the following paragraph.

27. The magnetic recording head and magnetized wire were mounted in the upper horizontal member of the stand (Figure 4a) in much the same manner as the wire-breaker and photoelectric configurations. Figure 12 is a detailed diagram of the magnetic head and magnetized wire. One end of the magnetized wire is attached to the object to be displaced and the other end is threaded through the wire guide on the magnetic head (the head remains stationary). When the wire is moved

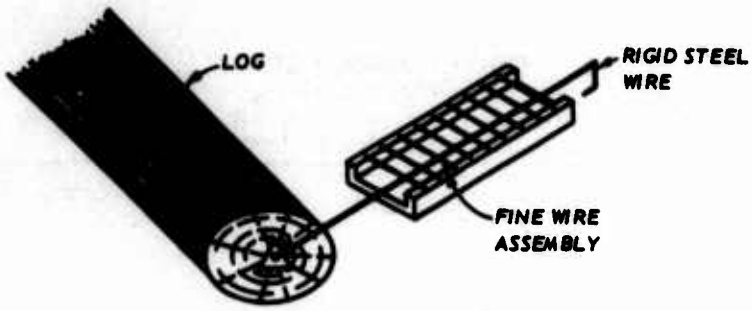

a. Schematic of apparatus

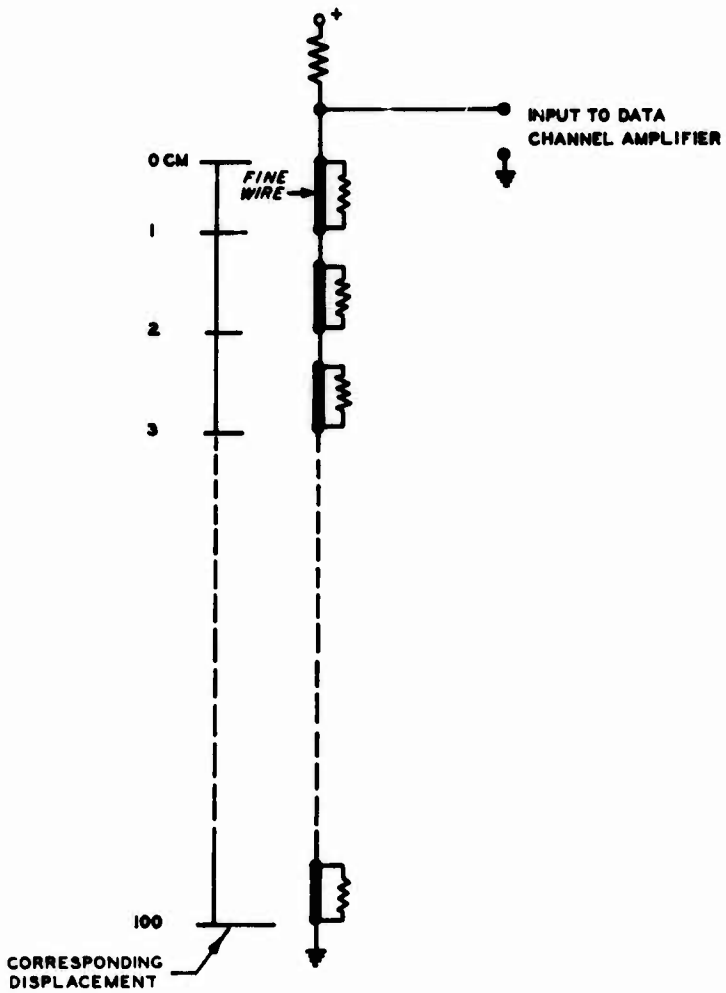

b. Schematic of circuit

Figure 11. Wire-breaker apparatus used to obtain displacement-time record of flying log

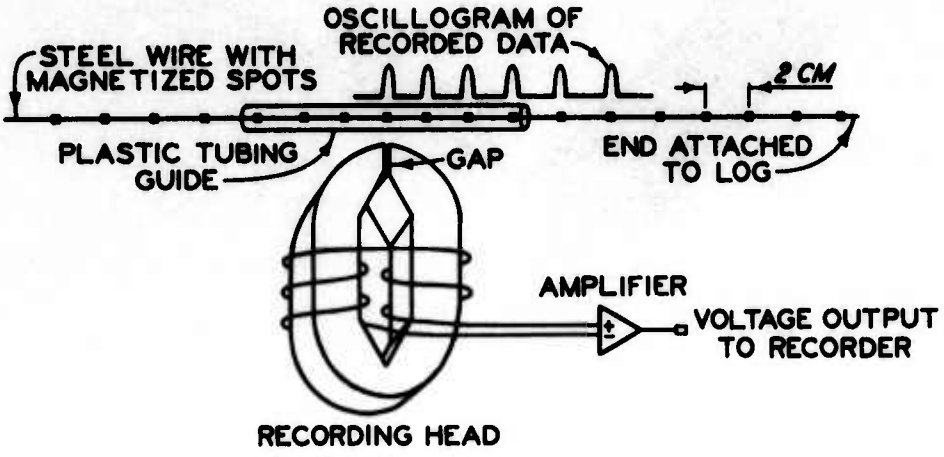

Figure 12. Magnetic apparatus for obtaining displacement measurements of log motion

(i.e., log displacement), the magnetized spots travel across the air gap on the magnetic head causing a varying flux, ϕ , through the core. An electric potential is produced in the coil of wire proportional to the rate of change in flux, i.e., $V = d\phi/dt$, and this voltage is fed into an amplifier to raise the signal to recording level. A displacement-time trace can then be reproduced on an oscillogram for data analysis. This device was used for test shots BB003 and BB004 (see Table 2).

28. The fourth displacement-time apparatus is shown in Figure 13. The log was positioned on the test stand constructed from 1.25-m lengths of angle iron (vertical members) and 15-cm sections of channel iron (horizontal members) (see paragraph 13 and Figure 4b). The magnetized-wire displacement-time apparatus (paragraph 27) was mounted inside a 6.3-cm-diam galvanized pipe structure immediately behind the test stand. A protective cap was threaded over the open end of the pipe to protect the magnetic head from the airblast. The magnetized wire was threaded through a Teflon guide in a hole drilled in the protective cap (Figure 14). This configuration produced good quality displacement-time data and was easier to install than any of the other methods previously tried, and was used for test shots BB003 through BB007.

Error analysis

29. Errors are inherent in any measurement system. The errors

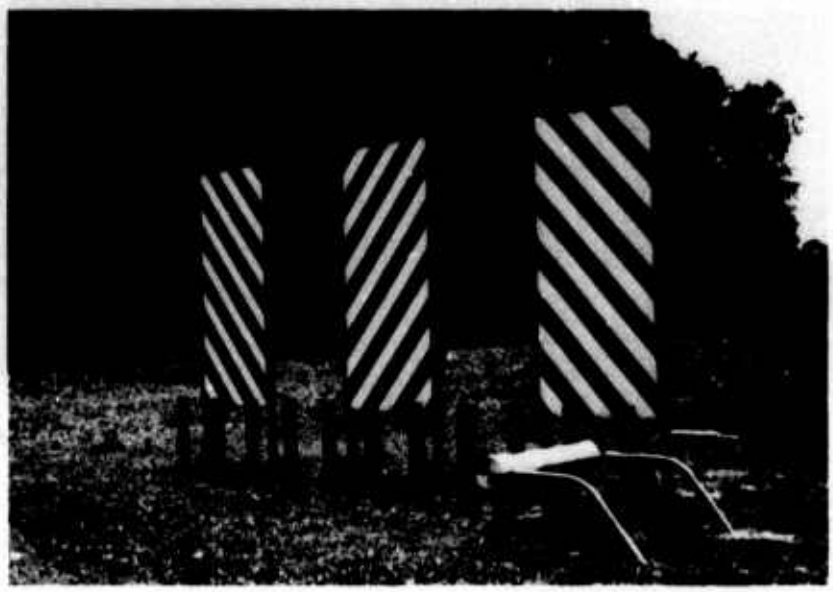

Figure 13. Modified stand used with displacement-time apparatus in test shots BB003-BB007. Vertical boards in background are for studying the shape of the shock front using high-speed photography

introduced by the gages used in the test series, together with estimates of error, are as follows:

a. Acceleration gages

(1) Calibration error (steady-state response). The acceleration gages were calibrated on a rotating table prior to their use in the field. Each had its own calibration factor; unless the gage is operated beyond its maximum range, this factor remains approximately the same throughout its life. Anticipated error is ±3 percent.

(2) Frequency response error. The acceleration gages have a damping factor of 0.03 (undamped) and therefore have a high peak in the response curve at the resonant frequency. To avoid erroneous data, the gage must be operated well below the resonant frequency. Large errors can also occur if the coupling device or medium produces secondary peaks in the response curve. Anticipated error is ±10 percent.

(3) Stability error. An acceleration gage may show a change in the calibration factor from day to day. This is a long-term drift factor that depends primarily on temperature. Anticipated error is ±1 percent.

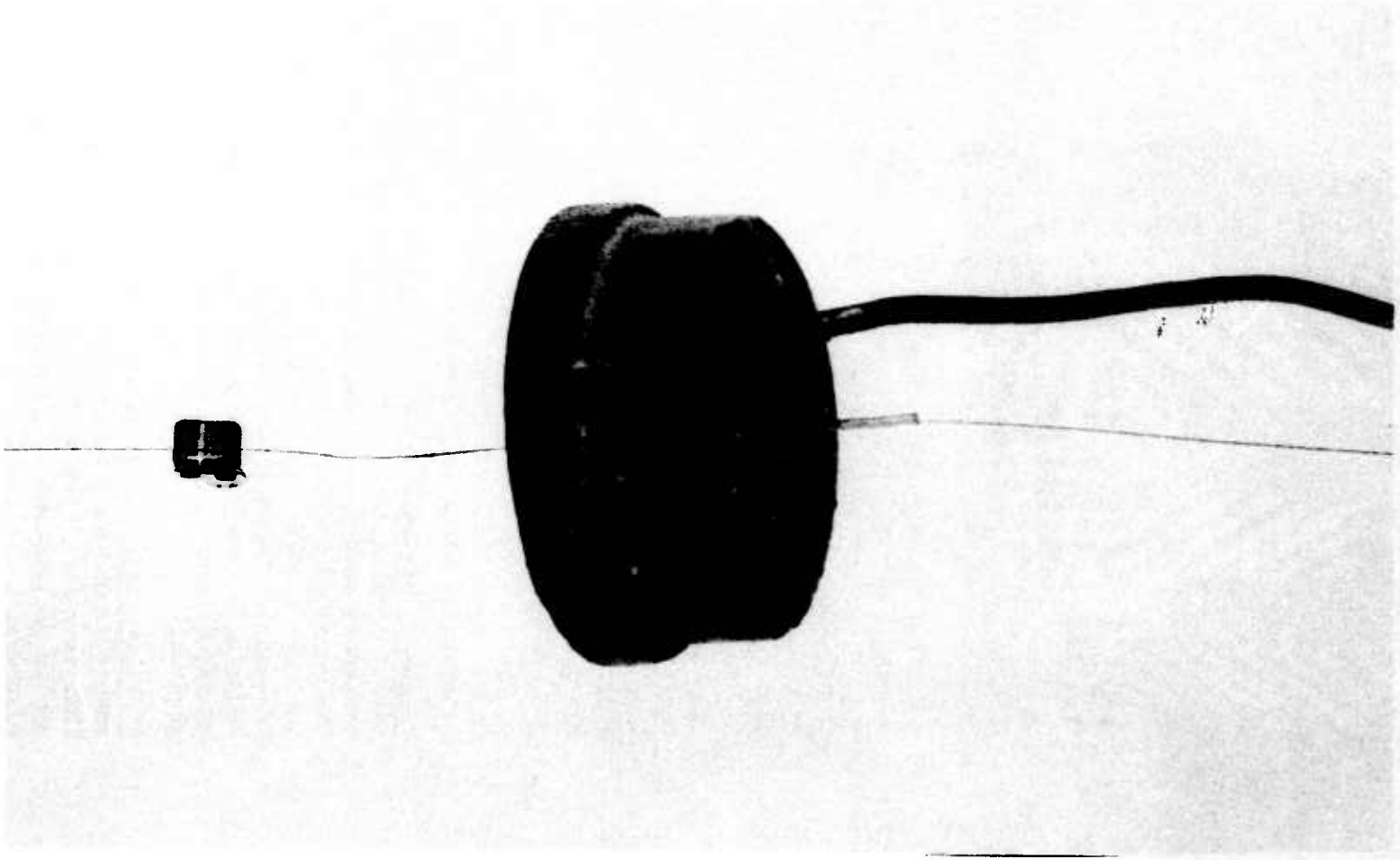

Figure 14. Magnetized-wire displacement-time apparatus. The magnetized wire is shown passing the recording head (left) and then through the Teflon wire guide in the protective cap. The two electrical wires connected to the recording head exit the protective cap via the cable shown on the upper portion of the cap. The recording head was mounted inside the cap during the tests

(4) Field reference error. The full-scale range of an acceleration gage is obtained from amplifier calibration by a resistor substitution technique. This resistance can be matched only approximately. Anticipated error is ±1 percent.

(5) Linearity error. The calibration curves are assumed to be linear, though in practice they have some second-order variations. Using a high-range acceleration gage for a low-range recording exaggerates this error. Anticipated error is ±3 percent.

(6) Mounting error. The acceleration gages were "soft" mounted in the logs, as opposed to "hard" mounting in which the gages are attached directly to the log. The soft mount requires that the transducer be embedded in a lossy material (foam plastic or polystyrene) in a hole in the log. This allows only the low-frequency components of the log's acceleration to couple to the acceleration gage. In effect, the soft mount is a low-pass filter. Thus, the acceleration curve or the integrals of the curve do not display the log motion, but represent the motion of the accelerometer. Errors in the acceleration magnitude may be due also to the gage not being exactly in the vertical or horizontal plane. Amplitude reduction is proportional to the cosine of the angle (5- to 10-deg max). Anticipated error is ±1 percent.

(7) Recording and digitization error. Minimal error is introduced by the analog tape recorder and the analog to digital converter (see paragraph 50). Anticipated total error is ±0.25 percent.

(8) Integration error. If errors in the measuring equipment cause the recordings of acceleration to show an offset after the main or peak acceleration has been passed, the integral of these data (especially for long periods after the peak acceleration) will contain errors in proportion to the product of the offset and the integration time. The offset voltage can be due to hysteresis in the amplifier or in the acceleration gage. The anticipated error due to hysteresis in the amplifier is ±0.1 percent, and in the acceleration gage is ±1 percent.

b. Velocity gages. Comments on the acceleration gages in subparagraphs (1), (4), (5), and (7) above apply to the velocity gages for error comments (1), (2), (3), and (4), respectively, below.

(1) Calibration error. Anticipated error is ±2 percent.

(2) Field reference error. Anticipated error is ±1 percent.

(3) Linearity error. Anticipated error is ±3 percent.

(4) Recording error. Anticipated error is ±0.25 percent.

(5) Frequency response error. The velocity gages are highly damped (mechanically damped with a viscous fluid) and have a frequency response of from 3 to 300 Hz. Since they are so highly damped, they do not normally have a peak in their response curve unless it is produced in the external mounting. Anticipated error is ±15 percent.

(6) Stability error. Velocity gages are sensitive to temperature and must be corrected for changes from the calibration temperature (1 percent/°F). With temperature correction, the maximum anticipated error is ±2 percent.

(7) Mounting error. Velocity gages are very sensitive to tilt (a 6-deg change is a full-scale effect). These gages were zeroed prior to the detonation by carefully changing the log position for zero response. If any log rotation takes place (changes of 1 deg or more), the effect on the output is significant. Rotation is evident on the recording as a steadily increasing or decreasing amplitude after the initial acceleration. Anticipated error is ±1 percent.

c. Displacement-time gages. Comments on the acceleration gages in subparagraphs a(1) and a(7) above apply to the displacement-time gages for error comments (1) and (2), respectively, below.

(1) Calibration error. Anticipated error is ±2 percent.

(2) Recording error. Anticipated error is ±0.25 percent.

(3) Mounting error. The displacement-time gages were mounted in a fixed stand with one end of the recording wire fixed to the log. A pull in any direction (i.e. combined vertical and horizontal displacement) activates the gage. Also, an air pressure differential between the inside of mount and the surrounding area may force the recording wire past the recording head without the corresponding log movement. Anticipated error is ±1 percent.

Meteorological instrumentation

30. Temperature and barometric pressure were measured prior to each test shot. These data are summarized in Table 5. The temperature was measured with a Friez hygrothermograph, Model 594; barometric pressure measurements were obtained from the weather station at WES. Wind

velocity was zero for each test. Shots were conducted on days when lighting was optimum for high-speed photography. This requirement precluded problems associated with detonation of explosives under low cloud ceilings.

High-Speed Camera

31. Five high-speed 16-mm movie cameras were used during the test series (see Table 1): a Milliken Model DBM SC manufactured by the D. B. Milliken Company (framing rate: 400 frames/second); a Reflex manufactured by Kodak (64 f/s); a Nova Model 16-3 manufactured by Photo-Kinetics, Inc. (framing rate variable to 40,000 f/s); a Model HS401 manufactured by Fairchild Camera and Instrument Company (2000 f/s); and a Fastex Model WF4T manufactured by Red Lake Laboratories, Inc. (5000 f/s). These cameras were used to obtain the displacement-time history of flying logs and to determine the shape of the shock front. Each camera was equipped with dual timing lenses and gave full-frame rather than split-frame type of coverage. The exposure rates used over the series of shots ranged from 64 to 8000 f/s. All cameras were mounted on tripods and were protected from flying debris with sandbags. Each tripod was rigidly fixed by a vertical tension cable between the tripod head and a ground anchor. Cameras were located approximately 50 m from GZ. Electrical timing circuits automatically activated the cameras prior to detonation allowing sufficient time for the film to accelerate to the required framing rate.

Test Program

Test shots

32. The objectives and site layout are described for each test shot in the following paragraphs.

33. Test Shot BB001. The objectives of shot BB001 were to:

a. Obtain the displacement-time history for flying logs.

b. Examine the geometrical properties of the shock front.

c. Make OP measurements to verify that the desired yield was obtained.

d. Measure soil displacement induced by the shock front.

34. The displacement-time histories of the flying logs were obtained with the wire-breaker apparatus described in paragraph 26 and from high-speed photography (Table 1). Two logs initially positioned at 8.8 m from GZ were used for this test (Table 4). The geometry of the shock front was examined in the horizontal plane by placing four TOA gages at 8.8 m from GZ, but spaced 90 deg apart. Equal arrival times at the same distances from GZ would indicate that the shock front was propagating away from GZ at the same velocity in four directions. The geometry of the shock front was examined in the vertical plane using high-speed photography and also by placing three TOA gages at 10.8, 12.3, and 13.8 m from GZ at the same elevation as that of the center of the explosion; three other gages were placed 2.37 m above these three. The inclination of the shock front with the horizontal could be examined from the activation sequence of the TOA gages (see paragraph 71). Four OP gages were placed at 8.8 m from GZ at azimuths* of 23, 90, 180, and 270 deg to verify that the desired yield had been obtained (Table 3). An earth-movement canister was placed at 8.8 m from GZ to measure horizontal and vertical soil displacement. Zero time was obtained from a break-wire device and a Questar telescope as described in paragraph 22. These two devices were used during the entire test series. Meteorological data were taken as described in paragraph 30. These data were taken for each test shot. The explosive was placed in a cubical Styrofoam container at GZ. A wide variety of cameras was used during the test series (see Table 1), and the selection of a particular high-speed camera for a particular shot depended more on its availability than on its capabilities. Some deterioration in the quality of the high-speed photography due to smoke from the explosion and ground dust was noted in this shot (see Figure 15).

---

* Azimuth was relative to point in center of large concrete block that was base of wire-breaker displacement-time stand used in test shots BB001 and BB002. The origin of the coordinate system was at GZ.

Figure 15. Ground dust beginning to obscure motion of log (shot BB001)

35. Test shot BB002. The objectives of shot BB002 were the same as those of BB001. The wire-breaker apparatus was again used to determine the displacement-time history of two flying logs initially positioned at 8.8 m from GZ. In addition to the four TOA gages positioned at 8.8 m from GZ (spaced 90 deg apart) that were used to study shock-front geometry in the horizontal plane, four additional TOA gages were placed at 22.48 m from GZ and spaced 90 deg apart. Two linear strings of eighteen TOA gages were placed radially from GZ starting at 1.65 m and extending out to 21.64 m. The strings were positioned 90 deg apart (see Table 4). The arrival times measured at these gages could be used to compute OP as a function of distance from GZ (see paragraph 80). The arrival times could also be used with the four gages at 8.8 m and at 22.48 m to study shock front geometry in the horizontal plane because each string had a gage at the same distance from GZ. An additional string of TOA gages was placed 1 m above one of the strings described above beginning at 8.0 m from GZ and extending out to 16.4 m. This configuration was used to examine the inclination of the shock front with the horizontal. Two OP gages were placed at 5.49 m from GZ

(azimuths of 93 and 183 deg, respectively) and two were placed at 8.8 m (azimuths of 23 and 273 deg, respectively) (Table 3). An attempt was made to reduce ground dust by placing a membrane over the ground at distances close to GZ that were in the field of view of the high-speed cameras (Figure 16). The membrane proved ineffective and was not used in any of the following tests.

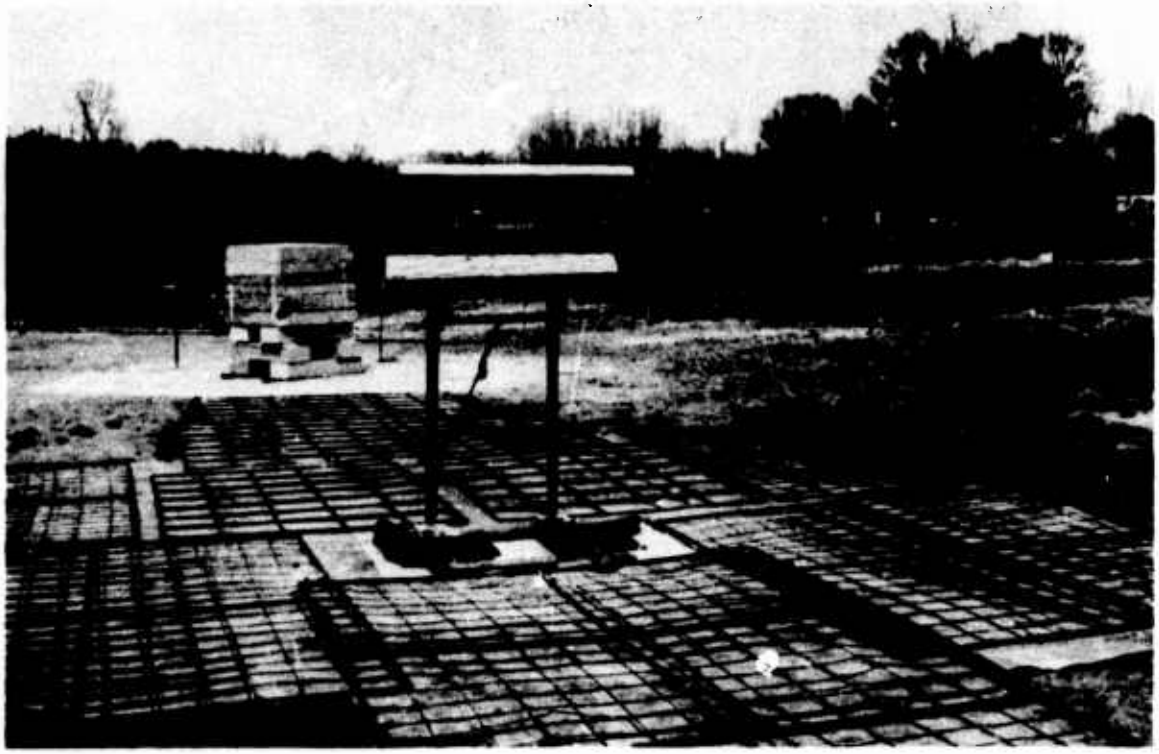

Figure 16. Membrane used for shot BB002 to reduce ground dust

36. Test shot BB003. The displacement-time instrumentation used for shots BB001 and BB002 proved to be unreliable; therefore, the major objective of shot BB003 was to obtain reliable displacement-time data for the flying logs. Three logs were used in shot BB003. These logs were positioned at 8.8 m from GZ. Accelerometers and velocity gages were mounted on each log. The displacement-time instrumentation used in the first two shots was replaced by the magnetized-wire devices described in paragraphs 26 and 27. One of the magnetized-wire devices was mounted in the stand used for the wire breaker; the other was mounted in a less rigid stand constructed of 6.3-cm-diam galvanized

pipe (see paragraph 28). No TOA gages were used for this test shot. Three OP gages were placed at 5.49 m from GZ at azimuths of 93, 183, and 273 deg (Table 3). The technique of hanging a log by piano wire (log number 3; see paragraph 14) resulted in no detectable improvement in the quality of the data and so was deleted from the program. The cost and effort involved in the installation could not be justified.

37. Test shot BB004. The objective of this shot was to collect additional displacement-time data for the flying logs. Four logs were positioned at 8.8 m for this shot. One log was attached to the magnetized-wire device mounted in the stand used for the wire breaker in shots BB001 and BB002. The other three were attached to the magnetized-wire apparatus mounted in the 6.3-cm-diam galvanized pipe stand. Accelerometers and velocity gages were mounted on three logs. The fourth log had only an accelerometer. This log had a smooth surface and was used to examine the effect of the log's surface on the displacement-time history. All other logs used during the test series had their natural surface (see paragraph 12). No TOA gages were used for this test. Three OP gages were placed at 5.49 m from GZ at azimuths of 138, 183, and 273 deg (Table 3). Reasonable success had been experienced after shots BB002 and BB003 in locating the position of the shock front at various times after detonation by viewing adjacent frames of the high-speed photography (see paragraph 56). To improve the contrast of the background, three plywood backboards (1.2 by 2.4 m) were erected in the field of view of the high-speed cameras (see Figure 13). These boards were positioned perpendicularly to the camera and were painted with black and white diagonal stripes; they were used for the remainder of the test series. The cubical Styrofoam container (Figure 2a) used to hold the AN/FO prior to detonation for test shots BB001 through BB003 was replaced by a spherical container (Figure 2b and Table 1) to preclude the possibility that the additional volume of the cubical container might contribute to the heat of the explosion. The spherical container was used for the remainder of the test series.

38. Test shot BB005. The magnetic-wire displacement-time apparatus mounted in the 6.3-cm-diam galvanized pipe stand generated excellent

data in shot BB004, and was used for the remainder of the test shots. Now that reliable instrumentation had been assembled, a test shot (BB005) was conducted to hopefully meet all the design objectives of test shot BB001. Two logs were initially positioned at 8.8 and 12.2 m, respectively, from GZ (Table 2). All logs in prior tests had been positioned at 8.8 m; the log placed at 12.2 m was used to verify that the magnetic-wire displacement-time device would function correctly when the incident OP on the log was less than 40 psi (this was the predicted OP at 8.8 m for the 104.5-kg AN/FO charge). The predicted OP at 12.2 m was 20 psi. Five TOA gages were placed at 8.8 m from GZ at azimuths of 68, 203, 247, 292, and 342 deg, respectively (Table 4). A linear string of 19 gages was oriented at 150 deg beginning at 4.46 m from GZ and extending out to 22.48 m. An experiment was conducted during this test to assess the effects of ground motion on the TOA gages. Three TOA gages were placed in cylindrical cavities at 6.51, 9.22, and 13.65 m from GZ. The covers of these cavities were sealed flush with the ground. Six OP gages were used for this shot (Table 3), placed at distances of 5.49, 5.49, 8.8, 8.8, 8.8, and 12.2 m from GZ at azimuths of 108, 293, 207, 344, 331, and 303 deg, respectively.

39. Test shot BB006. One log was used for this test. It was positioned at 4.4 m from GZ to verify that the magnetic-wire displacement device would function correctly at an OP of 200 psi, and that the galvanized pipe stand would not fail. No TOA gages were used for this test. OP gages were placed at distances of 5.49, 5.49, and 8.8 m from GZ at azimuths of 108, 207, and 292 deg, respectively (Table 3).

40. Test shot BB007. This test was identical with shot BB006 except that the log was positioned at 2.2 m from GZ (a predicted OP of 700 psi). The galvanized-pipe support apparatus after detonation of the charge is shown in Figure 17.

General procedures

41. Prior to each shot, all items that might have affected the trajectory of the flying logs or might have caused malfunction of the OP or TOA gages were removed from the test area. This included burying all cables, raking up all loose grass, paper, etc., and removing all

Figure 17. Galvanized-pipe support apparatus

stakes that held the instrumented logs in place.

42. Immediately after the detonation, the entire test area was surveyed. This included surveying the final positions of the flying logs and all fixed instrumentation apparatus. Survey of the apparatus was necessary because much of the data required that the support apparatus and gages be fixed with respect to a common frame of reference; otherwise, the data could not be related.

43. Although not directly related to the objectives of the test program, the following information may be of interest. Test shot BB001 produced a crater 60 cm deep and 285 cm wide as shown in Figure 18a. The dimensions of the crater indicated that some of the explosive yield was diverted from the shock front to cratering. This problem was eliminated by filling the crater after each subsequent explosion with a material that was denser and more cohesive than the original soil. This material was a soil-cement consisting of 10 percent cement by weight. The crater was backfilled by compacting the soil-cement in successive lifts of 15 to 20 cm. Use of this technique reduced the crater to 9 cm deep and 200 cm wide for shot BB002 (Figure 18b).

a. Test shot BB001

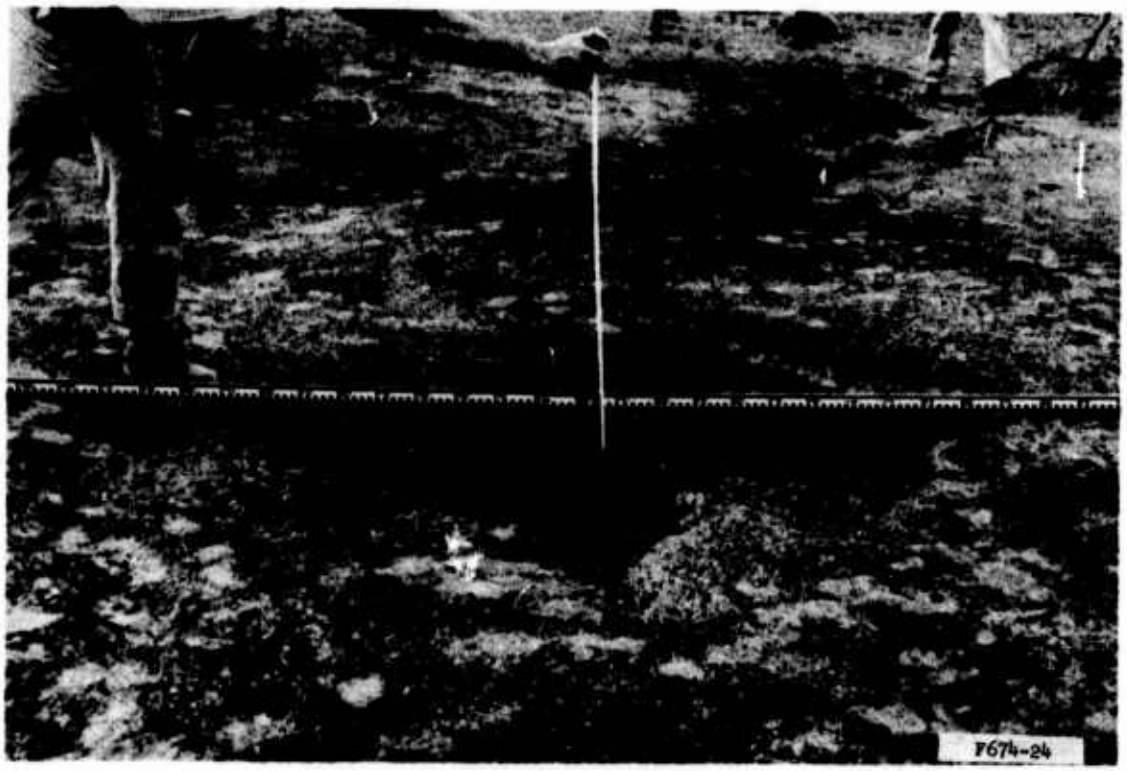

b. Test shot BB002

Figure 18. Craters produced by test shots BB001 and BB002

PART III: PROCESSING OF EXPERIMENTAL DATA

44. All experimental data (except high-speed photography) were recorded on magnetic tape and reproduced on oscillograms for analysis. These data included shock-front TOA and peak OP, and the dynamic properties of the flying logs. Prior to analysis, all data were processed using the methods described in the following paragraphs. A block diagram showing the data processing procedure is shown in Figure 19.

Discontinuous Data Records

Time of arrival

45. TOA data were obtained directly from the oscillograms produced from magnetic tape. Arrival time of the shock front at a particular TOA gage produced a step discontinuity on the oscillogram trace. This discontinuity resulted from a change in the circuit load resistance caused by the breaking of the pencil lead (see paragraphs 18-21).

46. A value for the arrival time was obtained by projecting a line from the discontinuity to the IRIG trace (this line must be perpendicular to the baseline of both traces). The arrival time was then estimated by counting the number of cycles on the IRIG trace between zero time and the intersection of the projected line from the discontinuity (Figure 20).

Log displacement-time history

47. The flying log displacement-time history was obtained by using the magnetized steel wire and recording head apparatus described in paragraphs 26-28. The magnetized spots on the steel wire were 2 cm apart; as a spot passed the recording head, a voltage spike was produced. The resulting oscillogram trace is a series of spikes (Figure 21). To evaluate the trace, a line drawn perpendicular to the trace was projected from the spike to the baseline constructed from the IRIG trace, thereby relating displacement to time. By following this procedure for each spike, a time-dependent history of log motion was produced.

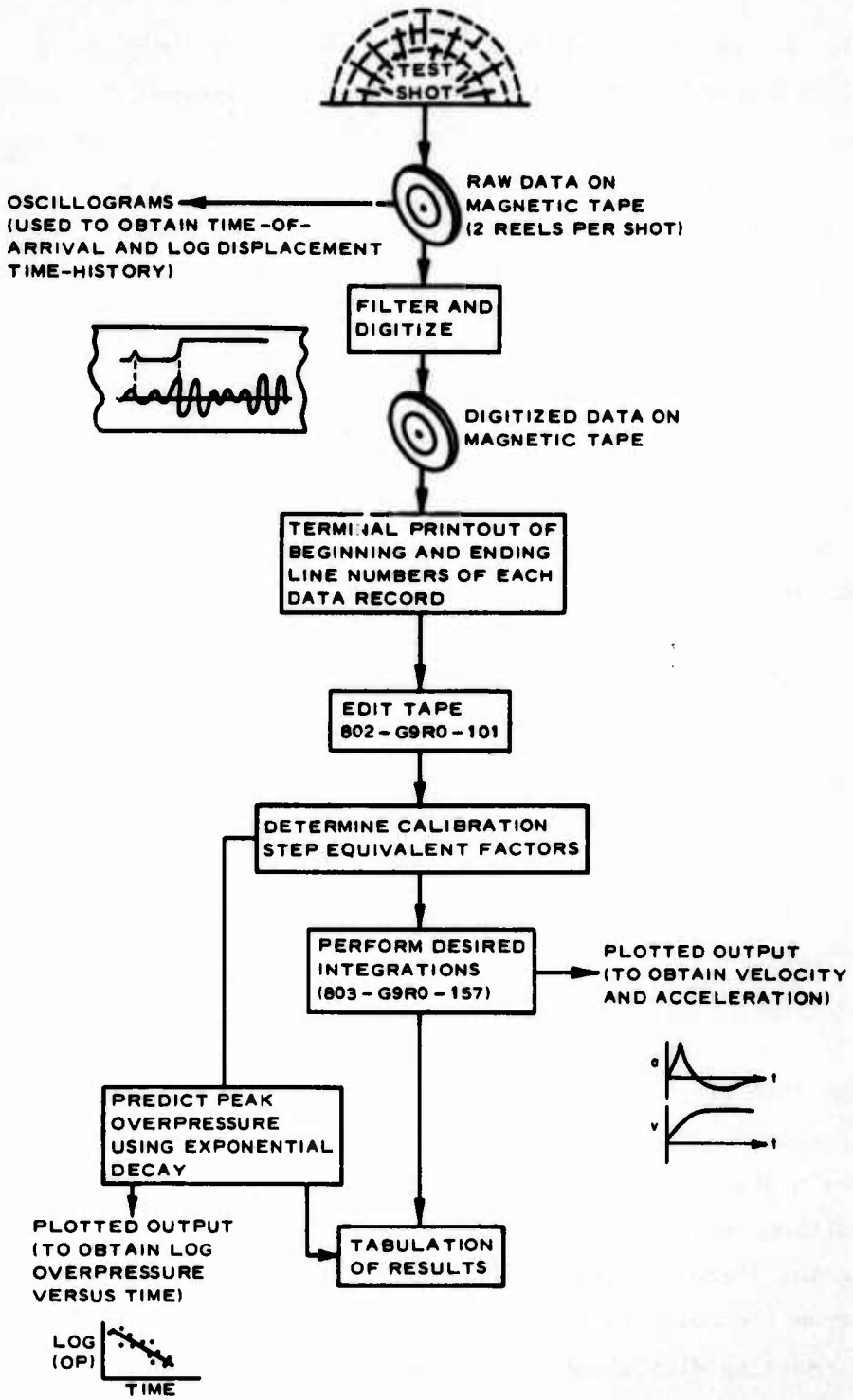

Figure 19. Data processing procedure

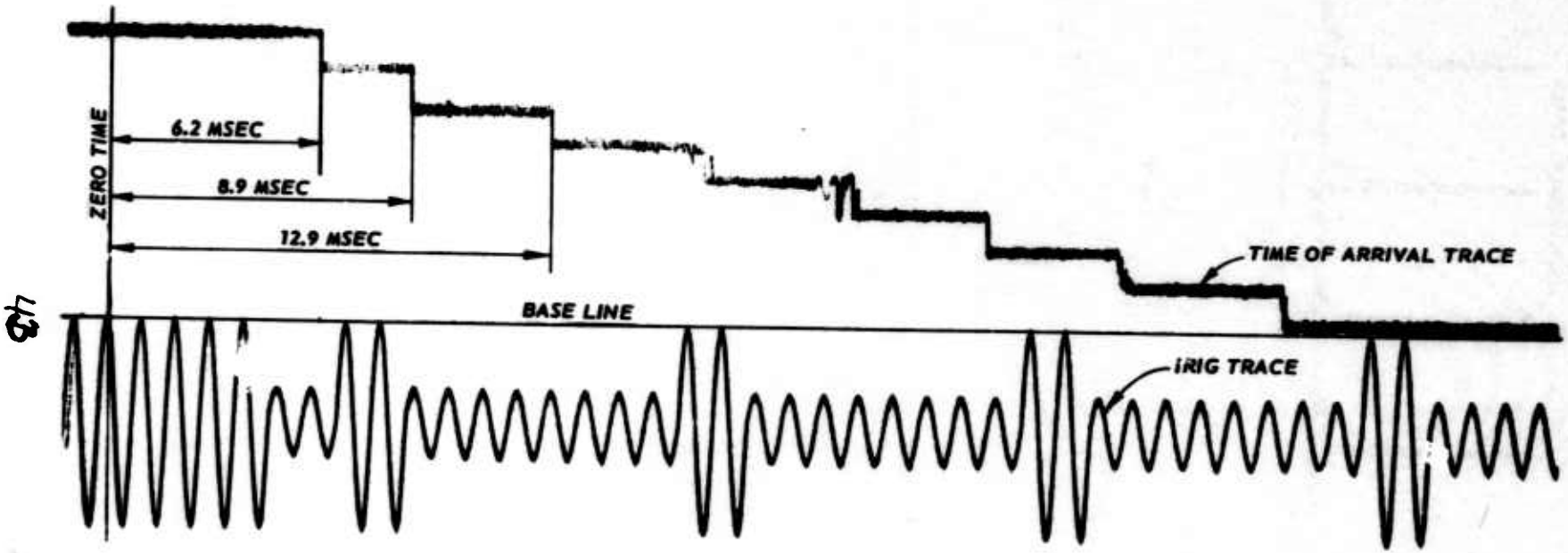

Figure 20. Illustration of method used to obtain arrival time (from test shot BB005)

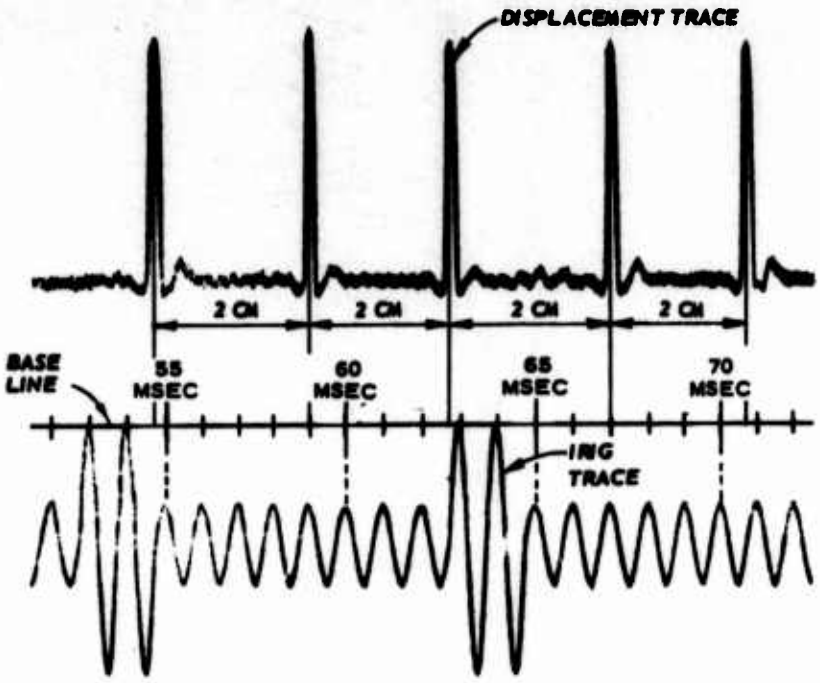

Figure 21. Method used to relate displacement and time using magnetized-wire apparatus (from test shot BB006). Time shown on baseline is the time after detonation

Continuous Data Records

48. Peak OP and the dynamic parameters associated with the motion of the instrumented logs were recorded on magnetic tape. The resulting information in each case is a continuous time-history record. Prior to each test shot, a signal that corresponded to a known value of the parameter to be measured was recorded on the parameter data channel. This signal is hereafter referred to as the "cal step." Parameters measured during a detonation could later be assigned numerical values by comparison with the cal step.

Filtering and digitizing records

49. Initial reduction of the time-history records from magnetic tape indicated that a substantial amount of high-frequency noise was present on each record. The magnitude of the problem was considerably reduced by filtering the data records (including cal steps) with a 10-kHz low-pass filter.

50. The filtered cal steps and data records were then digitized at 48 kHz and rerecorded on magnetic tape. Using an editing program (802-G9RO-101, WES computer library), the desired portions of the cal step and corresponding data records were printed from the magnetic tape. The printed output was then used with the cal step value to determine the conversion factor needed for each tape channel to change the digitized output units to the proper units of measurement recorded.

Integration of data

51. The filtered digital acceleration and velocity data were integrated using a previously developed program amenable to digitized data (803-G9RO-157, WES computer library). The results were printed in graphic format; sample outputs are shown in Figures 22 and 23. Figure 22 shows the acceleration data from an accelerometer mounted in the center of log 2, shot BB004; the integrated velocity and displacement are also shown. Figure 23 shows the results of measurements from a velocity gage in the center of log 2, shot BB003; these data were integrated to give displacement.

Prediction of OP

52. The initial oscillograms showing OP versus time were difficult to interpret and, as noted above, were filtered and digitized to aid in data interpretation. The shape of the resulting traces exhibited good agreement with theory; specifically, an almost instantaneous rise to peak OP was evident followed by a rapid initial decay in the general form of an exponential function with a negative exponent. The final part of the curve was characterized by a much slower (than exponential) decay until zero OP was attained.

53. Detailed examination of the initial portion of the traces, immediately following the OP rise, showed that the gages tended to overreact, thereby indicating OP's that were greater than the ones that actually occurred. This problem was eliminated by following the general methods developed by the Ballistics Research Laboratory for estimating peak OP.[7] This technique is used to to represent the OP data as a linear function of time and to estimate peak OP at the beginning of the positive phase duration. As noted in paragraph 52, the final

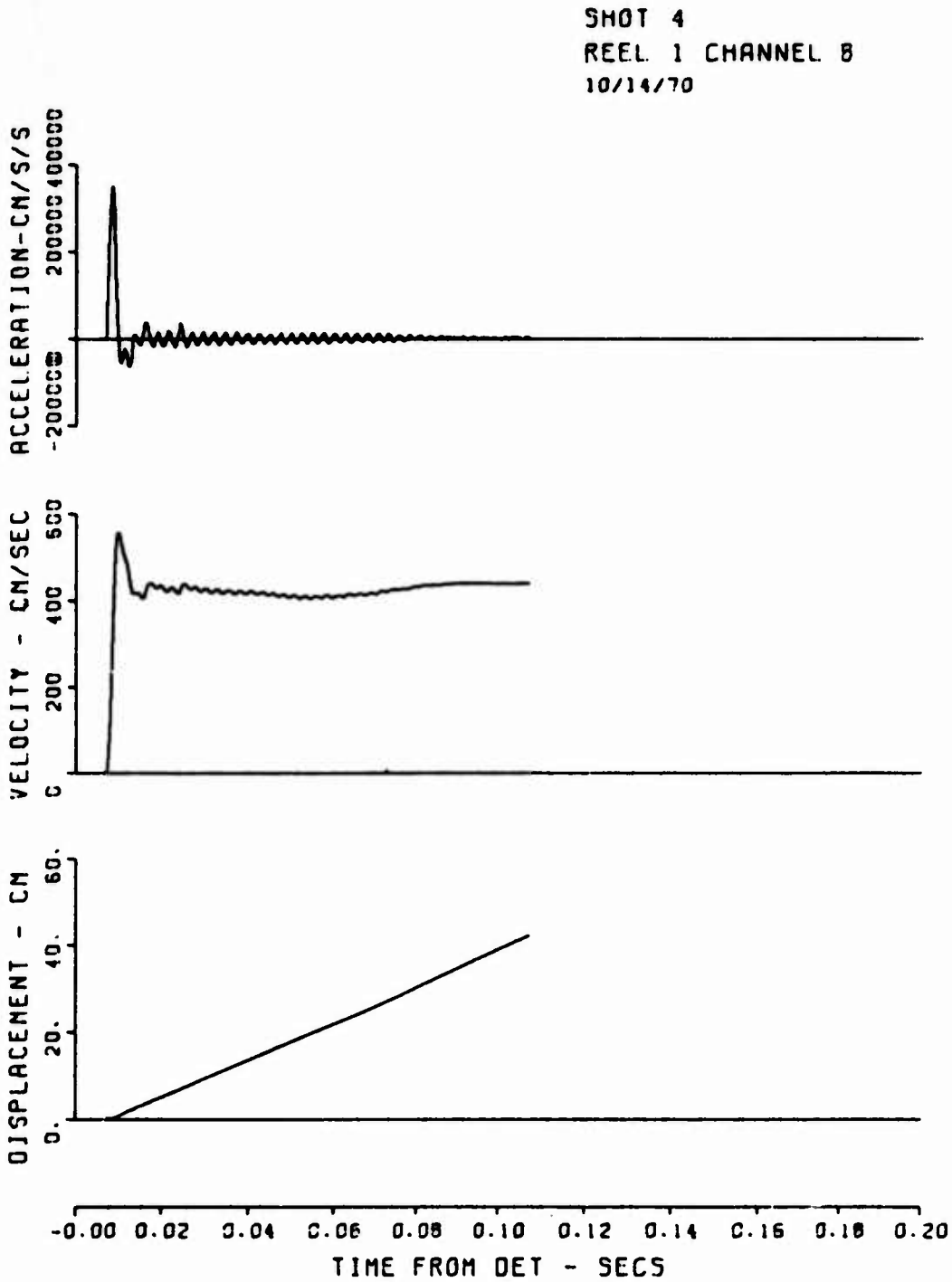

Figure 22. Velocity and displacement obtained from digitized acceleration data (from test shot BB004)

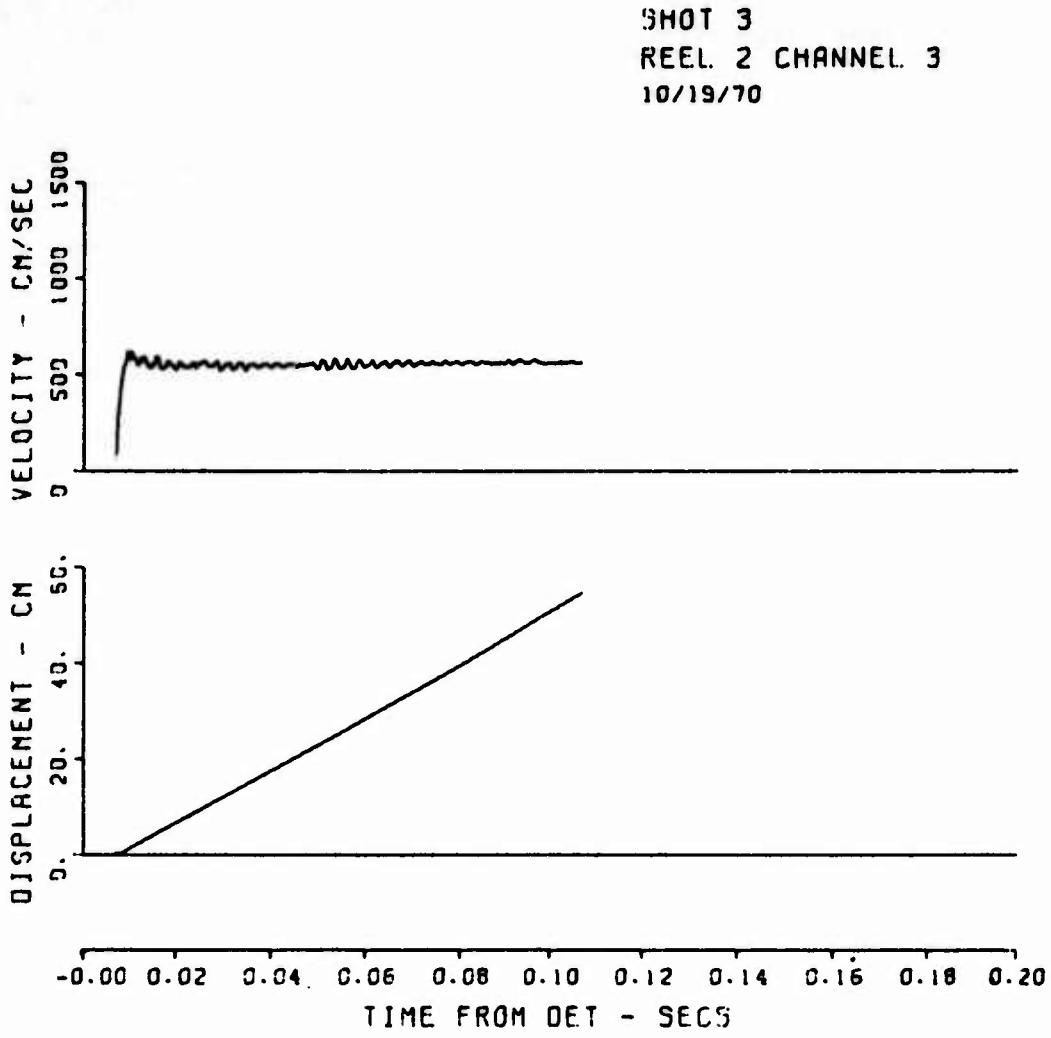

Figure 23. Displacement obtained from digitized velocity data (from test shot BB003)

portion of the OP decay did not have the same characteristic envelope as the earlier decay; therefore, the last two-thirds of the decay curve was deleted from the analysis. The remaining data were represented analytically in the following manner.

$$OP = A \times e^{-BT} \tag{1}$$

where

OP = overpressure, psi

A,B = constants for given data

T = time, msec

Taking the natural logarithm of Equation 1 yields

$$\ln (OP) = C - BT \qquad (2)$$

where $C = \ln A$. Equation 2 has a linear form. At $T = 0$, the intercept is

$$\ln (OP) = C$$

If an instantaneous rise time is assumed, the constant C and the logarithm of the peak OP are the same; the peak OP is then

$$OP = e^{C}$$

This method of estimating the peak OP represents minimum error introduced by the initial overreaction of the gage.

54. Constants B and C were determined for Equation 2 from a least-squares fit to the data points in the initial one-third of the pulse duration. Figures 24 and 25 show the raw oscillogram data, digitized and filtered data, and the OP estimated for 5.49 and 8.8 m, respectively, from GZ. Comparison of the estimated OP values and the predicted values is presented in paragraphs 73-77.

High-Speed Photography

55. High-speed motion picture records were made of each shot. These records were used, when possible, to determine the final velocities of the flying logs and to plot the visible shock front. As stated in paragraph 11, two noninstrumented logs were used. The ends of the logs were painted in alternating black and white quadrants. This technique provided a method of observing rotation around the longitudinal axis of the log and the displacement of the center of the log during free flight.

56. Log motion was analyzed with a Vangard Photographic Data Reduction Unit, Model M-16C, manufactured by Vangard Instrument Corp. Log displacement was determined by recording the x-y coordinates of the center of the flying log relative to a known fixed point. Timing

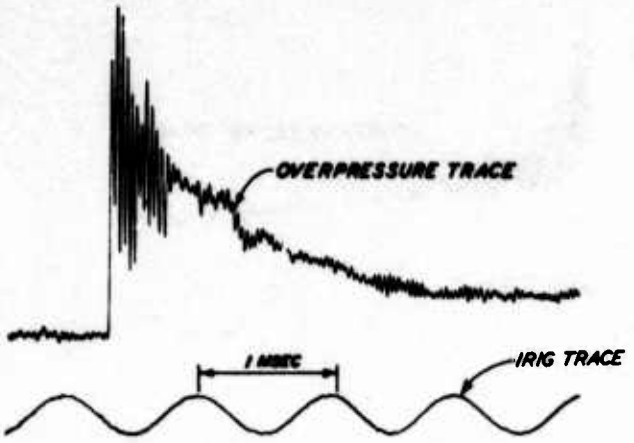

a. OSCILLOGRAM OF STATIC OVERPRESSURE TRACE

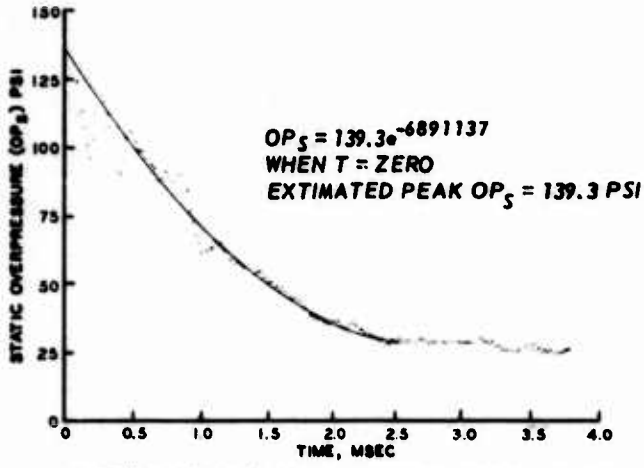

b. OVERPRESSURE TRACE FILTERED AND DIGITIZED

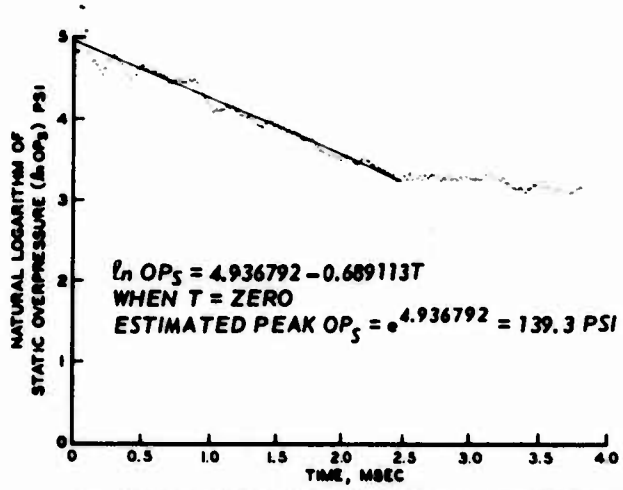

c. NATURAL LOGARITHM OF FILTERED AND DIGITIZED STATIC OVER PRESSURE DATA

Figure 24. Estimation of peak OP at 5.49 m from GZ

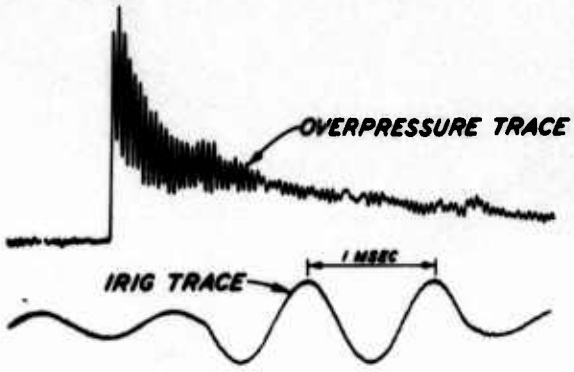

a. OSCILLOGRAM OF STATIC OVERPRESSURE TRACE

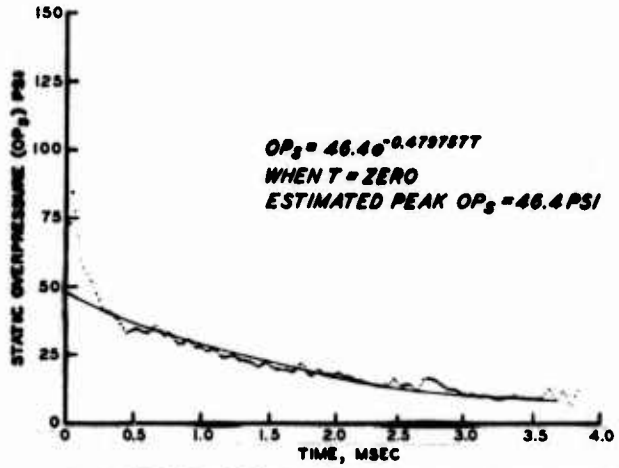

b. OVERPRESSURE TRACE FILTERED AND DIGITIZED

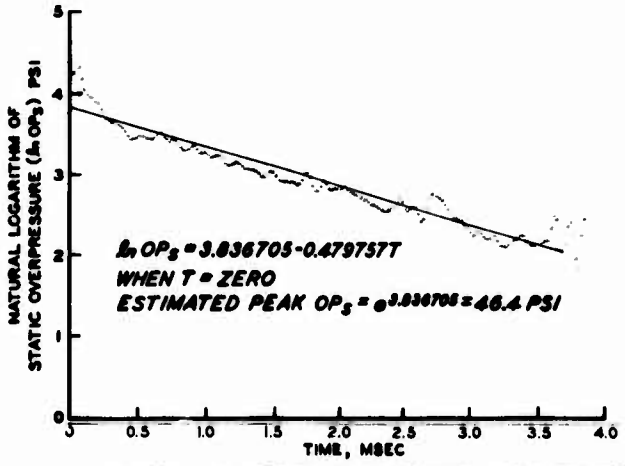

c. NATURAL LOGARITHM OF FILTERED AND DIGITIZED STATIC OVER PRESSURE DATA

Figure 25. Estimation of peak OP at 8.8 m from GZ

marks on the film in conjunction with the measured coordinates provided a time-history of the log's trajectory.

57. As stated in paragraph 37, three plywood backboards (1.2 by 2.4 m) were erected at the test site to study the shape of the shock front (Figure 13). These boards were positioned perpendicular to the camera and were painted with black and white diagonal stripes. This configuration and the variation in contrast of the forest in the background provided sufficient image distortion to locate the position of the shock front for test shots BB002, BB003, BB006, and BB007.* The shape of the shock front was analyzed with a Model 224-A Photo-Optical Data Analyzer manufactured by L-W Photo, Inc. With this unit individual frames can be viewed (Figure 26). The shape and position of the shock

Figure 26. Sample frame of high-speed photographic record

front for a given frame could be plotted relative to GZ by rapidly viewing adjacent frames. By selecting several frames during the time that the shock front was in the field of view, a succession of shock-front shapes could be plotted.

* The high-speed photography from test shots BB001, BB004, and BB005 was not of sufficient quality to be amenable to analysis.

PART IV: DATA ANALYSIS AND RESULTS

Quality of Test Data

58. Prior to validation of the theoretical loading function[1] by using results from the test shots, it was necessary to examine the quality of the data. It was decided that the following criteria must be satisfied before the data could be considered valid:

a. The frame of reference for each gage measuring displacement or each gage dependent on displacement for generation of data must remain fixed with respect to GZ while being acted upon by the shock front (this included all gages except the velocity gages and accelerometers mounted on the logs). This frame of reference could be distorted by both ground and air shock.

b. The shock front must be horizontally symmetrical,* i.e., there must be no jetting effects (see paragraphs 64-66 for explanation of jetting) that would generate abnormally high OP's for a given distance from GZ.

c. The data must be taken in the Mach stem** region. This is necessary because available data amenable to comparison are valid only in this region of the shock front. Also the loading function can accommodate only one rise and decay, i.e., above the Mach stem both the incident and reflected waves pass a given point.

d. The yield data must be compatible with those from accepted sources of blast data.

Stability of the frame of reference

59. Moving and fixed frames of reference (with respect to GZ) were used in the test program. The flying logs instrumented with velocity and acceleration gages used a moving frame of reference. Experimental equipment, the measurement capability of which depended on a fixed frame of reference, included the displacement-time apparatus, TOA gages, and OP gages. As mentioned in Part II, each gage was mounted so that effects caused by its translation or vibration with respect to its frame of reference were minimized. A gage and its

---

* Circular in shape as viewed in the horizontal plane.

** The shock front formed by the fusion of the incident and reflected shock fronts from an explosion; see Reference 6.

respective frame of reference must remain fixed with respect to each other; otherwise, measurements will be with respect to the frame of reference of the gage and will have no meaning with respect to the fixed frame of reference of the experiment, i.e., with respect to GZ.

60. Supporting hardware for the fixed frame of reference experimental apparatus was fabricated according to one of two techniques.

a. The TOA gages (Figure 7) and some of the OP gages (Figure 6) were mounted between the source of the airblast and the support hardware so that the gage was acted upon by the shock front before the support hardware. This method allowed the data to be taken before any vibration or translation of the support hardware could take place.

b. The superstructure of the support apparatus for each displacement-time gage (Figures 4a and 13) was designed to withstand any effects caused by the incident shock front. Detailed surveys after each shot showed no displacement of any rigid support apparatus at 8.8 m from GZ. Survey accuracy was better than 1.5 mm. Tests BB006 and BB007 were arranged so that the distance from GZ was less than 8.8 m for the galvanized-pipe support apparatus (paragraphs 39 and 40). No displacement or structural damage was noted after shot BB006 (OP of 200 psi); however, the support apparatus did fail during shot BB007 (OP of 700 psi; see Figure 17).

61. Although the methods of fabricating the support hardware described above were effective against airblasts, the possibility had to be considered that the compression wave induced in the earth by the explosion might travel ahead of the shock front and invalidate mounting method a, paragraph 60, i.e., vibration of the aluminum poles used to support the TOA gages might break the pencil lead (paragraphs 18-21) before the shock front arrived, or vibration of the stands used to support the OP gages might generate erroneous OP data (see paragraph 17). To investigate the magnitude of this problem, a seismic refraction survey (paragraph 5) was conducted prior to test shot BB001. Results showed that the compression wave velocity in the near-surface layer was 300 m/sec. At 8.8 m from GZ (location of gages for most tests), the shock-front velocity for a 0.09-metric-ton yield had decayed to a predicted value of 643 m/sec; therefore, prior to initial testing it

seemed probable that earth motion was of no consequence. This assumption was verified by the earth-movement canister placed at 8.8 m from GZ for tests BB001 and BB002 (see paragraphs 23 and 34). For test BB001, the TOA gages indicated that the shock front arrived at 8.8 m from GZ at 6.125 msec (average) after detonation; the earth-movement canisters were activated no earlier than 8.0 msec and as late as 11.0 msec. For the second test, the TOA gages indicated that the shock front arrived at 8.8 m at 6.7 msec (average) after detonation; the earth-movement canisters were activated no earlier than 7.8 msec and as late as 10.8 msec. Therefore, earth motion had no effect on the gages during the period when data were being taken.

62. Further experiments to study the effects of earth motion were conducted during shot BB005. Three TOA gages were placed in cylindrical cavities as described in paragraph 38; following the detonation, the gages were examined. None of the pencil leads in the TOA gages were broken, indicating that earth motion did not affect the performance of the gages.

63. Based on the results of the investigation discussed above, it was believed safe to assume that earth motion induced by the explosions had no effect on the quality of the data for this test series.

Shock-front
symmetry in horizontal plane

64. The shock front resulting from a detonation must be proven to be symmetrical in the horizontal plane (circular) so that all data taken at the same distance from GZ can be interpreted with equal weight. The major phenomenon that destroys the symmetry of a shock front is referred to as "jetting."

65. Generally, jets occur close to GZ and are a result of some of the explosive material being displaced before reacting. At some time later, the detonation catches up with the explosive material and produces a jet (sometimes luminous). Associated with the jet is an OP that is greater than would normally be anticipated at that distance from GZ.

66. The effects due to jetting were analyzed by evaluating arrival times at different azimuths but at the same distance from GZ. Equal arrival times indicated that the shock front was symmetrical in the horizontal plane, and there was no detectable jetting. Arrival-time data were available from two sources, the TOA gages and the activation time of the OP gages. Tables 6 and 7 show a complete compilation of TOA and OP gage data, respectively, for the entire test series. All TOA data in which there were at least two measurements at the same radial distance from GZ were complied from Table 6 and listed in Table 8. A similar compilation was not prepared from Table 7 because of the variable response times of the OP gages; however, Table 7 is presented for completeness and general interest.

67. Table 8 contains the TOA data for test shots BB001 and BB002. For test shot BB001, four TOA gages were spaced 90 deg apart, all at 8.8 m from GZ. Arrival times of 6.1, 6.2, 6.2, and 6.0 msec were recorded. The small differences in arrival time indicate that symmetry was almost achieved in the horizontal plane at 8.8 m. These differences should be considered within the limits of experimental error.

68. Symmetry in the horizontal plane was studied in greater detail during the second test, BB002 (see paragraph 35). In addition to the four TOA gages used in BB001, two strings of gages were added to the test configuration. These strings were perpendicular to each other. The TOA gages were spaced such that the estimated travel time of the shock front from one gage to the next would be 2 msec. The results are presented in Table 8. The symmetry distortion was again evaluated by comparing arrival times for gages at the same radial distance from GZ. A 10 percent variation in TOA is not unreasonable to expect for two gages placed at the same distance from GZ for a given shot. The data in Table 8 meet this criterion, indicating that the shock front propagated away from GZ in a nearly symmetrical manner.

Shape of the shock front
in the vertical plane and
the path of the Mach stem

69. Several experiments were included in the test program to study the shape of the shock front in a vertical plane passing through GZ and the path of the Mach stem. Data on the shape of the shock front in a vertical plane were required if it became apparent that the plane-wave shock front used in the original loading function did not correctly simulate the actual shock front. Study of the Mach stem path was necessary to verify that the data were taken in the Mach stem region; data taken above the Mach stem could not be scaled to other yields,[6] i.e., the scaling laws are valid only in the Mach stem region. In addition, the loading function is valid only in the Mach stem region.

70. A shock wave generated by an explosion in air is approximately spherical. If the explosion is close to the ground, a Mach stem develops as soon as the shock wave strikes the ground. Since the velocity of the Mach stem away from GZ is slightly greater than that of the incident shock wave, the shape of the shock wave-Mach stem combination, as viewed in a vertical plane passing through GZ, is a complex curve, with a breakpoint (called the triple point) at the junction between the Mach stem and the incident shock wave (Figures 27 and 28).

71. Experiments to examine the inclination of the shock front were conducted during shots BB001 and BB002 (see paragraphs 33 and 34). Pairs of TOA gages were placed at the same distance from GZ, but at different elevations (see Table 4 and Figure 7b). For the shock front to be spherical in nature, the lower TOA gage of a pair should be activated before the upper gage. The resulting data are presented in Table 9. The majority of the data were lost in shot BB002 because of circuit failure. The three pairs of data that are valid for each shot show that the lower TOA gages were indeed activated first, indicating that the shock front was inclined toward GZ.

72. Photography suitable for analysis of the shape of the shock

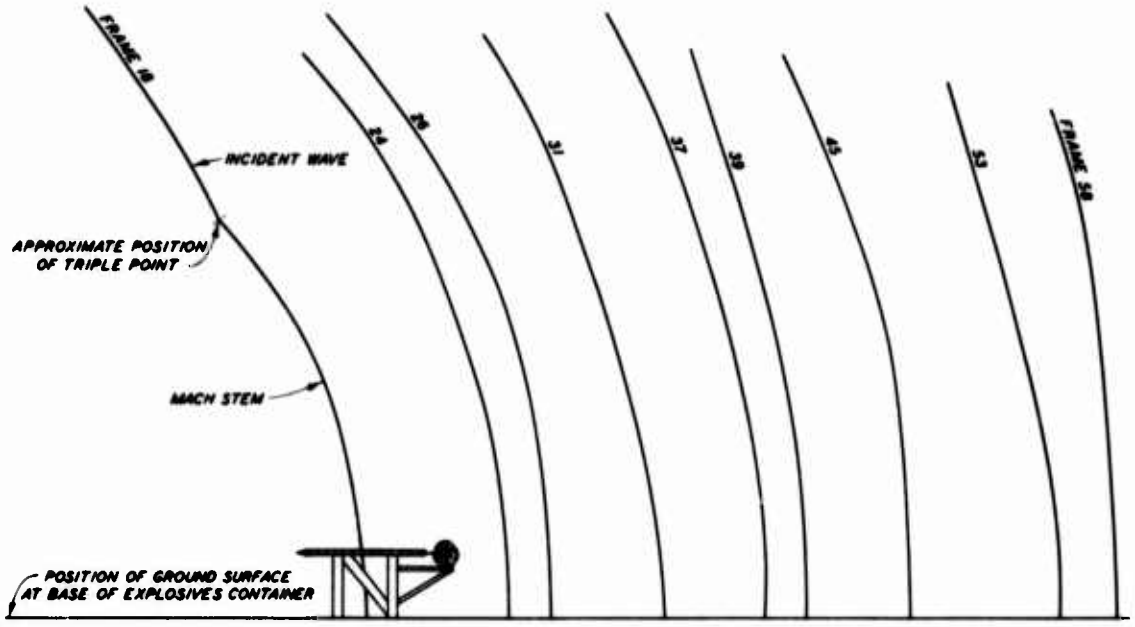

a. SHOT NO. BB002 - DATA OBTAINED FROM BLACK AND WHITE FILM EXPOSED AT 7859 FRAMES PER SECOND

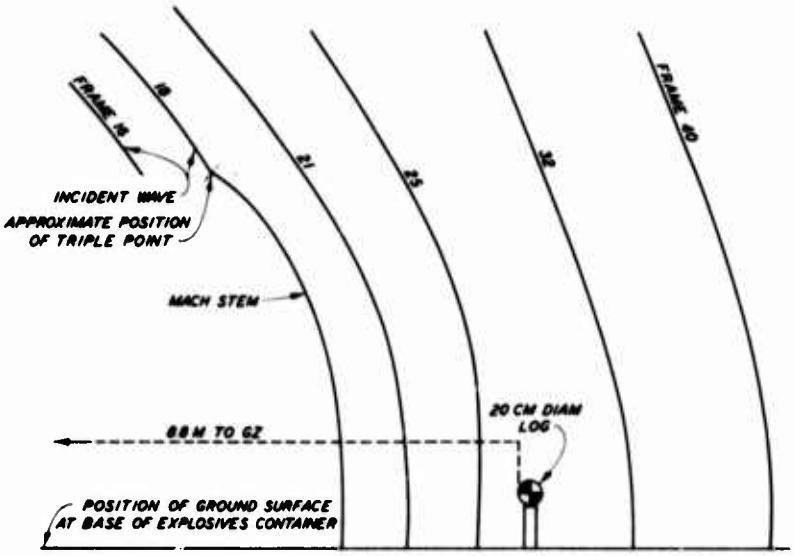

NOTE:
1. ALL HORIZONTAL DISTANCES FROM GZ ARE ACCURATE IN PLAN VIEW, BUT ARE ONLY APPROXIMATE IN THE FIELDS OF VIEW SHOWN.
2. FRAME NO'S REFER TO THE NO OF 16 MM FILM FRAMES EXPOSED SINCE DETONATION.

b. SHOT NO. BB003 - DATA OBTAINED FROM COLOR FILM EXPOSED AT 2000 FRAMES PER SECOND

Figure 27. General shape of shock front for test shots BB002 and BB003

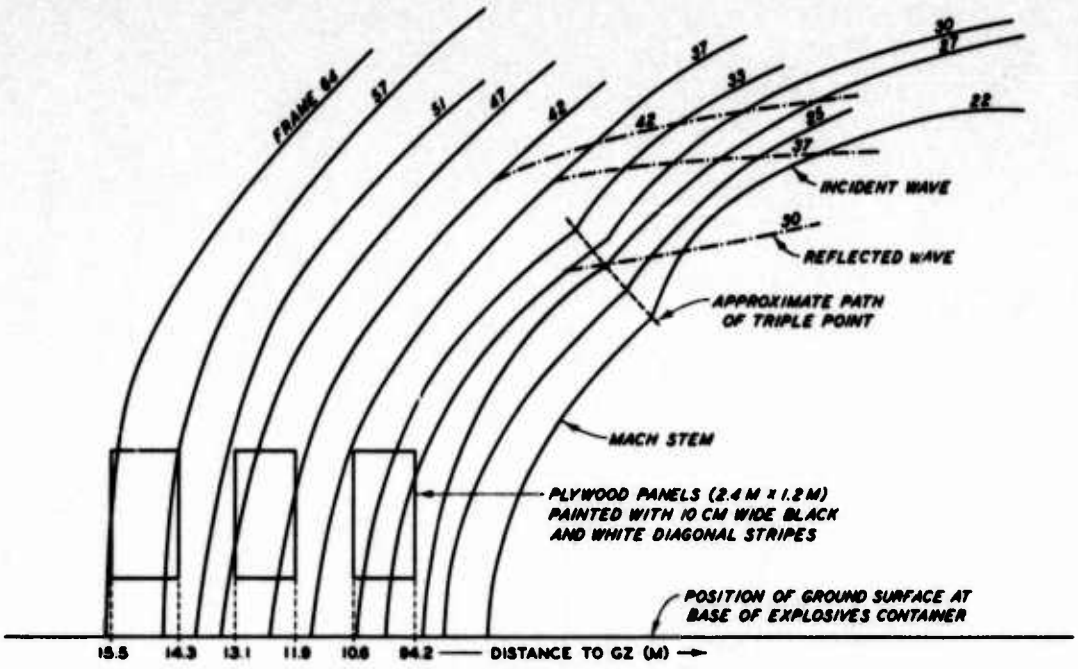

a. SHOT NO. BB006 - DATA OBTAINED FROM COLOR FILM EXPOSED AT 5210 FRAMES PER SECOND

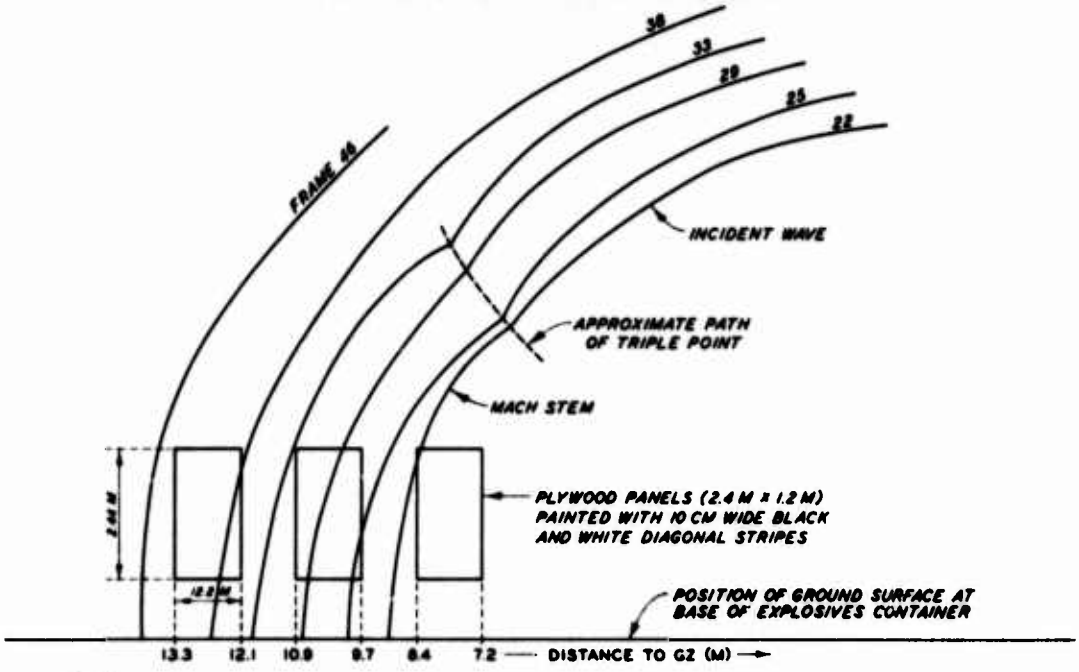

NOTE:
1. ALL HORIZONTAL DISTANCES FROM GZ ARE ACCURATE IN PLAN VIEW, BUT ARE ONLY APPROXIMATE IN THE FIELDS OF VIEW SHOWN.
2. FRAME NO'S REFER TO THE NO. OF 16 MM FILM FRAMES EXPOSED SINCE DETONATION.

b. SHOT NO. BB007 - DATA OBTAINED FROM COLOR FILM EXPOSED AT 5150 FRAMES PER SECOND

Figure 28. General shape of shock front for test shots BB006 and BB007

front was obtained for test shots BB002, BB003, BB006, and BB007.* The framing rates were 7859, 2000, 5210, and 5150 f/s, respectively. The shock-front shapes were constructed using the methods described in paragraph 57. The shapes of the shock fronts as they propagated away from GZ for shots BB002, BB003, BB006, and BB007 are shown in Figures 27 and 28. The path of the triple point is sufficiently obvious, at least in Figure 28, to conclude that all measurements of shock-front TOA, OP, ground motion, and log motion were obtained in the Mach stem region.

Compatibility of yield
data with accepted source data

73. The experimental yield data were compared with the following accepted data sources:

a. Ballistics Research Laboratory (BRL) OP test data,[3] which were scaled from 3.6- to 0.09-metric-ton yield.

b. Air Force Weapons Laboratory (AFWL) test data,[4] which were scaled from normalized data.

c. Naval Ordnance Laboratory (NOL) test data,[5] which were scaled from normalized data.

74. These sources were selected for comparison for the following reasons:

a. The BRL data were scaled down from data that were in good agreement with data acquired at Fort Benning.[1] After the Fort Benning test, the BRL data were used to generate the generalized stem-failure criterion and to structure the loading function.

b. The AFWL test data were acquired from the detonation of a 0.45-metric-ton spherical charge of TNT, with the height of burst being 4.57 m; 4.57 m scales down to 1.33 m for 0.09-metric-ton TNT yield. This value (1.33 m) is very close to the height of burst used for the test series described herein (0.72 m).

c. The NOL test data were valid for a spherical charge in free space, i.e. so far above the ground that no Mach stem forms. These data were used only to compare the shock-front characteristics of a free-space explosion with those of an explosion at a finite height above ground where a distinct Mach stem was formed.

---

* The high-speed photography from test shots BB001, BB004, and BB005 was not of sufficient quality to be amenable to analysis.

75. Peak OP and TOA for each of the above sources were scaled to 0.09-metric-ton TNT yield. The scaled values are plotted in Figures 29 and 30, respectively. The WES TOA and OP data are in good agreement with the data from the other sources. The compatibility of data on both plots indicates that the desired energy yields were obtained from the AN/FO explosives, and that existing cube-root scaling laws may be applied with confidence to yields as low as 0.09-metric-ton TNT.

76. The NOL data appear to produce a lower OP and later arrival time than the other available data. This is because the other data are measured in the Mach stem region, and the NOL data are valid only for free space, i.e., the Mach stem is the composite of both the incident and reflected waves, whereas the NOL data result from the incident shock front only. The major differences appear to be close to GZ; however, at large distances from GZ, the differences become much smaller. The BRL, AFWL, and NOL data shown in Figures 29 and 30 were standardized such that they are independent of temperature and barometric pressure.

77. Numerical comparison of WES and BRL TOA and OP data are shown in Tables 10 and 11, respectively. These data were not corrected for variations in meteorological conditions. Variation in the barometric pressure is insignificant for the data shown in both tables. Temperature introduces insignificant error at 8.8 m and beyond. The available data indicate that approximate symmetry of the shock front was achieved in the WES test shots at about 5.5 m. However, the fireball normally extended out to about 8.0 m (Figure 31).

78. Existing methods of predicting TOA and OP are valid only when the available energy is entirely kinetic, i.e., outside the fireball. This kind of correction cannot be applied inside the fireball, since in that situation chemical reactions are continuing and adding heat energy to the expanding gases. The kinetic instabilities resulting from this situation make it invalid to apply normal temperature corrections to the region inside the fireball, which in the case of the WES tests implies any distance less than about 8.0 m. Thus, even though the shock front appears to have attained symmetry at about 5.5 m (which is generally regarded as the distance from GZ beyond which normal TOA and OP

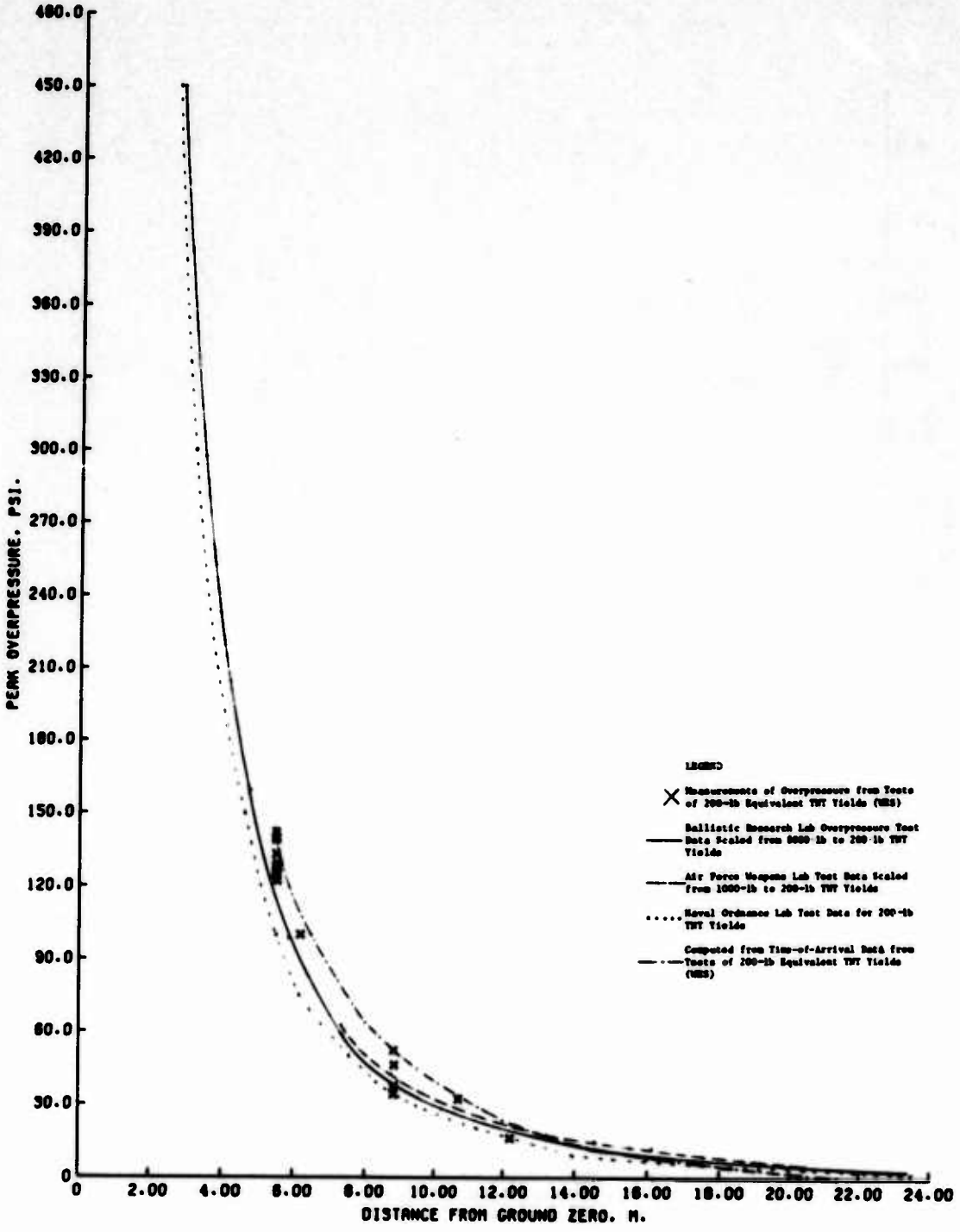

Figure 29. Peak OP versus distance from GZ for selected data

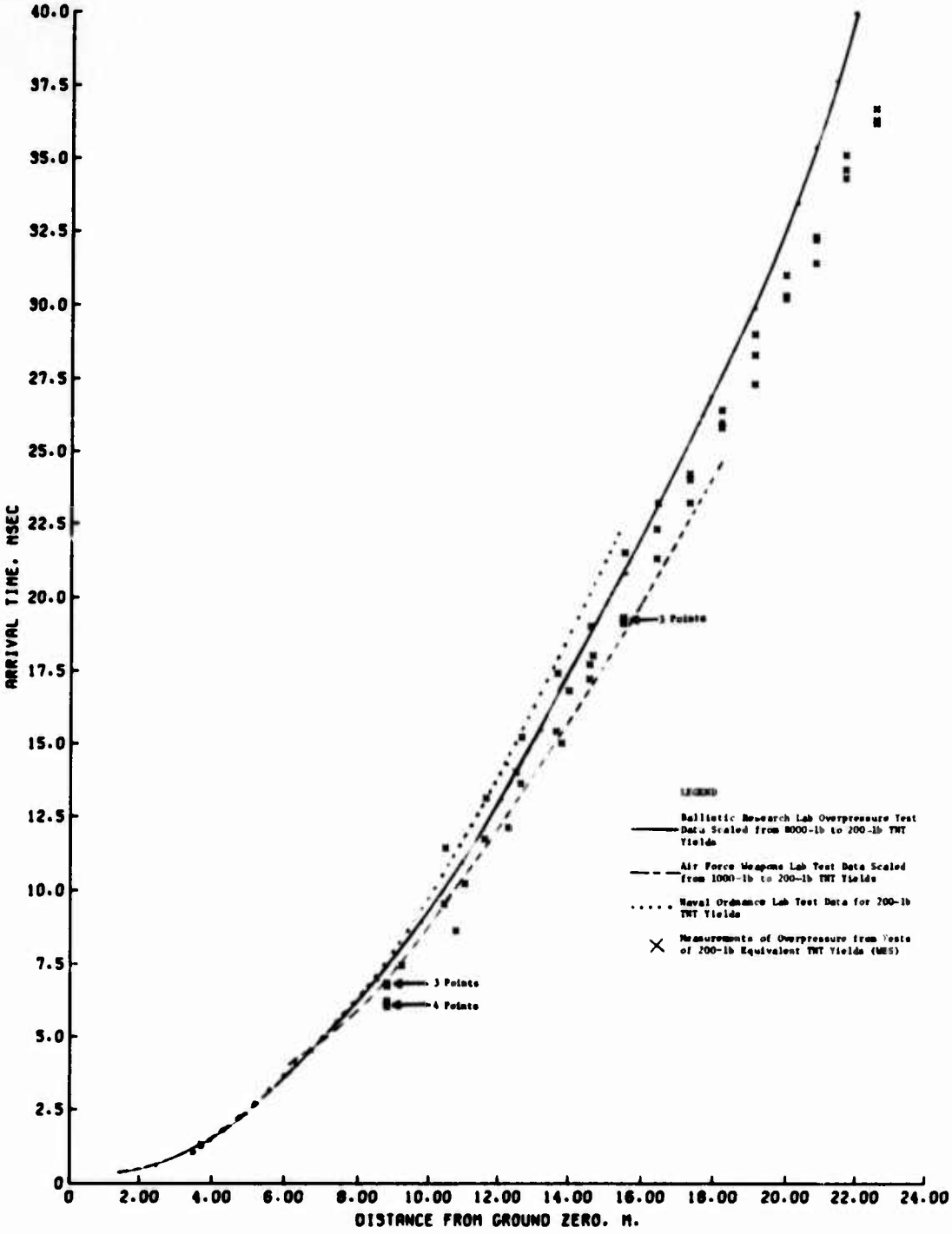

Figure 30. Arrival time versus distance from GZ for selected data

Figure 31. Explosion of test shot BB002. Fireball has expanded to maximum value of approximately 8.0 m

prediction methods could be reliably used), the TOA's and OP's in the annulus between 5.5 and 8.0 m cannot be reliably predicted.

79. Of the 56 TOA measurements obtained at distances from 8.8 m up to 22.5 m, 89 percent are within 10 percent of the values determined from the BRL data (Table 10). Of the 17 peak OP values determined from the WES experiments, 82 percent are within 15 percent of peak values obtained from BRL data, and 100 percent are within 21 percent of the BRL values (Table 11). A 20 percent variation in peak OP measurement is not uncommon for similar gages placed at the same distance from GZ for a given shot.

80. To evaluate the compatibility of the WES TOA data and OP data, the TOA data were converted to OP data as follows: The distance from GZ was plotted versus TOA using all valid data. A least-squares polynomial equation was generated using these data. The derivative of this equation yields the instantaneous velocity of the shock front for a given arrival time. This arrival time corresponds to a given distance from GZ; hence, the shock-front velocity can be plotted as a function of distance from GZ. The Rankine-Hugoniot equation for shock-wave velocity (V) in the Mach stem region is[5]

$$V = C_o\left(1 + \frac{6P}{7P_o}\right)^{1/2} \qquad (3)$$

where

C_o = velocity of sound at ambient temperature

P = peak overpressure

P_o = ambient atmospheric pressure

Rearranging Equation 3 yields

$$P = \frac{7P_o}{6}\left[\left(\frac{V}{C_o}\right)^2 - 1\right]$$

Therefore, a curve of peak OP versus distance from GZ can be plotted (distance from GZ is a function of velocity as stated above). This curve is shown in Figure 29 along with measured WES data, and BRL, AFWL, and NOL peak OP data. The curve appears to be in good agreement with the other curves.

Summary

81. The data obtained during the WES test series agree with theory within anticipated instrumental and observational error based on the conditions specified in paragraph 58, i.e., the frame of reference of each sensor was not influenced by the incident shock, the shock front exhibited symmetrical propagation characteristics, all data were taken in the Mach stem region, and yield data from the WES test series are compatible with yield data from accepted sources of blast data.

Validation of Tree Stem Loading Function

82. The major objective of the test program was to validate the theoretical loading function used in the solution of the partial differential equation (PDE) describing the dynamic deformation of a right-circular cylindrical beam, i.e. the dynamic motion of an individual tree stem being acted upon by a shock front.[1] The solution of the PDE was required in order to relate the geometric stem curvature required

for stem failure to the height on the stem (remnant height) at which failure occurs. Development of the stem failure criterion and solution of the PDE are discussed in Appendix A. Using the failure criterion and the PDE solution, a nomographic technique was developed for estimating stem-remnant height at a given distance from GZ for wide variations in stem properties and weapon yields. The development of this procedure is described in Appendix B.

83. The tree stem discussed above is represented in this validation by the logs used in this test program (see paragraph 9). The loading function was validated by considering the momentum transfer per unit length of the log between the shock front and the log during the positive pulse duration of the shock front, i.e.

$$M = \int_0^{T_p} F(x,t)\, dt \qquad (4)$$

where

M = momentum transfer per unit length of the log

T_p = length of positive pulse duration

$F(x,t)$ = loading function that characterizes the dynamic loading of the log by the shock front (see Appendix A for derivation of loading function)

Integration of Equation 4 by expressing $F(x,t)$ as a change of momentum with respect to time yields

$$M = \frac{m}{\ell} (V_f - V_i) \qquad (5)$$

where

m = mass of log

ℓ = length of log

V_f = velocity of log at end of positive pulse duration (referred to herein as final velocity)

V_i = velocity of log at beginning of positive pulse duration

V_i was always zero for the WES test series because the logs were at rest when the shock front initially came in contact with them. Experimental data for V_f are available from the field procedures previously discussed in paragraphs 47, 51, 55, and 56; also see paragraphs 86-91. A theoretical prediction for V_f can be obtained by integrating Equation 4, using the derived loading function; the resulting value of M can be equated with Equation 5 to obtain the desired theoretical value of V_f. Agreement of the experimental and theoretical values of V_f for the same data will validate the loading function.

Theoretical determination of V_f

84. Integrating Equation 4 using the derived loading function (see Appendix A) shows that momentum transfer per unit length is

$$M = 2rJ_T \tag{6}$$

where

r = radius of the stem

J_T = the total effective pressure impulse; see paragraphs 29 through 38 of Reference 1 for discussion of the total effective pressure impulse

J_T can be calculated from

$$J_T = JC_d + P_r\left(\frac{2r}{U}\right) \tag{7}$$

where

J = dynamic pressure impulse

C_d = drag coefficient of stem

P_r = reflected pressure

U = velocity of shock front

JC_d is generated by the air drag on the stem within the shock front; P_r is due to a pressure differential generated between the side facing the incident shock front and the lee side of the tree stem; and $2r/U$ is the shock-front transit time across the stem. The derivation of

Equation 7 is shown in Reference 1 on pages 25 and 26. The last term in Equation 7 can be expressed in terms of known values of the dynamic pressure impulse (J_B) as follows

$$P_r\left(\frac{2r}{U}\right) = 0.5J_B \tag{8}$$

For a stem radius of 10 cm,* the term $P_r(2r/U)$ was calculated using OP values from Figure 8 of Reference 1. The results indicate that for a given distance from GZ, the calculated value of $P_r(2r/U)$ is equal to approximately one-half the corresponding dynamic pressure impulse (also shown in Figure 8). To satisfy any stem diameter, both terms in Equation 8 can be multiplied by the term $r/10$. According to cube-root scaling laws, the dynamic pressure impulse can be computed for any weapon yield (W) for a given distance from GZ if the value for the dynamic pressure impulse (J_B) is known for another yield (W_B) at the same distance from GZ, i.e.

$$J = J_B\left(\frac{W}{W_B}\right)^{1/3} \tag{9}$$

Substituting Equations 8 and 9 into Equation 7 and the resulting value of J_T into Equation 6 yields

$$M = d\left[J_B \times C_d + \frac{1}{40\left(\frac{W}{W_B}\right)^{1/3}}\right] \tag{10}$$

where $d = 2r$. Equating Equations 5 and 10 and solving for V_f yields the desired theoretical final velocity:

$$V_f = J_B\left[C_d + \frac{d}{40\left(\frac{W}{W_B}\right)^{1/3}}\right]\frac{d\ell}{m} \tag{11}$$

---

* Arbitrarily selected value; any real number can be used.

85. A sample calculation to obtain a theoretical value of V_f (Equation 11) is shown below using typical physical properties of the logs used in the WES test series (compiled in Table 12). Consider shot BB001, log 1:

$m = 9054$ g

$\ell = 111.8$ cm

$d = 10$ cm

Also

$J_B = 2434$ dyne × sec/cm^2 (predicted dynamic pressure impulse at 8.8 m from GZ for a 0.09-metric-ton yield)

For all calculations of V_f

$W = 0.09$ metric ton

$W_B = 3.6$ metric tons*

$C_d = 0.75$**

Then

$$V_f = 2434\left[0.75 + \frac{10}{40\left(\frac{0.09}{3.6}\right)^{1/3}}\right]\left(\frac{10 \times 111.8}{9054}\right)$$

$$= 481.8 \text{ cm/sec}$$

Experimental determination of V_f

86. The final velocity (V_f) was obtained experimentally from 13 logs. As stated in paragraph 12, each of the logs was 111.8 cm long, was either 10 or 20 cm in diameter, and varied in mass from 9,054 to 36,083 g. Twelve had rough, natural surfaces and one had a smooth surface. The logs were instrumented to measure displacement, velocity, or acceleration. Some logs were instrumented to measure more than one of

---

* See Figure 8 of Reference 1.

** Predicted drag coefficient for a cylinder with a surface similar to that of a log.

the parameters. The displacement measurements were taken from three different sources: (a) shot BB001, log 1 and log 2 data were obtained from the displacements measured on high-speed movies of the blast; (b) shot BB002, log 1 data were taken from the wire-breaker device; and (c) the displacement data for shots BB003-BB006 were taken from the magnetic wire-displacement apparatus. The derivative of the displacement-time data yielded the desired final velocity. Velocity data were also obtained from direct output of the velocity gages. The acceleration records were integrated when possible to obtain velocity data.

87. Eleven of the logs from which experimental velocity data were obtained were statically positioned at 8.8 m from GZ prior to detonation; one was at 12.2 m, and one was at 4.4 m (paragraphs 33-40). These data for each log, plus the theoretically calculated and experimentally measured horizontal velocities, are shown in Table 12. Experimental data are shown for gages positioned in the center and in both ends of the log. A value that can be interpreted as the representative horizontal velocity of the center of mass of the log was calculated by using simple or weighted averages. The averages were obtained by classifying the horizontal velocity data into one of the following categories:

a. One or more values at only one of the three gage positions.

b. One or more values at both end mounting positions, but not at the center.

c. One or more values at each of the three mounting positions.

The representative horizontal velocity of the center of mass of the log was then obtained in the following manner: Category a data were averaged. A value was obtained for category b data by averaging all data at each end, and then averaging the resulting end values. A weighted value was obtained from category c data by averaging the data at each position. The end values were averaged; the result of this average was averaged with the average center value to obtain the representative velocity.

88. Initial inspection of the measured horizontal velocities for the 12 logs with natural surfaces (Table 12) indicates the following:

a. The measured horizontal velocity was somewhat higher when obtained from a velocity gage than from an accelerometer gage when data are compared from gages mounted at the same position on the log.

b. The horizontal velocity appears to be different at opposite ends of logs that had instrumentation on both ends.

c. The difference in the log velocities at either end of the log appears to be minimized when displacement-time gages are used.

89. The data in Table 12 indicate seven instances in which velocity gages measured higher values than those measured by accelerometers for the final log velocity. Even though this is not enough data to rigorously analyze the problem, some speculation is possible. Errors due to integration or an insufficient sample of the acceleration-time record were initially eliminated. Errors due to nonrigid mounting were possible, i.e., the gages' frames of reference were not fixed with respect to one another; however, the most probable cause of the higher values is the rotation of the log disturbing the calibration of the velocity gages.

90. Rotation of the log was noted (high-speed photography) about the vertical and lateral axes of the log, but not about its longitudinal axis. Rotation about the two axes was probably due to nonsymmetrical loading of the log (variation in OP across the face of the log), variation in the drag coefficient on the loading surface, or the center of mass of the log being different from the geometric center of the log. The rotational motion induced by one or more of the above parameters most likely accounts for the differences in the horizontal velocities.

91. The displacement-time gages produced the most consistent results (see Table 13) i.e., the horizontal end velocities agree more closely than those velocities determined from accelerometer and velocity data. The possibility should be considered that the drag of the magnetized wire on the Teflon guide (paragraph 28) reduced the difference in the end velocities. The coefficient of kinetic friction for Teflon is close to zero, thus drag of the magnetized wire in the Teflon was probably insignificant and was assumed to be so in computing final log velocities. The quality of data generated, plus low cost and ease

of installation (as compared with velocity gages and accelerometers mounted in the logs), indicates that a displacement-time apparatus is the optimum configuration for obtaining impulse data from free-flying logs.

Comparison of theoretical and experimental data

92. Figure 32 is a comparison of theoretically predicted and experimentally measured final velocities for 13 logs put into free flight by impulse loading from a passing shock front.* The predicted values were computed with Equation 11. The linear relation shown on the graph indicates that the measured velocities are somewhat higher than the predicted velocities (note that the slope of the line is not unity). However, if a higher value were used for the drag coefficient, the predicted values could be adjusted for a match. The predicted velocity for the smooth log is too high. Therefore, the drag coefficient would have to be lowered to adjust for a match. Thus, the drag coefficient used to calculate the predicted final velocities (0.75) shown in Figure 32 is too low for logs with a rough surface and too high for a log with a smooth surface. If it is assumed that the pine logs are rough compared to the majority of tree species, 0.75 may be a good compromise. The large cluster of points in Figure 32 represents data collected on logs of two diameters when the incident OP was 40 psi. Also single tests were conducted at 20 and 200 psi as indicated on Figure 32. The resulting data appear to be in good agreement with the linear fit, i.e., the 20-psi data point falls directly upon the linear fit, and the 200-psi data point slightly above. Although there is some discrepancy between the measured and predicted values of V_f, the data spread in Figure 32 is small enough to conclude that the stem loading function (paragraph 8) used in the tree height prediction model properly represents the physical phenomena.

* Data from last two columns of Table 12.

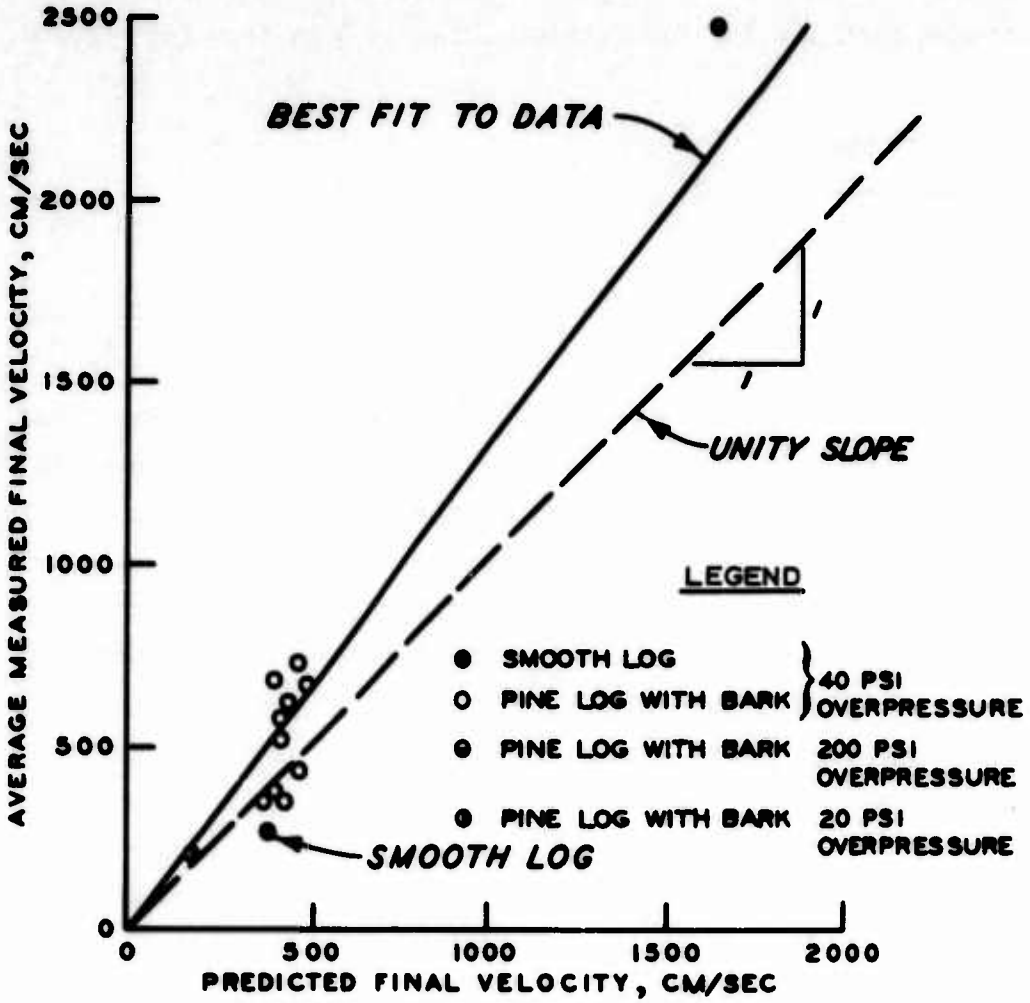

Figure 32. Comparison of predicted and measured final velocities for logs

PART V: CONCLUSIONS AND RECOMMENDATIONS

Conclusions

93. The following conclusions are based on the measurement techniques developed for the test program and the resulting data:

a. Reliable equipment and data reduction techniques were developed to evaluate the impulse loading experienced by a tree stem (flying log) being acted upon by a shock front.

b. The reduced data from the test series indicate that the loading function used in the partial differential equation describing tree stem motion under the influence of a shock front[1] is valid for the data presented.

Recommendations

94. Based on the findings of this study, it is recommended that:

a. Comprehensive tests be initiated to acquire additional impulse data for tree stem loading for OP's greater than and less than 40 psi.

b. Additional tests be conducted to determine the relative influence of the drag coefficient on the theoretical loading function as compared with other parameters.

REFERENCES

1. Benn, B. O. et al., "Evaluation of Construction Munitions for Clearing Helicopter Landing Zones in Forested Areas, Project Combat Trap; Effects of Bomb Blast on Trees ," Technical Report M-69-3, Report 1, Aug 1969, U. S. Army Engineer Waterways Experiment Station, Vicksburg, Miss.

2. Sadwin, L. D. and Swisdak, M. M. Jr., "Blast Characteristics of 20- and 100-ton Hemispherical AN/FO Charges, NOL Data Report," NOL TR 70-32, 17 Mar 1970, Naval Ordnance Laboratory, White Oak, Md.

3. Kingery, C., personal communication, Aug 1969, U. S. Army Ballistics Research Laboratory, Aberdeen Proving Ground, Md.

4. Needham, C. E., et al., "Theoretical Calculations of the Detonation of a 1,000-lb Sphere of TNT at 15 Feet Above Ground Level," Technical Report No. AFWL-TR-66-128, Oct 1966, Air Force Weapons Laboratory, Air Force Systems Command, Kirtland Air Force Base, N. Mex.

5. U. S. Naval Ordnance Laboratory, "Explosive Effects Data Sheets," NAVORD Report Z986, Jun 1955, White Oak, Md.

6. Office, Chief of Engineers, Department of the Army, "The Effects of Nuclear Weapons," Pamphlet No. 39-3, Apr 1962 (revised and reprinted Feb 1964), Washington, D. C.

7. Ethridge, N. H., "A Procedure for Smoothing Pressure-Time Data From H. E. and Nuclear Explosions," BRL Memorandum Report 1691, Sep 1965, Ballistics Research Laboratory, Aberdeen Proving Ground, Md.

8. Richtmyer, R. D. and Marton, K. W., Difference Methods for Initial-Value Problems, Interscience Publishers, New York, 1975.

Table 1

Equipment Used in Test Shots

Equipment	Shot BB00- 1	2	3	4	5	6	7
Noninstrumented logs	x	x					
Instrumented logs			(See Table 2)				
Explosive container	c	c	c	s	s	s	s
Recorders	x	x	x	x	x	x	x
Overpressure (OP) gages			(See Table 3)				
Time-of-arrival (TOA) gages			(See Table 4)				
Questar telescope	x	x	x	x	x	x	x
Earth-movement canister	x	x					
Accelerometers			(See Table 2)				
Velocity gages			(See Table 2)				
Displacement-time gages			(See Table 2)				
Cameras							
Milliken	x	x			x	x	x
Kodak	x			x			
Nova		x			x	x	x
Fairchild			x	x	x	x	x
Fastex			x	x			
Image distortion backboards				x	x	x	x

Note: x = apparatus used; c = cubical; and s = spherical.

Table 2

Instrumented Logs Used in Test Shots

Test Shot	Log	Log Data				Location		Accelerometers Mounted			Velocity Gages Mounted			Displacement-Time Gages†					
														A		B		C	
		Mass* g	Length cm	Diameter cm	Surface	Azimuth** deg	Distance from Ground Zero m	Left End	Center	Right End	Left End	Center	Right End	Left End	Right End	Left End	Right End	Left End	Right End
BB001	1	9,054	111.8	10	Rough	51	8.8							x	x				
	2	37,277		20		360								x	x				
BB002	1	9,520		10		51								x	x				
	2	35,455		20		360								x	x				
BB003	1	31,752		20		45		x		x	x		x						
	2	30,845		20		360			x			x		x	x	x	x		
	3	33,565		20		315			x		x	x						x	x
BB004	1	30,977		20		45		x		x	x		x						
	2	28,367		20		360			x			x				x	x		
	3	33,246		20		315			x		x	x						x	x
	4	36,083		20	Smooth	93				x									
BB005	1	32,590		20	Rough	338												x	x
	2	38,206		20		292	12.2											x	x
BB006	1	9,535		10		23	4.4											x	x
BB007	1	9,455		10		30	2.2											x	x

Note: x = instrumentation used.

* Log mass including mounted instrumentation.

** Azimuth relative to point in center of large concrete block which was base of wire-breaker displacement-time stand used in test shots BB001 and BB002. Origin of coordinate system at ground zero.

† A = wire-breaker (see text).
B = magnetic head mounted in concrete stand (see text).
C = magnetic head mounted in 6.3-cm-diam galvanized pipe (see text).

Table 3

Overpressure Gages Used in Test Shots

Test Shot	Overpressure Gage Designation	Azimuth* deg	Distance from Ground Zero m	Height of Gage Above Reference Plane** m
1	1	90	8.8	-0.74
	2	180		
	3	270		
	4	23		0.76
2	1	93	5.49	-0.94
	2	183	5.49	
	3	273	8.8	
	4	23	8.8	0.56
3	1	93	5.49	-0.60
	2	183		-0.60
	3	273		0.0
4	1	138		
	2	183		
	3	273		
5	1	108		-0.60
	2	293		
	3	207	8.8	
	4	344		0.0
	5	331		
	6	303	12.2	
6	1	108	5.49	
	2	292	5.49	
	3	207	8.8	
7	1	108	5.65	
	2	292	6.19	
	3	207	10.7	

* Azimuth relative to point in center of large concrete block which was base of wire-breaker displacement-time stand used in test shots BB001 and BB002. Origin of coordinate system at ground zero.

** The reference plane is the horizontal plane which includes the point source of the explosion (72 cm above original ground surface). Positive values indicate height above the plane and negative below the plane. This plane was the same for each test.

Table 4

Time-of-Arrival Gages Used in Test Shots

Test Shot	Time-of-Arrival Gage Designation	Azimuth* deg	Distance from Ground Zero m	Height of Gage Above Reference Plane** m
1	1	180	8.80	0.0
	2		10.80	
	3		12.30	
	4		13.80	
	5		10.80	2.37
	6		12.30	
	7		13.80	
	8	270	8.80	0.0
	9	0	8.80	
	10	90	8.80	
2	1	180	1.65	
	2		4.60	
	3		6.60	
	4		8.00	
	5		8.80	
	6		9.22	
	7		10.45	
	8		11.61	
	9		12.65	
	10		13.65	
	11		14.56	
	12		15.48	
	13		16.40	
	14		17.31	
	15		18.18	
	16		19.06	
	17		19.93	
	18		20.78	
	19		21.64	
	20		22.48	
	21		8.00	1.0
	22		8.80	
	23		9.22	
	24		10.45	
	25		11.61	
	26		12.65	
	27		13.65	
	28		14.56	
	29		15.48	
	30		16.40	
	31	90	1.65	0.0
	32		4.60	
	33		6.60	
	34		8.00	
	35		8.80	
	36		9.22	
	37		10.45	
	38		11.61	
	39		12.65	
	40		13.65	
2	41	90	14.56	0.0
	42		15.48	
	43		16.40	
	44		17.31	
	45		18.18	
	46		19.06	
	47		19.93	
	48		20.78	
	49		21.64	
	50		22.48	
	51	270	8.80	
	52	270	22.48	
	53	0	8.80	
	54		22.48	
5	2	203	8.80	
	3	247		
	4	292		
	5	342		
	10	158		
	11			1.46
	12		6.51	0.0
	13		8.00	
	14		8.80	
	15		9.22	
	16		10.45	
	17		11.61	
	18		12.65	
	19		13.65	
	20		14.56	
	21		15.48	
	22		16.40	
	23		17.31	
	24		18.18	
	25		19.06	
	26		19.93	
	27		20.78	
	28		21.64	
	29		22.48	
	40	68	1.46	
	41		4.46	
	42		6.51	
	43		8.01	-66.5
	44		8.80	0.0
	45		9.22	0.0
	46		10.45	-66.5
	47		11.61	0.0
	48		12.65	0.0
	49		13.65	-66.5

* Azimuth relative to point in center of large concrete block which was base of wire-breaker displacement-time stand used in test shots BB001 and BB002. Origin of coordinate system at ground zero.

** The reference plane is the horizontal plane which includes the point source of the explosion (72 cm above original ground surface). Positive values indicate height above the plane and negative below the plane. This plane was the same for each test.

Table 5

Meteorological Data For Shots BB001 through BB007

Test Shot	Temperature °C	Barometric Pressure, psi
BB001	16.7	14.8
BB002	29.4	14.5
BB003	32.8	14.7
BB004	30.0	14.7
BB005	34.7	14.6
BB006	30.6	14.7
BB007	35.4	14.7

Table 6

Data from Time-of-Arrival (TOA) Gages

Test Shot	TOA Gage Designation	Azimuth deg*	Distance from Ground Zero m	Height of Gage Above Reference Plane** m	Arrival Time msec
BB001	9	0	8.8	0.0	6.1
	10	90	8.8		6.2
	1	180	8.8		6.2
	8	270	8.8		6.0
	2	180	10.8		8.6
	5		10.8	2.37	10.2
	3		12.3	0.0	12.1
	6		12.3	2.37	14.0
	4		13.8	0.0	15.0
	7		13.8	2.37	16.8
BB002	53	0	8.8	0.0	6.7
	51	270	8.8	0.0	6.7
	24	180	10.45	1.00	11.4
	25	180	11.61	1.00	13.1
	26	180	12.65	1.00	15.2
	27	180	13.65	1.00	17.4
	41	90	14.56	0.0	17.2
	11	180	14.56	0.0	17.7
	28	180	14.56	1.00	19.0
	42	90	15.48	0.0	19.3
	12	180	15.48	0.0	19.1
	29	180	15.48	1.00	21.5
	43	90	16.40	0.0	21.3
	13	180	16.40	0.0	22.3
	30	180	16.40	1.00	23.2
	44	90	17.31	0.0	24.2
	14	180	17.31		24.0
	45	90	18.18		26.0
	15	180	18.18		25.8
	46	90	19.06		28.3
	16	180	19.06		29.0
	47	90	19.93		30.3
	17	180	19.93		31.0
	48	90	20.78		32.3
	18	180	20.78		32.2
	49	90	21.64		34.6
	19	180	21.64		34.3
	50	90	22.48		36.3
	20	180	22.48		36.2
	52	270	22.48		36.3
BB005	14	158	8.8		6.8
	15		9.22		7.4
	16		10.45		9.5
	17		11.61		11.7
	18		12.65		13.6
	19		13.65		15.4
	20		14.56		18.0
	21		15.48		19.2
	22		16.40		22.3
	23		17.31		23.2
	24		18.18		26.4
	25		19.06		27.3
	26		19.93		30.2
	27		20.78		31.4
	28		21.64		35.1
	29		22.48		36.7

* Azimuth relative to point in center of large concrete block which was base of wire-breaker displacement-time stand used in test shots BB001 and BB002. Origin of coordinate system at ground zero.

** The reference plane is the horizontal plane which includes the point source of the explosion (72 cm above original ground surface). Positive values indicate height above the plane. This plane was the same for each test.

Table 7

Data from Overpressure (OP) Gages

Test Shot	OP Gage Designation	Azimuth deg*	Distance from Ground Zero m	Height of Gage Above or Below Reference Plane** m	Activation Time of Gage msec	Peak Over-pressure psi
BB001	4	23	8.8	0.76	7.0	ND†
	1	90	8.8	-0.74	5.7	
	2	180	8.8	-0.74	6.0	
	3	270	8.8	-0.74	6.0	
BB002	1	93	5.49	-0.94	2.5	
	2	183	5.49	-0.94	2.5	
	3	23	8.8	0.56	6.6	
BB003	1	93	5.49	-0.60	2.9	129
	2	183		-0.60	2.4	139
	3	273		0.0	2.8	124
BB004	1	138		0.0	2.7	128
	2	183		0.0	2.8	142
	3	273		0.0	2.8	126
BB005	1	108		-0.60	2.7	122
	2	293		-0.60	2.7	127
	3	207	8.8	-0.60	6.5	46
	5	331	8.8	0.0	6.4	37
	4	344	8.8		6.4	34
	6	303	12.2		12.1	16
BB006	1	108	5.49		3.0	133
	2	292	5.49		2.9	140
	3	207	8.8		6.4	52
BB007	1	108	5.65		2.7	ND
	3	207	10.7		9.7	32
	2	292	6.19		3.3	100

* Azimuth relative to point in center of large concrete block which was base of wire-breaker displacement-time stand used in test shots BB001 and BB002. Origin of coordinate system at ground zero.

** The reference plane is the horizontal plane which includes the point source of the explosion (72 cm above original ground surface). Positive values indicate height above the plane and negative below the plane. This plane was the same for each test.

† No data.

Table 8

Time-of-Arrival (TOA) Data Used to Evaluate Shock-Front Symmetry

Test Shot	TOA Gage Designation	Azimuth deg*	Distance From Ground Zero m	Arrival Time msec
BB001	9	0	8.8	6.1
	10	90	↓	6.2
	1	180	↓	6.2
	8	270	↓	6.0
BB002	53	0	↓	6.7
	51	270	↓	6.7
	41	93	14.56	17.2
	11	183	14.56	17.7
	42	90	15.48	19.3
	12	180	15.48	19.1
	43	90	16.40	21.3
	13	180	16.40	22.3
	44	90	17.31	24.2
	14	180	17.31	24.0
	45	90	18.18	26.0
	15	180	18.18	25.8
	46	90	19.06	28.3
	16	180	19.06	29.0
	47	90	19.93	30.3
	17	180	19.93	31.0
	48	90	20.78	32.3
	18	180	20.78	32.2
	49	90	21.64	34.6
	19	180	21.64	34.3
	50	90	22.48	36.3
	20	180	22.48	36.2

* Azimuth relative to point in center of large concrete block which was base of wire-breaker displacement-time stand used in test shots BB001 and BB002. Origin of coordinate system at ground zero.

Table 9

Time-of-Arrival Data Used to Examine Inclination of Shock Front

Test Shot	TOA Gage Designation		Activation Time of Gage, msec	
	Lower	Upper	Lower	Upper
BB001	2	5	8.6	10.2
	3	6	12.1	14.0
	4	7	15.0	16.8
BB002	11	28	17.7	19.0
	12	29	19.1	21.5
	13	30	22.3	23.2

Table 10

Comparison of WES and BRL Time-of-Arrival Data

Test Shot	Distance from Ground Zero, m	Shock-Front Time of Arrival, msec	
		Measured by WES*	Predicted from BRL Data
BB001	8.8	6.2	7.3
	8.8	6.0	7.3
	8.8	6.1	7.3
	8.8	6.2	7.3
	10.8	8.6	10.6
	11.05	10.2	10.9
	12.3	12.1	13.5
	12.52	14.0	13.8
	13.8	15.0	16.5
	14.00	16.8	16.7
BB002	8.8	6.7	7.3
	8.8	6.7	7.3
	10.49	11.4	10.3
	11.65	13.1	12.3
	12.68	15.2	14.2
	13.68	17.4	16.2
	14.56	17.2	18.0
	14.56	17.7	18.0
	14.57	19.0	18.1
	15.48	19.1	20.0
	15.48	19.3	20.0
	15.51	21.5	20.0
	16.40	21.3	22.4
	16.40	22.3	22.4
	16.43	23.2	22.4
	17.31	24.0	24.4
	17.31	24.2	24.4
	18.18	25.8	26.5
	18.18	26.0	26.5
	19.06	28.3	29.0
	19.06	29.0	29.0
	19.93	30.3	30.0
	19.93	31.0	30.0
	20.78	32.2	32.8
	20.78	32.3	32.8
	21.64	34.3	35.0
	21.64	34.6	35.0
	22.48	36.2	37.5
	22.48	36.3	37.5
	22.48	36.3	37.5
BB005	8.80	6.8	7.3
	9.22	7.4	8.0
	10.45	9.5	10.0
	11.51	11.7	12.0
	12.65	13.6	14.0
	13.65	15.4	16.0
	14.65	18.0	18.0
	15.48	19.2	20.0
	16.40	22.3	22.4
	17.31	23.2	24.4
	18.18	26.4	26.5
	19.06	27.3	29.0
	19.93	30.2	30.0
	20.78	31.4	32.8
	21.64	35.1	35.0
	22.48	36.7	37.5

* From Table 6.

Table 11

WES and BRL Peak Overpressure Data

Test Shot	Distance from Ground Zero, m	Peak Overpressure, psi	
		Measured by WES*	Predicted from BRL Data
BB003	5.49	124	125
	5.52	129	123
	5.49	139	125
BB004	5.49	126	125
	5.49	128	125
	5.49	142	125
BB005	5.52	122	123
	5.52	127	123
	8.80	34	43
	8.80	37	43
	8.82	46	43
	12.20	16	21
BB006	5.49	133	125
	5.49	140	125
	8.80	52	43
BB007	6.19	100	97
	10.7	32	28

* From Table 7.

Table 12

Momentum Transfer Data

Test Shot	Log	Log Data: Mass g*	Length cm	Diameter cm	Distance from Ground Zero m	Gage Type**	Measured Horizontal Velocity, cm/sec, Gage Position on Log: Left	Center	Right	Representative Horizontal Velocity of the Center of Mass of the Log, cm/sec	Calculated Horizontal Velocity, cm/sec
BB001	1	9,054	111.8	10	8.8	DSPMT			663	663	482
	2	37,277	111.8	20	8.8	DSPMT			351	351	358
BB002	1	9,520	111.8	10	8.8	DSPMT	770		690	730	458
BB003	1	31,752	111.8	20	8.8	ACC	440			583	421
						VEL	470		710		
	2	30,845	111.8	20	8.8	ACC		510		520	419
						VEL		530			
	3	33,565	111.8	20	8.8	ACC		340		400	398
						VEL	350	360			
						DSPMT			550		
BB004	1	30,977	111.8	20	8.8	ACC	740		220	618	431
						VEL	1030		480		
	2	28,367	111.8	20	8.8	ACC		430		440	471
						VEL		480			
						DSPMT	410		410		
	3	33,246	111.8	20	8.8	ACC		560		680	401
						VEL	350	770			
						DSPMT			1070		
	4†	36,083	111.8	20	8.8	ACC			270	270	370
BB005	1	32,590	111.8	20	8.8	DSPMT	370		340	355	416
	2	38,206	111.8	20	12.2	DSPMT	180		230	205	177
BB006	1	9,535	111.8	10	4.4	DSPMT	2390		2570	2480	1653

* Log mass including mounted instrumentation.

** ACC = acceleration gage; VEL = velocity gage; DSPMT = displacement-time gage.

† Smooth log (turned down on lathe to remove log bark).

Table 13

Comparison of Horizontal Velocities from Left and Right Gage Positions Measured with Displacement-Time Gages

Log Mass g	Distance of Log from GZ m	Final Velocity m/sec	
		Left	Right
9,535	4.4	23.9	25.7
9,520	8.8	7.7	6.9
28,367	8.8	4.1	4.1
32,590	8.8	3.7	3.4
38,206	12.2	1.8	2.3

APPENDIX A: TREE STEM FAILURE

1. This appendix describes the development of a failure criterion for a tree stem under dynamic loading by a shock front. The failure criterion is based on the mechanical properties of the tree stem and does not specify the height on the stem at which failure occurs. Estimation of this height requires the solution of a fourth-order partial differential equation (PDE) that describes the deformation of the stem under loading; the solution of this PDE using the finite difference method is demonstrated. The solution of the PDE requires a theoretical loading function that simulates the effect of the shock front on the stem; the loading function is derived.

Failure Criterion

2. The failure curvature of a tree stem under dynamic loading can be derived by treating the tree as a right-circular cylindrical wood beam. The bending moment at any cross section of a beam is expressed in equation form as

$$M_b = \frac{\sigma \times I}{r} \tag{A1}$$

where

M_b = static bending moment

σ = maximum stress occurring at a section

$I = \pi r^4/4$ = moment of inertia of circular cross section of a beam with respect to the neutral axis

r = radius of beam (distance from the neutral axis to the outermost fiber)

Substituting the modulus of rupture, S, for the maximum stress in Equation A1 yields

$$M_c = \frac{S \times I}{r} \tag{A2}$$

where M_c = bending moment required for failure. A mathematical description of stem curvature in response to impulse loading is a prerequisite to the analysis of stem failure. The bending moment at any height above the ground for any time is described by

$$EI\left[\frac{\partial^2 y(x,t)}{\partial x^2}\right] = M_b(x,t) \qquad \text{(A3)}$$

where

E = Young's modulus parallel to longitudinal axis of beam

$\partial^2 y/\partial x^2$ = geometric curvature of beam

$y(x,t)$ = deflection perpendicular to the longitudinal axis of the beam

x = distance along longitudinal axis of beam from base of beam (origin of coordinate system)

t = time after initial application of driving force (shock front)

By introducing Equation A2 into Equation A3 and rearranging terms, the equation for beam (stem) failure curvature K_c is

$$K_c = \frac{S}{Er} \qquad \text{(A4)}$$

Whenever the value for the term $\partial^2 y/\partial x^2 > K_c$, stem failure will occur for given values of S, E, and r. Equation A4 is time independent and does not specify a unique height on the stem at which failure occurs; also Equation A4 is not a function of the dynamic loading. These restrictions should be removed so that Equation A4 can be used to predict stem-remnant height after detonation of a munition.

Partial Differential Equation

3. The geometric curvature of a beam can be explicitly related to the dynamic loading of the beam for unique values of x and t by consideration of the dynamic equilibrium equation of the beam:

$$\frac{\partial mv(x,t)}{\partial t} + \frac{\partial^2}{\partial x^2}\left\{EI(x)\left[\frac{\partial^2 y(x,t)}{\partial x^2}\right]\right\} = F(x,t) \qquad \text{(A5)}$$

where

$m = \rho A$ = mass per unit length of cylinder

ρ = density of the wood beam

A = cross-sectional area of the beam

$\partial y(x,t)/\partial t$ = velocity of stem perpendicular to the longitudinal axis of the beam

$F(x,t)$ = function that characterizes the dynamic loading of the stem by the shock front. $F(x,t)$ has units of force per unit length

The first term of Equation A5 represents the inertial force per unit length required to accelerate an elemental mass (i.e. the mass associated with a unit length) in a horizontal direction (y) for a given unit time. The second term is the second derivative of the bending moment (Equation A3). This term represents the internal load intensity for a given beam cross section. In the static condition, the vector resultant of all loads is zero, i.e. $\Sigma F = 0$. The system is in equilibrium because there are no unbalanced forces. Any excess in the external load over the internal load must be balanced by force that produces acceleration and bending of the beam. By taking the indicated partial derivatives in Equation A5,

$$\rho A\left[\frac{\partial v(x,t)}{\partial t}\right] + v(x,t)\left[\frac{d(\rho A)}{dt}\right] + \left\{\frac{d^2[EI(x)]}{dx^2}\right\}\left[\frac{\partial^2 y(x,t)}{\partial x^2}\right]$$

$$+ 2\left\{\frac{d[EI(x)]}{dx}\right\}\left[\frac{\partial^3 y(x,t)}{\partial x^3}\right] + EI(x)\left[\frac{\partial^4 y(x,t)}{\partial x^4}\right] = F(x,t)$$

If ρ and E are assumed to be constant and the cross-sectional area of the stem is πr^2 , where r is a function of x only, then the following working form of the PDE is generated:

$$\rho\pi r^2\left[\frac{\partial v(x,t)}{\partial t}\right] + \left[E\,\frac{d^2 I(x)}{dx^2}\right]\left[\frac{\partial^2 y(x,t)}{\partial x^2}\right] + \left[2E\,\frac{dI(x)}{dx}\right]\left[\frac{\partial^3 y(x,t)}{\partial x^3}\right]$$

$$+ EI(x)\left[\frac{\partial^4 y(x,t)}{\partial x^4}\right] = F(x,t) \qquad \text{(A6)}$$

By representing the tree stem as a right-circular cylindrical beam, the moment of inertia is constant for all x. Therefore, the second and third terms of Equation A6 go to zero, and the equation becomes

$$\rho w r^2 \left[\frac{\partial v(x,t)}{\partial t}\right] + EI\left[\frac{\partial^4 y(x,t)}{\partial x^4}\right] = F(x,t) \qquad \text{(A7)}$$

Loading Function

4. The solution of Equation A7 requires a mathematical expression for $F(x,t)$ that describes the loading of the beam by the shock front. $F(x,t)$, hereafter referred to as the loading function, can be established in terms of the total effective pressure impulse (J_T) as follows:

$$J_T = \int_0^{T_p} P(t)\, dt$$

where

T_p = positive pulse duration

$P(t)$ = total effective pressure incident upon the beam

By assuming that $P(t)$ rises to a maximum value instantaneously, the impulse is the area of simple triangle (Figure A1). Therefore,

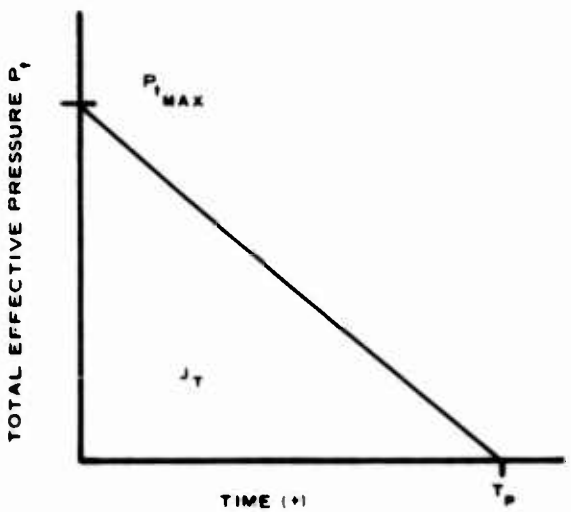

Figure A1. Triangular assumption used to calculate the total effective pressure impulse (J_T)

$$J_T = \frac{P_{T_{max}} T_p}{2}$$

Solving for $P_{T_{max}}$:

$$P_{T_{max}} = \frac{2J_T}{T_p}$$

Multiplying this equation by the diameter of the stem (2r) produces an expression with terms of force per unit length, which are the correct units for Equation A7. Then

$$F(x,t)_{T_{max}} = (2r)\left(P_{T_{max}}\right) = \frac{4rJ_T}{T_p} \qquad (A8)$$

The value computed for Equation A8 is the maximum force per unit length experienced by the stem during the positive pulse duration (T_p). $F(x,t)_{T_{max}}$ is a constant at a given point on the stem for the positive pulse duration. It is, therefore, necessary to construct a loading function that includes $F(x,t)_{T_{max}}$, but is a function of time.

5. The loading function $F(x,t)$ was constructed in two components. The first component describes the effect of the shock front on the stem from the time the shock front first comes in contact with the stem until the amplitude of the shock front pulse reaches a maximum value $F(x,t)_{T_{max}}$. This time interval is defined as the rise time (T_r). The second component describes the effect of the shock front on the stem from the time when the amplitude of the shock-front pulse is a maximum until the time when the pulse first decays to zero. This time interval is defined as the decay time. The time period from initial contact of the stem by the shock front until the shock front passes its peak amplitude and first returns to zero is defined as the positive pulse duration (T_p). The above requirements can be expressed mathematically as:

$$\left.\begin{array}{ll} \text{At } t = 0 & F(x,t) = 0 \\ \text{At } t = T_r & F(x,t) = F(x,t)_{T_{max}} \\ \text{At } t = T_p & F(x,t) = 0 \end{array}\right\} \qquad \text{(A9)}$$

6. It is necessary to derive appropriate scale factors which, when multiplied by $F(x,t)_{T_{max}}$, will satisfy the requirements of Equations A9. The scale factors must characterize the physical phenomena of the rise and decay components of the loading function. The loading function can then be expressed mathematically as:

$$F(x,t)_{rise} = F(x,t)_{T_{max}} SF_R$$

$$F(x,t)_{decay} = F(x,t)_{T_{max}} SF_D$$

where

SF_R = rise scale factor

SF_D = decay scale factor

7. To satisfy Equations A9, the following restrictions must be placed on the scale factors:

$$\left.\begin{array}{ll} \text{At } t = 0 & SF_R = 0 \\ \text{At } t = T_r & SF_R = SF_D = 1 \\ \text{At } t = T_p & SF_D = 0 \end{array}\right\} \qquad \text{(A10)}$$

The value of SF_R was hypothesized to increase as the stem loading area increased. SF_D was assumed to decrease linearly.

8. The stem loading area is assumed to be a plane perpendicular to the horizontal component of the total effective pressure impulse and confined to the chord of the stem surface and length differential (dx) of the stem (Figure A2). The rise time T_r is assumed to be the ratio of the stem radius to the shock-front velocity. The time required to

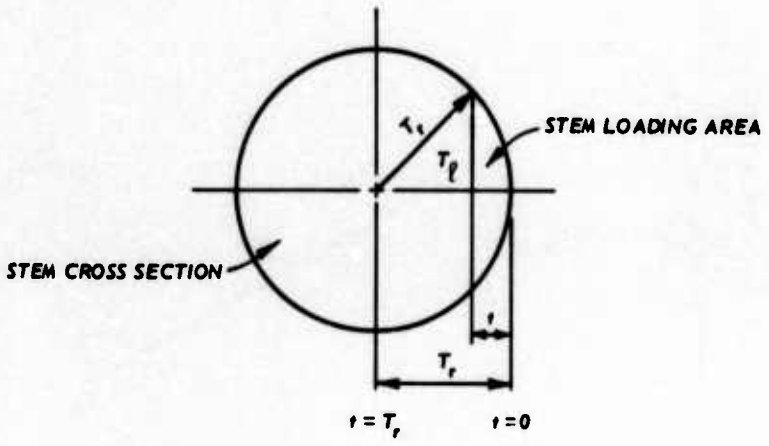

Figure A2. Calculation of time required to load a given differential stem area

load a given area, T_ℓ , is calculated as follows:

$$T_\ell = \sqrt{T_r^2 - (T_r - t)^2}$$

where

T_ℓ = time required to load differential stem area

T_r = rise time of positive pulse

Simplifying,

$$T_\ell = T_r \sqrt{1 - \left(1 - \frac{t}{T_r}\right)^2}$$

The dimensionless square root is equivalent to SF_R because it obeys the required conditions of Equation A10 and increases as the loading area increases. Therefore,

$$F(x,t)_{rise} = F_{T_{max}} \left[1 - \left(1 - \frac{t}{T_r}\right)^2\right]^{1/2} \qquad \text{(A11)}$$

9. The decay component of the loading function can be derived from the equation of the line from $\left[T_r\ ,\ F(x,t)_{T_{max}}\right]$ to $(T_p\ ,\ 0)$ (see Figure A3). The slope of the line is

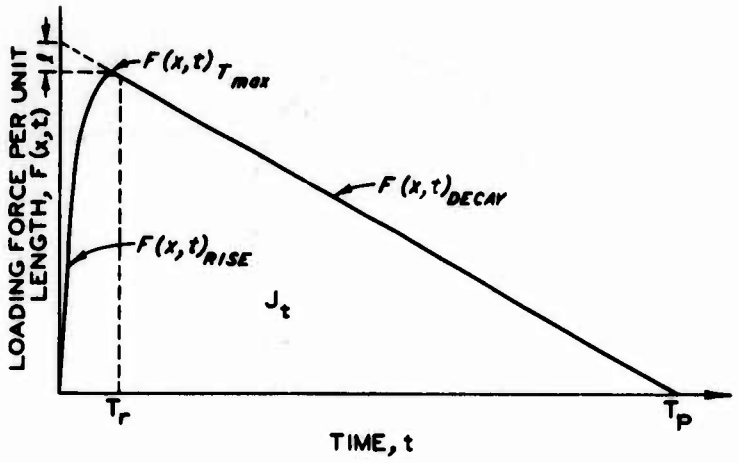

Figure A3. Graphic representation of loading function

$$m = - \frac{F_{T_{max}}}{T_p - T_r}$$

The intercept is

$$B = F_{T_{max}} + \ell = F_{T_{max}} + m \times T_r$$

Therefore,

$$F(x,t)_{decay} = mt + B = - \left(\frac{F_{T_{max}}}{T_p - T_r} \right) t + \left[F_{T_{max}} \left(\frac{F_{T_{max}}}{T_p - T_r} \right) T_r \right]$$

$$= F_{T_{max}} \left(1 - \frac{t - T_r}{T_p - T_r} \right) \quad \text{for} \quad T_r < t < T_p \qquad \text{(A12)}$$

10. Equations A11 and A12 satisfy the requirements in paragraphs 5 and 7, above, but the derivatives of the functions are discontinuous at $t = T_r$, i.e.

$$\frac{\partial F_{rise}}{\partial t} \neq \frac{F_{decay}}{\partial t} \qquad \text{(A13)}$$

Physically, this means that at $t = T_r$ the rise and decay functions are not changing at the same rate with respect to time. This problem was rectified by multiplying the rise component of the loading function by the decay scale factor (SF_D). The rise component of the loading function then becomes

$$F(x,t)_{rise} = \frac{4rJ_T}{T_p}\left(1 - \frac{t - T_r}{T_p - T_r}\right)\left[1 - \left(1 - \frac{t}{T_r}\right)^2\right]^{1/2}$$

$$\text{for} \quad 0 < t < T_r \qquad \text{(A14)}$$

Equation A14 then satisfies the equality (Equation A13). SF_D is very close to unity between $t = 0$ and $t = T_r$; therefore, it is numerically insignificant in the solution, but it does cause the peak value of loading to occur slightly before $t = T_r$ (Figure A3).

11. Two further refinements were made. First, the total effective pressure impulse discussed thus far has assumed radial symmetry with respect to the source of the shock front (center of explosion). At heights on the stem different from the height of the center of the explosion, error will be introduced into the computations if the radial value of J_T is used; therefore, to eliminate this error, the horizontal component of J_T must be substituted into the loading function, i.e.

$$J_{T_{horizontal}} = J_T \cos \phi$$

where ϕ is the angle between the horizontal and the point of interest on the tree. Second, the value of J_T is not constant for all points on the stem because the shock front decays as the reciprocal of the square of the propagation distance; and since the distances from the center of the explosion to any two points on the stem are different, J_T must also be different. Therefore,

$$J_{TL} = J_{TR}\left(\frac{R}{L}\right)^2$$

where

J_{TL} = effective total pressure impulse at any point on the stem

J_{TR} = effective total pressure impulse at a height on the stem equal to the height of the center of the explosion (EC)

R = horizontal distance from EC to tree stem

L = radial distance from EC to point of interest on tree stem

These two modifications are shown in detail on pages 16 and 17 of Reference 1.*

12. The resulting loading function is

$$F(x,t)_{rise} = \frac{4rJ_{TR}R^2 \cos\phi}{T_p L^2}\left(1 - \frac{t - T_r}{T_p - T_r}\right)\left[1 - \left(1 - \frac{t}{T_r}\right)^2\right]^{1/2} \quad \text{for} \quad 0 < t < T_r$$

$$F(x,t)_{decay} = \frac{4rJ_{TR}R^2 \cos\phi}{T_p L^2}\left(1 - \frac{t - T_r}{T_p - T_r}\right) \quad \text{for} \quad T_r < t < T_p$$

A value for J_{TR} was calculated by the following equation:

$$J_{TR} = JC_d + P_r\left(\frac{2r}{U}\right)$$

where

J = dynamic pressure impulse

C_d = drag coefficient of stem

P_r = reflected pressure

U = shock-front velocity

All values apply to the point on the stem that equals the height of the EC. JC_d results from the air drag on the stem within the shock front. The second term in the equation is due to the pressure differential between the side facing the incident shock front and the lee side of the tree stem. The term $2r/U$ is the shock-front transit time across the stem (see Reference 1, pages 25 and 26).

---

* References in this appendix are cited at the end of the main text.

Finite Difference Solution

13. The fourth-order differential equation describing the dynamic deformation of a right-circular cylindrical beam (Equation A7) is difficult to solve in closed form for an arbitrary function $F(x,t)$. Therefore, a numerical scheme was employed to obtain a solution of Equation A7. The derivatives were represented in finite difference form as follows:

$$\rho\pi r^2\left(\frac{Y_{i-1,j} - 2Y_{i,j} + Y_{i+1,j}}{\Delta t^2}\right)$$

$$+ \frac{E\pi r^4}{4}\left(\frac{Y_{i,j-2} - 4Y_{i,j-1} + 6Y_{i,j} - 4Y_{i,j+1} + Y_{i,j+2}}{\Delta H^4}\right) = F_{i,j} \qquad \text{(A15)}$$

where

$Y_{i,j}$ = horizontal displacement at time step i and nodal point j above the ground

i = time subscript

j = distance subscript

Δt = time increment

ΔH = distance increment along the beam

$F_{i,j}$ = loading function in terms of discrete values ($F(x,t)$ implies a continuous function)

Note that upper case Y's are used for the finite difference solution and lower case y's for differential representation.

Boundary Conditions

14. Associated with the solution of the fourth-order PDE are four boundary conditions related to the independent variable x and two related to the independent variable t (more properly an initial value problem). Consider the stem model as in Figure A4. The stem is free to rotate at the base, but not to translate. The following boundary conditions can be deduced from the diagram: (a) At $x = 0$, $y = 0$,

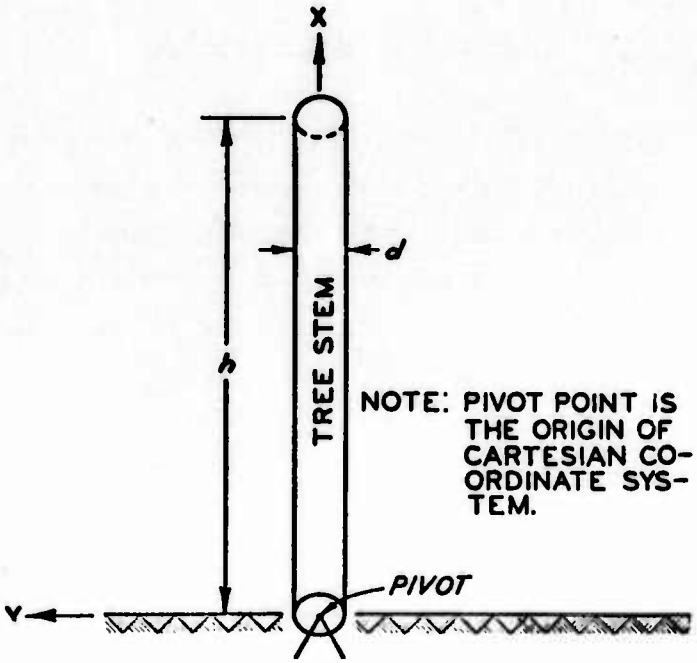

Figure A4. Stem model

(b) the bending moment at $x = 0$ (base of stem) is zero, (c) the bending moment at $x = L$ (top of stem) is zero, and (d) the shear at $x = L$ is zero. These can be expressed mathematically as

$$\text{At } x = 0 \text{ , } y(0,t) = 0 \text{ and } EI(x) \frac{\partial^2 y(0,t)}{\partial x^2} = 0$$

$$\text{At } x = L \text{ , } EI(x) \frac{\partial^2 y(L,t)}{\partial x^3} = 0 \qquad \text{(A16a)}$$

and

$$EI(x) \frac{\partial^3 y(L,t)}{\partial x^3} = 0 \qquad \text{(A16b)}$$

The statement (Equation A16b) is true because:

$$\frac{\partial}{\partial x}\left(EI \frac{\partial^2 y}{\partial x^2}\right) = \left(\frac{\partial EI}{\partial x}\right)\left(\frac{\partial^2 y}{\partial x^2}\right) + EI\left(\frac{\partial^3 y}{\partial x^3}\right)$$

But at $x = L$, $\partial^2 y/\partial x^2 = 0$. Therefore, expression A16b is valid. Applying finite difference notation to the boundary conditions:

At $x = 0$ (base of stem, i.e., $j = 2$)

$$Y_{i,j} = 0 \quad \text{and} \quad \frac{Y_{i,j-1} - 2Y_{i,j} + Y_{i,j+1}}{\Delta H^2} = 0$$

Therefore,

$$Y_{i,j-1} = -Y_{i,j+1}$$

At $x = L$ (top of stem, i.e., $j = n$, where n is the last node point)

$$\frac{Y_{i,j-1} - 2Y_{i,j} + Y_{i,j+1}}{\Delta H^2} = 0 \quad \text{and}$$

$$\frac{-Y_{i,j-2} + 2Y_{i,j-1} - 2Y_{i,j+1} + Y_{i,j+2}}{2\Delta H^3} = 0 \qquad \text{(A17)}$$

Then,

$$Y_{i,j+1} = 2Y_{i,j} - Y_{i,j-1}$$

and from Equation A17

$$Y_{i,j+2} = 4Y_{i,j} - 4Y_{i,j-1} + Y_{i,j-2}$$

15. The initial value problem relevant to time is solved by considering that the displacement and velocity at $t = 0$ are zero. These can be expressed mathematically as

$$Y(x,0) = 0 \quad \text{and} \quad Y(x,t) = 0 \quad \text{for} \quad t < 0$$

and

$$\frac{\partial Y(x,t)}{\partial t} = 0$$

Hence, at $t = 0$, i.e., $i = 1$, the initial conditions can be expressed in finite difference form by

$$Y_{i,j} = 0$$

$$Y_{i-1,j} = 0$$

and

$$\frac{-Y_{i-1,j} + Y_{i+1,j}}{2\Delta t} = 0$$

Therefore,

$$Y_{i+1,j} = Y_{i-1,j}$$

Sample Solution of Finite Difference Equation

16. The six boundary conditions, plus the finite difference form for the PDE, are sufficient to generate values for the deflection and its derivatives for all times greater than $t = 0$ at selected heights up the tree. The sequence of mathematical operations is to calculate the deflection at each of the node points for a given time, i.e., the j subscript is incremented from $j = 1$ to $j = n$ for a given value of i. Solving for the acceleration term from Equation A15:

$$\ddot{Y}_{i,j} \cong \frac{F_{i,j}}{\rho\pi r^2} - \frac{Er^2}{4\rho}\left(\frac{Y_{i,j-2} - 4Y_{i,j-1} + 6Y_i - 4Y_{i,j+1} + Y_{i,j+2}}{\Delta H^4}\right)$$

Also from finite difference notation:

$$\ddot{Y}_{i,j} = \frac{Y_{i-1,j} - 2Y_{i,j} + Y_{i+1,j}}{\Delta t^2}$$

Therefore,

$$Y_{i+1,j} = \ddot{Y}_{i,j}\Delta t^2 + 2Y_{i,j} - Y_{i-1,j}$$

Thus, the deflection in the next time increment can be generated. Consider the following graphic representation (Figure A5) of eight node points prior to the initial calculation. The initial deflections (at $t = 0$) are assumed to be zero, i.e., $Y_{i,j}$, where j varies from 3 to 10. From the boundary conditions $Y_{1,12}$, $Y_{1,11}$, and $Y_{1,1}$ are also zero. The deflections before time zero ($Y_{o,j}$) are also assumed to be zero. The time zero here specifically refers to the time at which the shock wave arrives at a node point on the stem and differs from the detonation time for the bomb by the amount of time required for the shock front to travel from ground zero (GZ) to the node point in question.

17. Since all the $Y_{i,j}$'s are zero for the initial calculations,

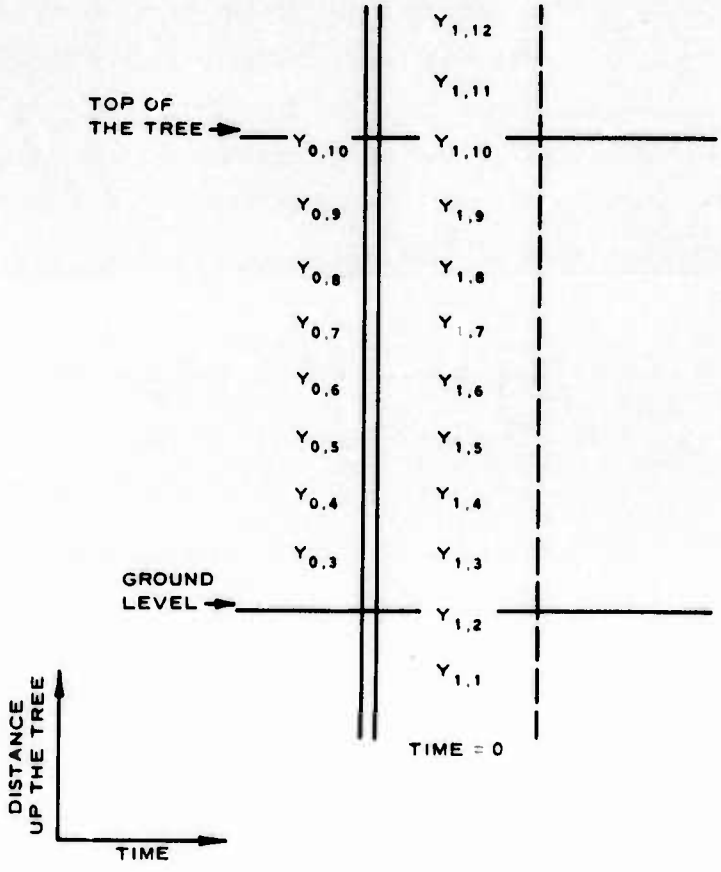

Figure A5. Graphic representation of initial data at $t = 0$. As discussed in the text, all $Y_{i,j}$ values are zero

$$\ddot{Y}_{i,j} \cong \frac{F_{i,j}}{\rho \pi r^2}$$

where $F_{i,j}$ is different for each node point. The difference in the driving function $F_{i,j}$ at each node point arises from the fact that the distance that the shock front must travel is different at each point, and the angle between the horizontal and incident front is different for each node point. The following calculation can now be made:

$$Y_{2,j} \cong \ddot{Y}_{1,j}\Delta t^2 = \frac{F_{1,j}\Delta t^2}{\rho \pi r^2} = BF_{2,j}$$

where $B = \Delta t^2/\rho \pi r^2$. The deflections for the first two time steps are shown in Figure A6. The data enclosed by ellipses represent the data necessary to obtain the deflection for $Y_{2,7}$. The five points in the vertical ellipse yield the acceleration; then using a backward difference, the actual deflection is calculated. The specific details of obtaining $Y_{2,7}$ are as follows:

$$\ddot{Y}_{1,7} = \frac{F_{1,7}}{\rho \pi r^2} - \frac{Er^2}{4\rho}\left(\frac{Y_{1,5} - 4Y_{1,6} + 6Y_{1,7} - 4Y_{1,8} + Y_{1,9}}{\Delta H^4}\right)$$

But

$$Y_{1,5} = Y_{1,6} = Y_{1,7} = Y_{1,8} = Y_{1,9} = 0$$

Therefore,

$$\ddot{Y}_{1,7} = \frac{F_{1,7}}{\rho \pi r^2}$$

Then

$$Y_{2,7} = \ddot{Y}_{1,7}\Delta t^2 + 2Y_{1,7} - Y_{0,7} = \frac{\Delta t^2 F_{1,7}}{\rho \pi r^2} + 2(0) - (0) = BF_{1,7}$$

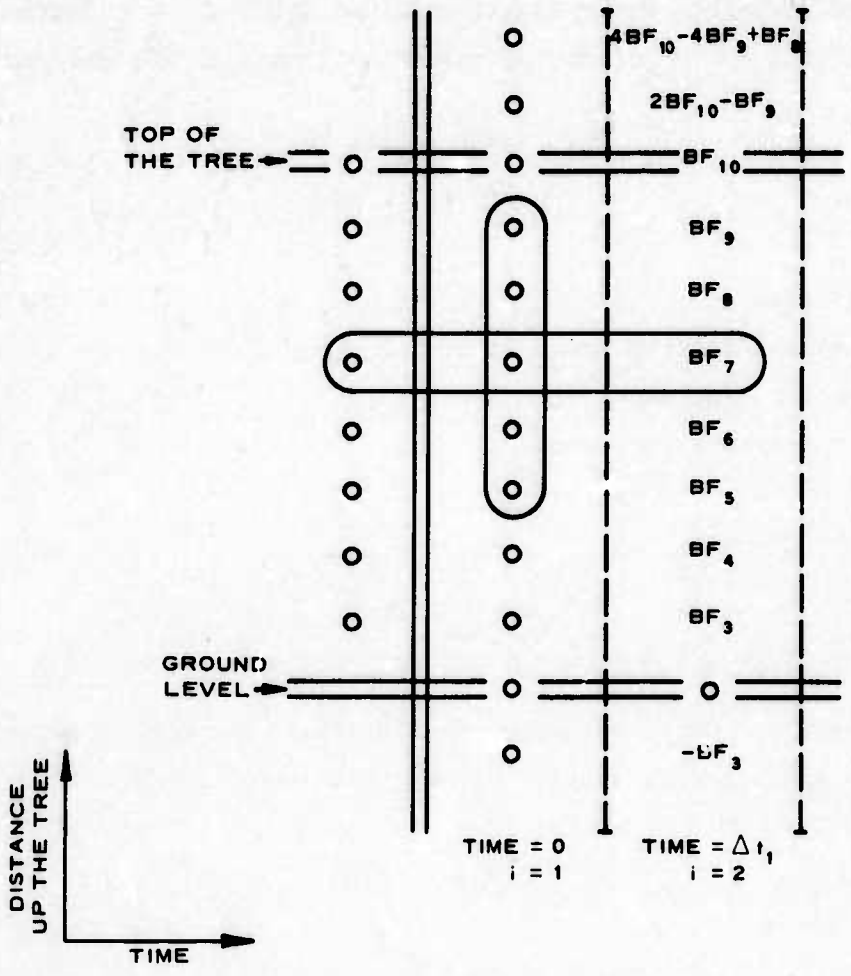

Figure A6. Calculations for displacements at $t = \Delta t_1$. Numbers enclosed in elliptical areas show data used to calculate $Y_{2,7}$

where $B = \Delta t^2/\rho\pi r^2$. The four derivatives of the deflection can then be calculated by using central differences. The second, third, and fourth derivatives correspond to the bending moment, shear, and load, respectively, provided the central difference is multiplied by the flexural rigidity (EI). The calculations continue in this manner until the limit of the time interval of interest is reached.

Stability of Finite Difference Equation

18. The stability of the finite difference equation for the

given selected differences can be examined using the von Neuman necessary condition for stability of thin elastic beams from Reference 8;

$$\frac{a\Delta t}{\Delta H^2} = 1/2$$

where

$a = EI/\mu$

μ = mass density per unit length

Δt = time increment

ΔH = distance increment

Then

$$a = \sqrt{\frac{E\frac{\pi r^4}{4}}{\rho \pi r^2}} = \sqrt{\frac{Er^2}{4\rho}}$$

For the reference case solution (see Reference 1) used to generate failure heights versus distance from ground zero (DGZ),

$$E = 1.2 \times 10^{11}$$

$$\rho = 0.8$$

Then,

$$\sqrt{\frac{(1.2 \times 10^{11})r^2}{(4)(0.8)}}\left(\frac{\Delta t}{\Delta H^2}\right) < 1/2$$

Therefore, the stability condition for this problem is

$$r\left(\frac{\Delta t}{\Delta H^2}\right) < 0.258 \times 10^{-5} \qquad \text{(A18)}$$

Output from the computer solution of Equation A15 was verified using Equation A18. Violation of Equation A18 yielded deflections that were meaningless.

APPENDIX B: NOMOGRAPHIC SOLUTION FOR PREDICTION OF STEM-REMNANT HEIGHT

1. This appendix describes the development of a nomographic solution for the prediction of tree stem-remnant height for wide variations in weapon yield and stem properties. This solution uses the stem failure criterion and the finite difference solution of the partial differential equation (PDE) describing stem motion developed in Appendix A.

2. The finite difference solution for the PDE is a lengthy iterative technique that is amenable to a computer solution in lieu of manual calculations. The resulting computer output yields the deflection of the stem and its derivatives at selected heights up the tree for a given time. The second derivative of the deflection is the curvature; hence, data for curvature times stem radius versus height on the stem at which the curvature occurs are available for a given stem diameter. Using the output, a family of curves was generated for selected stem diameters relating maximum curvature multiplied by stem radius versus height on the stem at which the maximum curvature occurred (Figure B1).

3. The curves for Figure B1 for a given stem diameter were obtained as follows: For each time increment (Δt), the computer printout provided the curvature for each node point on the stem. The node at which the maximum curvature occurs and the corresponding height of the node provide the data point for that Δt.

4. The model for the stem consists of a right-circular cylinder constrained at the base by a single point, such that the base is free to rotate but not translate (Appendix A). Therefore, as the shock front interacts with the model, the point of maximum curvature must move up the stem. This phenomenon is similar to whiplash. Examination of sequential time increments of the computer printout indicated that the point of maximum curvature did always move up the stem; but because of the complex oscillatory motion of the stem, the value of the maximum curvature did not always increase. Data points that had a lower value of maximum curvature than the previous time step, but a higher node point, were rejected.

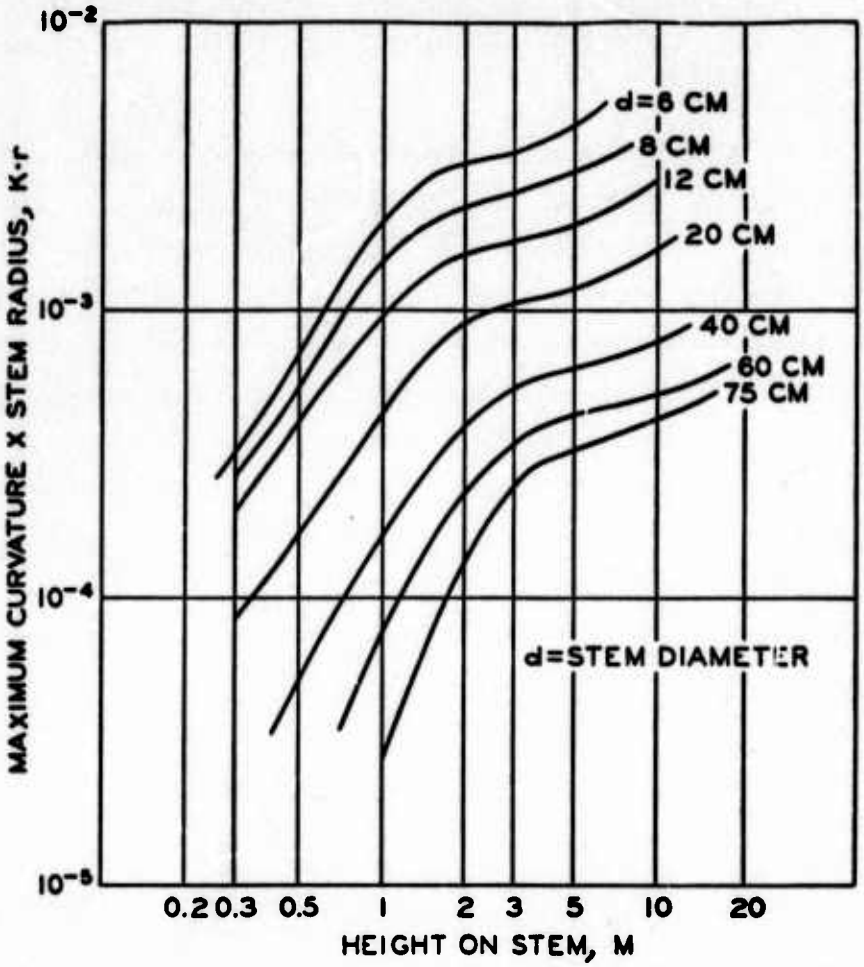

Figure B1. Maximum stem curvature multiplied by stem radius versus height at which maximum curvature occurred

5. The height on the stem at which the maximum curvature occurs and the stem-remnant height are considered to be the same if failure occurs. A remnant height obtained from Figure B1 can be considered to be the remnant height associated with the value of $K_c \times r$ required for failure (Appendix A), because the curves in Figure B1 represent maximum values of curvature on the stem at a given time; therefore, if a calculated value of the critical curvature times the radius is entered on the vertical scale of Figure B1 and has a corresponding value on the horizontal axis, it then follows that this is the remnant height associated with the calculation of $K_c \times r$ because the critical curvature and the maximum curvature are the same. If $K_c \times r$ does not have a

value on the horizontal scale, the stem did not fail and the energy absorbed by the stem from the shock front is dissipated as vibratory motion or structural damage. In view of the above interpretation, the axes of Figure B1 can be relabeled critical curvature times stem radius versus remnant height.

6. The curves generated in Figure B1 by inspection of the printouts for each radius (r) are valid only for the value of Young's modulus (E), total effective pressure impulse (J_T), and stem density (ρ) used in the finite difference solution of the PDE. The solution of the PDE used to produce Figure B1 is termed the reference case solution. Numerical values used in this solution are termed reference case values, i.e., reference case stem radius, reference case Young's modulus, reference case total effective pressure impulse, reference case stem density. The reference case values used in the solution were $r = 6, 8, 12, 20, 40, 60,$ and 75 cm, $E = 1.2 \times 10^{11}$ dynes/cm^2, $J_T = 4.99 \times 10^6$ dyne $\times$ msec/cm^2,* and $\rho = 0.8$ g/cm^3. The curves in Figure B1 are not applicable if a remnant height prediction is desired using values other than those reference case values used in the solution that generated the curves in the figure. In order to make Figure B1 applicable for wide variations in E, J_T, and ρ, two options were available: (a) generate curves for all desired values of E, J_T, and ρ, or (b) derive scale functions such that values of E, J_T, and ρ other than those used in the reference case PDE solution can be used to predict remnant heights using Figure B1. Option (b) is the logical choice.

7. Use of Figure B1 for specific values of E, ρ, and J_T (other than those used in the reference case PDE solution) requires modification of the failure criterion to account for the variations in E, J_T, and ρ. The modified failure criterion is as follows:

$$K_{co} \times r_o = \frac{S\rho J_{To}}{E\rho_o J_B \left[\left(\frac{W}{W_B}\right)^{1/3} C_d + \frac{r}{20}\right]} \qquad \text{(B1)}$$

---

* References in this Appendix are cited at the end of the main text.

where

K_{co} = reference case critical curvature required for stem failure

r_o = reference case stem radius

J_{To} = reference case total effective pressure impulse

ρ_o = reference case stem density

C_d = drag coefficient (0.75 was used in the reference case solution)

The subscript o indicates a parameter used in the reference case solution. The other terms in Equation B1 are:

S = modulus of rupture

E = Young's modulus

ρ = stem density

W = weapon yield

r = stem radius

all of which refer to the specific case solution. The values that refer to the actual stem whose remnant height is required are termed specific case values. Also, J_B = known value of the dynamic pressure impulse at a given distance from GZ for weapon yield W_B. The curves in Figure 8 of Reference 1* were used to compute J_B for the reference case curves in Figure B1. The derivation of Equation B1 is shown in Reference 1, pages 25-34. Also, more information on the reference and specific case solutions can be found in paragraphs 60-80 of Reference 1.

8. The remnant height for a given stem can be obtained by the following procedure:

a. $K_{co} \times r_o$ is computed from Equation B1.

b. The diameter curves in Figure B1 are reference case values and differ from the specific case values by

$$d_o = \frac{d}{\sqrt{\frac{E_o \rho}{E \rho_o}}} \qquad (B2)$$

Therefore, d_o must be calculated for a given d.

---

* References in this appendix are cited at the end of the main text.

c. The remnant height can then be obtained by entering the computed value of $K_{co} \times r_o$ on the vertical axis of Figure B1 and projecting a horizontal line from this point until the proper reference case diameter curve is intersected. A line is then projected parallel to the vertical axis from the intersection to the horizontal axis; the intersection with the horizontal axis is the predicted remnant height.

9. The procedure outlined in paragraph 8 is not conducive to rapid calculation of stem-remnant height if calculational aids are not available, i.e. in a combat situation. Therefore, in an effort to reduce computational difficulties, the entire process was reduced to a nomographic solution (Figure B2), hereafter referred to as the nomograph.

10. Equation B1 can be rewritten as

$$K_{co} \times r_o = \left[\frac{1}{J_B\left(\frac{W}{W_B}\right)^{1/3}}\right]\left(\frac{SJ_{To}\rho}{E\rho_o}\right)\left[\frac{1}{0.75 + \frac{d}{40\left(\frac{W}{W_B}\right)^{1/3}}}\right]$$

The initial procedure is to graphically solve for the term in the second set of brackets. This was accomplished by generating diameter curves for a continuous variation of weapon yields (graph 3 of the nomograph). The resulting numerical scale common to graphs 3 and 4 is the computed numerical value for

$$\left[0.75 + \frac{d}{40\left(\frac{W}{W_B}\right)^{1/3}}\right]$$

for given values of d and W.

11. The next step is to obtain the ratio of $\left(\frac{SJ_{To}\rho}{E\rho_o}\right)$ to $\left[0.75 + \frac{d}{40\left(\frac{W}{W_B}\right)^{1/3}}\right]$ and then divide this value by $J_B\,(W/W_B)^{1/3}$ to obtain $K_{co} \times r_o$. The graphic division process is performed using

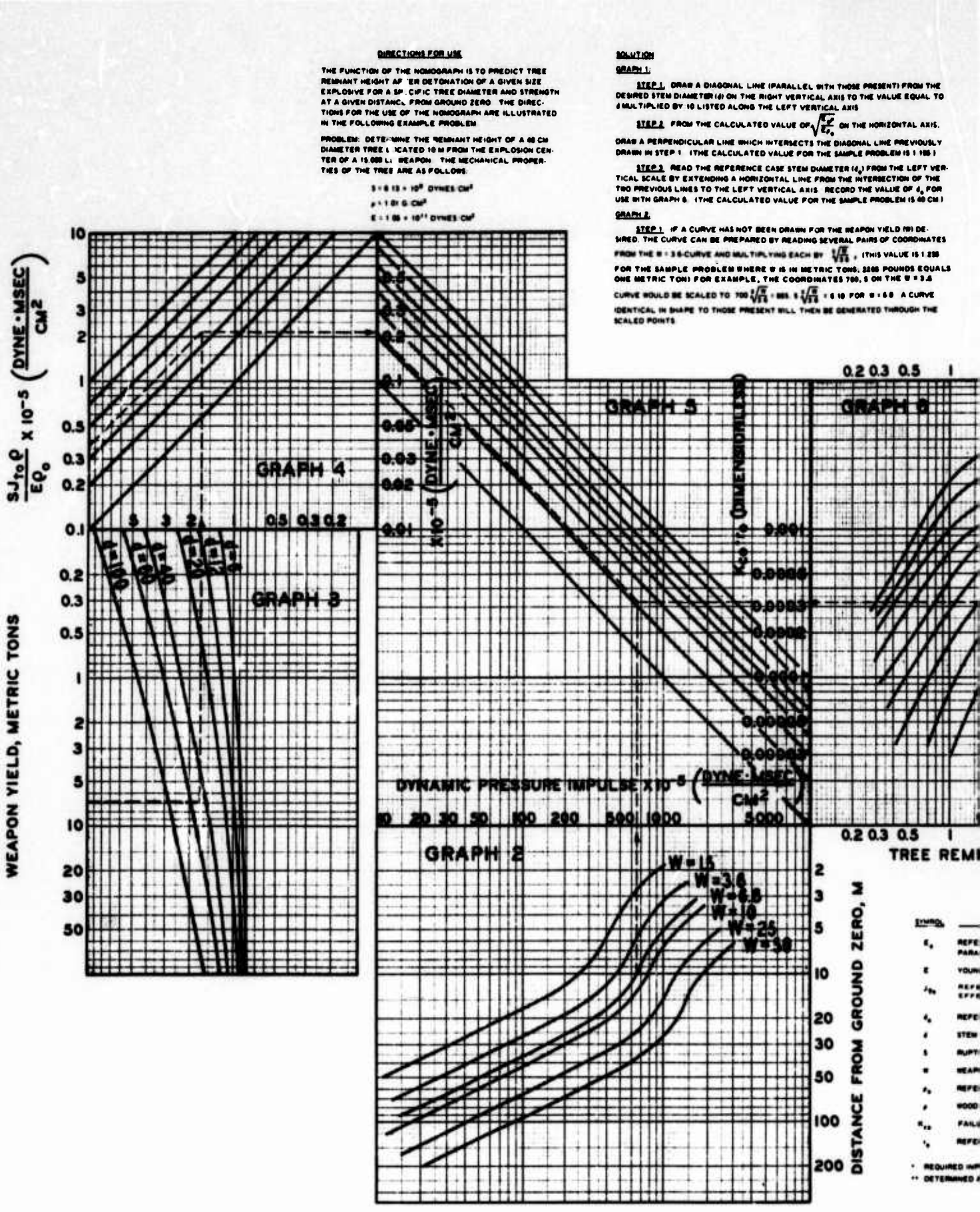

Figure B2. Nomograph to predict tree remnant height afte
specific tree diameter and strength at a

NAL LINE (PARALLEL WITH THOSE PRESENT) FROM THE
ON THE RIGHT VERTICAL AXIS TO THE VALUE EQUAL TO
ALONG THE LEFT VERTICAL AXIS

CULATED VALUE OF $\sqrt{\frac{E\rho}{E_0\rho_0}}$ ON THE HORIZONTAL AXIS.

E WHICH INTERSECTS THE DIAGONAL LINE PREVIOUSLY
CULATED VALUE FOR THE SAMPLE PROBLEM IS 1 198)

FERENCE CASE STEM DIAMETER (d_0) FROM THE LEFT VER-
A HORIZONTAL LINE FROM THE INTERSECTION OF THE
LEFT VERTICAL AXIS RECORD THE VALUE OF d_0 FOR
LCULATED VALUE FOR THE SAMPLE PROBLEM IS 40 CM)

IS NOT BEEN DRAWN FOR THE WEAPON YIELD (W) DE-
REPARED BY READING SEVERAL PAIRS OF COORDINATES
) MULTIPLYING EACH BY $\sqrt[3]{\frac{W}{W_0}}$, (THIS VALUE IS 1 235
M WHERE W IS IN METRIC TONS; 2200 POUNDS EQUALS
AMPLE, THE COORDINATES 700, 5 ON THE W = 3.0
) $700\sqrt[3]{\frac{5}{3.0}} = 865$ & $5\sqrt[3]{\frac{5}{3.0}} = 6.18$ FOR W = 5.0 A CURVE
BE PRESENT WILL THEN BE GENERATED THROUGH THE

STEP 3 AT THE POINT WHERE A HORIZONTAL LINE THROUGH THE DESIRED DISTANCE FROM GROUND ZERO CROSSES THE CURVE FOR THE APPROPRIATE WEAPON YIELD, DRAW A VERTICAL LINE THAT EXTENDS ACROSS THE DIAGONAL LINES ON GRAPH 5 (THIS OPERATION WILL YIELD 650 ON THE HORIZONTAL AXIS OF GRAPH 2 FOR THE SAMPLE PROBLEM)

GRAPH 2:

STEP 1 IF NO CURVE IS PRESENT FOR THE DESIRED STEM DIAMETER (d), AN APPROPRIATE CURVE CAN BE PREPARED BY FINDING HORIZONTAL COORDINATES ASSOCIATED WITH VARIOUS WEAPON YIELDS, (W) AS FOLLOWS:

$$F(d,W) = 0.75 + \frac{d}{40\left(\frac{W}{5.0}\right)^{1/3}}$$

THE NUMERICAL VALUES FOR THE HORIZONTAL AXIS ARE PRESENTED ON THE HORIZONTAL AXIS COMMON TO GRAPHS 3 AND 4. IF ONLY ONE WEAPON YIELD IS BEING UTILIZED THE ENTIRE CURVE NEED NOT BE DRAWN UNLESS IT WILL BE USED LATER (F(d,W) EQUALS 1 72 FOR THE SAMPLE PROBLEM)

STEP 2 AT THE INTERSECTION OF A HORIZONTAL LINE THROUGH THE GIVEN WEAPON YIELD AND CORRECT STEM DIAMETER CURVE, CONSTRUCT A VERTICAL LINE SO THAT IT PASSES THROUGH THE DIAGONAL LINES ON GRAPH 4

GRAPH 4:

STEP 1 CONSTRUCT A DIAGONAL LINE (PARALLEL WITH THOSE PRESENT) FROM THE CALCULATED VALUE OF $\frac{E_0\rho_0 r_0}{E\rho} = 10^{-5}$ ON THE LEFT VERTICAL AXIS (THE CALCULATED VALUE FOR $\frac{E_0\rho_0 r_0}{E\rho} = 10^{-5}$ FOR THE SAMPLE PROBLEM IS 0 384)

STEP 2 FROM THE INTERSECTION OF THE DIAGONAL LINE IN STEP 1 AND THE VERTICAL LINE PROJECTED FROM GRAPH 3, CONSTRUCT A HORIZONTAL LINE WHICH WILL INTERSECT THE RIGHT VERTICAL AXIS OF GRAPH 4 (THIS VALUE IS 0 211 FOR THE SAMPLE PROBLEM)

GRAPH 5:

STEP 1 DRAW A DIAGONAL LINE (PARALLEL WITH THOSE PRESENT) FROM THE INTERSECTION POINT ON THE RIGHT VERTICAL AXIS OF GRAPH 4 TO THE POINT ON THE LEFT VERTICAL AXIS OF GRAPH 6 (WHOSE VALUE IS SMALLER BY A FACTOR OF 10^{-2}).

STEP 2 WHERE THE DIAGONAL LINE IN STEP 1 INTERSECTS THE VERTICAL LINE EXTENDING FROM GRAPH 2, CONSTRUCT A HORIZONTAL LINE THROUGH GRAPH 6 (THE VALUE OF THE VERTICAL AXIS OF GRAPH 6 IS 0.00652 FOR THE SAMPLE PROBLEM)

GRAPH 6:

STEP 1 IF NO CURVE EXISTS ON GRAPH 6 FOR THE STEM DIAMETER (d_0) CALCULATED FROM GRAPH 1, ESTIMATE A FEW POINTS IN THE APPROPRIATE INTERVAL FOR THE DIAMETERS GIVEN AND SKETCH THE APPROXIMATE CURVE THROUGH THOSE POINTS CHOSEN

STEP 2 FROM THE INTERSECTION OF THE K_{10} r_0 VALUE HORIZONTAL LINE EXTENDED FROM GRAPH 5) AND THE REFERENCE CASE STEM DIAMETER CURVE, DRAW A LINE WHICH IS PERPENDICULAR TO THE HORIZONTAL AXIS OF GRAPH 6. THE TREE REMNANT HEIGHT IS THE VALUE ASSOCIATED WITH THE POINT AT WHICH THE PERPENDICULAR LINE CROSSES THE HORIZONTAL AXIS (THE REMNANT HEIGHT IS 1.62 FOR THE SAMPLE PROBLEM)

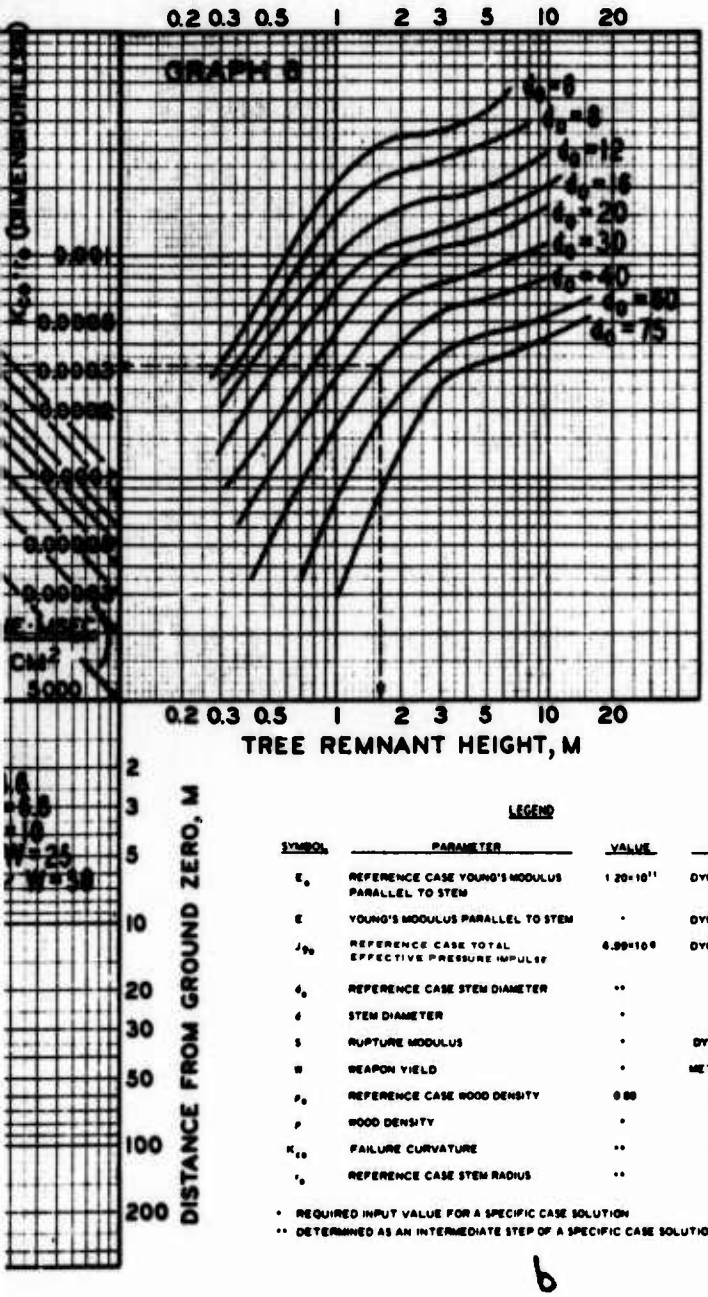

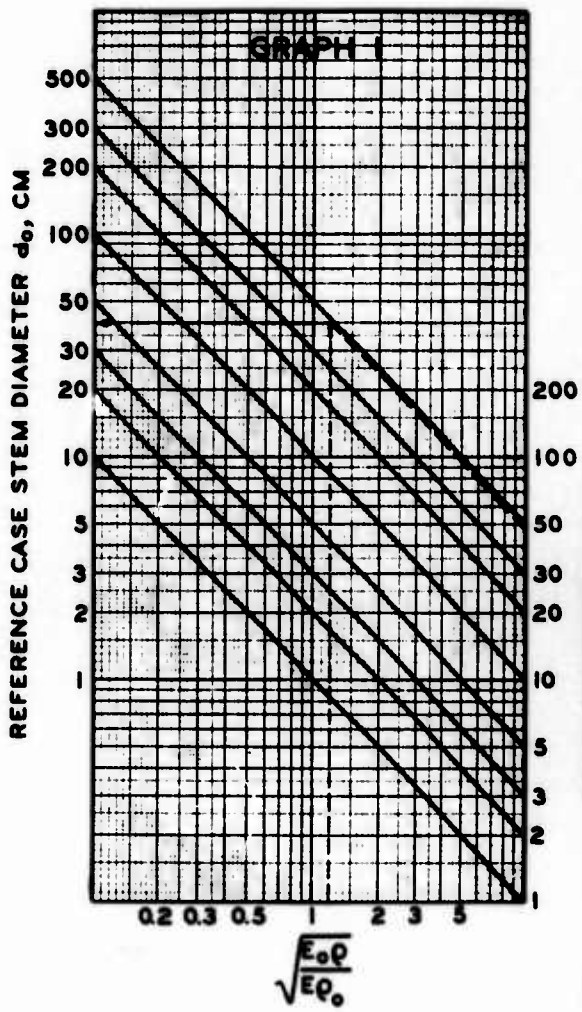

LEGEND

SYMBOL	PARAMETER	VALUE	UNITS
E_0	REFERENCE CASE YOUNG'S MODULUS PARALLEL TO STEM	1.20×10^{11}	DYNES CM^2
E	YOUNG'S MODULUS PARALLEL TO STEM	*	DYNES CM^2
J_{ρ_0}	REFERENCE CASE TOTAL EFFECTIVE PRESSURE IMPULSE	6.99×10^6	DYNE-MSEC CM^2
d_0	REFERENCE CASE STEM DIAMETER	**	CM
d	STEM DIAMETER	*	CM
S	RUPTURE MODULUS	*	DYNES/CM^2
W	WEAPON YIELD	*	METRIC TONS
ρ_0	REFERENCE CASE WOOD DENSITY	0 80	G CM^3
ρ	WOOD DENSITY	*	G CM^3
K_{10}	FAILURE CURVATURE	**	1 CM
r_0	REFERENCE CASE STEM RADIUS	**	CM

* REQUIRED INPUT VALUE FOR A SPECIFIC CASE SOLUTION
** DETERMINED AS AN INTERMEDIATE STEP OF A SPECIFIC CASE SOLUTION

Preceding page blank

B7

b

tree remnant height after explosion of a given size charge for a
meter and strength at a given distance from GZ

logarithmic paper. Figure B3 shows the two possible configurations for graphic division; in both cases A is the numerator and B the denominator. The ratio C is obtained by the following procedure:

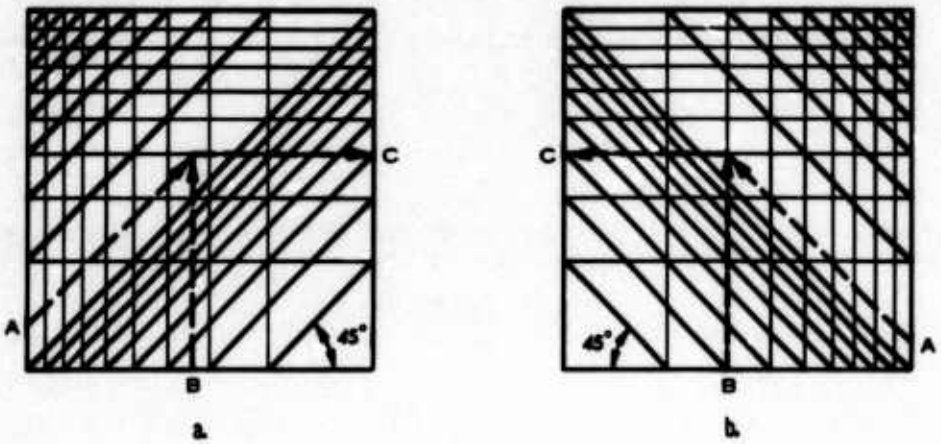

Figure B3. Use of logarithmic paper for graphic division. In both cases, C = A/B and scale A has a numerical value of 10 times scale C

a. A line is projected from the point on the horizontal scale that is the numerical value of the denominator (B). This projected line is perpendicular to the horizontal scale.

b. A line is projected from the point on the vertical scale that represents the numerical value of A (this scale has numerical values of 10 times the other vertical scale). This projected line forms an angle of 45 deg with the horizontal axis.

c. From the intersection of the two projected lines, a line is projected horizontally to the other vertical scale. The numerical value of the ratio A/B is the value on the vertical scale where the projected line crosses the scale.

12. Using the method in Figure B3a, $\left(\frac{SJ_{To}\rho}{E\rho_o}\right)$ is divided by $\left[0.75 + \frac{d}{40\left(\frac{W}{W_B}\right)^{1/3}}\right]$ (graph 4 of the nomograph). The numerical result of the division is represented by the scale common to graphs 4 and 5 on

the nomograph. The value of $\left(\frac{SJ_{To}\rho}{E\rho_o}\right)$ need be calculated only once for each tree species.

13. Using the method in Figure B3b, $\left(\frac{SJ_{To}\rho}{E\rho_o}\right)\left[\frac{1}{0.75 + \frac{d}{40\left(\frac{W}{W_B}\right)^{1/3}}}\right]$ is divided by $J_B\left(\frac{W}{W_B}\right)^{1/3}$ (graph 5 of the nomograph) to obtain $K_{co} \times r_o$. The dynamic pressure impulse, $J_B\left(\frac{W}{W_B}\right)^{1/3}$, is obtained from graph 2 by entering the distance from ground zero (DGZ) on the vertical scale and using the appropriate yield curve. The scale common to graphs 2 and 5 is the numerical value of the dynamic pressure impulse (DPI).

14. Graph 6 is the same as Figure B1 except the vertical scale is now labeled $K_{co}r_o$ and the horizontal scale is labeled tree-remnant height (in metres). Thus the value obtained in graph 5 can be entered into graph 6, provided the proper reference stem diameter is known. The reference diameter is obtained from Equation B2. Graph 1 is a solution of this equation using the method shown in Figure B3b.

15. Additional curves for the graphs shown on the nomograph can be generated as follows:

a. Diagonals for graph 1 can be added for other specific case diameters as required.

b. Curves for yields other than those shown in graph 2 can be generated from any one of the curves shown by using the cube-root scaling law for both the DPI and the DGZ (Reference 6).

c. Curves for graph 3 for diameters other than those shown can be generated by solving $\left[0.75 + \frac{d}{40\left(\frac{W}{W_B}\right)^{1/3}}\right]$ for yields of 0.1 to 100 metric tons (W_B = 3.6 metric tons) for the diameter required.

d. Diagonals for graph 4 can be added for other specific case tree species as required.

e. Diagonals for graph 5 can be added as required for the graphical solution resulting from graphs 3 and 4.

f. Curves for graph 6 can be obtained for stem diameters other than those shown by substituting the required diameter in the finite difference solution for the partial differential equation describing the motion of a stem being acted upon by an incident shock front (Appendix A). The data points for the curve can then be generated from the computer output of the finite difference solution as previously described (paragraph 3).

16. All of the curves can be generated with a minimum of computational difficulty, except those in graph 6. Some interpolation between the diameter lines in graph 6 is acceptable as a last resort, but with an accompanying loss in the credibility in the results.

17. The complexity of the nomograph can be reduced for situations in which the yield or stem diameter is constant or when only one tree species is to be considered. Consider the case of a constant yield. Graph 2 can be eliminated by converting the scale common to graphs 2 and 5 from DPI to DGZ. This can be accomplished by replotting values of DGZ for a given yield curve along the horizontal axis. For constant yield, graph 3 can also be eliminated by converting the scale common to graphs 3 and 4 from $\left[0.75 + \frac{d}{40\left(\frac{W}{W_B}\right)^{1/3}} \right]$ to diameter values. This can be accomplished by replotting the horizontal scale with selected diameter values. Similar schemes can be used for situations in which only one stem diameter or species is of interest.

18. The remnant heights generated from the nomograph should be considered valid data only if:

a. The center of the explosion is well below the bottom of the forest canopy and is less than 5 m above the ground.

b. The overpressure is never negative.

c. The terrain around ground zero is flat.

These constraints are explained in Reference 1. In addition, the nomograph will not predict soil or root failures.

In accordance with ER 70-2-3, paragraph 6c(1)(b), dated 15 February 1973, a facsimile catalog card in Library of Congress format is reproduced below.

Keown, Malcolm Price
Experimental verification of a theoretical loading function describing momentum transfer from an explosion to a tree stem, by Malcolm P. Keown, Jack K. Stoll, and Hansjoerg Nikodem. Vicksburg, U. S. Army Engineer Waterways Experiment Station, 1976.
1 v. (various pagings) illus. 27 cm. (U. S. Waterways Experiment Station. Technical report M-76-2)
Prepared for Office, Chief of Engineers, U. S. Army, Washington, D. C., under Project 4A062112A859, Task 05.
Includes bibliography.

1. Dynamic loads. 2. Explosion effects. 3. Forests. 4. Helicopter landing zones. 5. Momentum transfer. 6. Shock waves. 7. Tree stems. I. Stoll, Jack K., joint author. II. Nikodem, Hansjoerg, joint author. III. U. S. Army. Corps of Engineers. (Series: U. S. Waterways Experiment Station, Vicksburg, Miss. Technical report M-76-2)
TA7.W34 no.M-76-2

B13